

AN INCLUSIVE SEARCH FOR BEYOND THE
STANDARD MODEL LONG-LIVED DECAYS
WITH THE CMS DETECTOR AT THE LARGE
HADRON COLLIDER IN $\sqrt{s} = 13$ TeV DATA

JOSHUA ROBERT HARDENBROOK

A DISSERTATION
PRESENTED TO THE FACULTY
OF PRINCETON UNIVERSITY
IN CANDIDACY FOR THE DEGREE
OF DOCTOR OF PHILOSOPHY

RECOMMENDED FOR ACCEPTANCE
BY THE DEPARTMENT OF
PHYSICS
ADVISER: CHRISTOPHER G. TULLY

© Copyright by Joshua Robert Hardenbrook, 2017.

All rights reserved.

Abstract

A search for long-lived particles decaying to jets is presented, performed on the data collected by CMS at a center-of-mass energy $\sqrt{s} = 13$ TeV in 2015. The data set corresponds to an integrated luminosity of 2.7 fb^{-1} . The analysis exploits a set of trigger algorithms and a customized displaced-jet tagger. The number of tagged displaced-jets is used to characterize a potential signal. The pair production of long-lived particles decaying to two jets or to a b jet and a lepton is excluded for masses lighter than 450–1000 GeV, for lifetimes between 1 mm to 1 m.

Acknowledgements

“People say to me: are you looking for the ultimate laws of physics? No, I’m not. I’m just looking to find out more about the world and if it turns out there is a simple ultimate law that explains everything—so be it. That would be very nice to discover. If it turns out its like an onion with millions of layers and we’re just sick and tired of looking at the layers. Then that’s the way it is. But whatever way it comes out its nature that’s there and she’s going to come out the way she is. Therefore when we go to investigate it, we shouldn’t pre-decide what we want to find out besides to find out more about it. You see – one thing is, I can live with doubt, and uncertainty and not knowing. I think its much more interesting to live not knowing than to have answers that might be wrong. I have approximate answers and possible beliefs, and different degrees of certainty about different things, but I’m not absolutely sure of anything and there are many things I don’t know anything about. But I don’t have to know an answer. I don’t have to. I don’t feel frightened by not knowing things.”

—Richard P. Feynman

This is the dedication all about how my thesis got turned right upside down

Contents

Abstract	iii
Acknowledgements	iv
1 Introduction	1
2 Theory	2
2.1 The Standard Model of Particle Physics	2
2.1.1 Quantum Field Theory	3
2.1.2 Symmetries	8
2.1.3 The Standard Model Lagrangian	15
2.1.4 Electroweak Symmetry Breaking (EWSB)	20
2.1.5 Divergences in the Standard Model	22
2.1.6 Maxwell's Laws	22
2.1.7 Feynman Diagrams	23
2.1.8 Radiative Corrections (Loop Diagrams)	24
2.2 Beyond the Standard Model	25
2.2.1 Open Questions and Incompleteness in the Standard Model .	25
2.2.2 Supersymmetry	25
2.3 Long-lived Signatures	25
2.3.1 Standard Model Particles with Long Lifetimes	25
2.3.2 Split-Susy and Naturalness at the LHC	27

2.3.3	Hidden Valley Models	28
3	Collider Physics and Phenomenology	29
3.1	Introduction	29
3.2	From Matrix Elements to Cross Sections	30
3.3	Luminosity	35
3.4	Parton Model of Hadron Collisions	35
3.5	Kinematic Conventions for Collider Physics	38
3.6	Showering	41
3.7	Hadronization	45
3.8	Hadron Decay	48
3.9	Jet Clustering	48
4	CERN Laboratories	50
4.1	Financial and Organizational Structure	50
4.1.1	Funding Model	50
4.1.2	Organizational Structure	52
4.2	The Large Hadron Collider	52
5	The Compact Muon Solenoid Experiment	55
5.1	Superconducting Solenoid	56
5.2	Electromagnetic Calorimeter (ECAL)	59
5.3	Hadronic Calorimeter (HCAL)	63
5.4	Tracking Layers	66
5.5	Muon Spectrometer	70
5.6	Trigger System	73
5.6.1	Level 1 (L1) Trigger	77
5.6.2	High Level Trigger (HLT)	78
5.6.3	DAQ	80

6 Studies of Displaced Jet Tagging Variables	81
6.1 Introduction	81
6.1.1 Significant differences with respect to b-tagging	82
6.2 Samples	83
6.3 Signal Samples	83
6.4 Individual Variable Studies	86
6.4.1 Impact Parameter Information	86
6.4.2 Calo Jet Information	96
7 Displaced Jet Analysis	99
7.1 Introduction	99
7.2 Datasets	100
7.3 An inclusive displaced-jet tagger	100
7.3.1 Tagging Variable Cut Optimization	105
7.4 Event selection	106
7.5 Datasets and simulated samples	107
7.6 Background prediction	109
7.6.1 Signal Injection Tests	112
7.6.2 Tag Probability Cross Validation	118
7.7 Systematic uncertainties	122
7.7.1 Background systematic uncertainties	122
7.7.2 Signal systematic uncertainties	122
7.8 Results and interpretation	128
Bibliography	142

Chapter 1

Introduction

Chapter 2

Theory

2.1 The Standard Model of Particle Physics

Forward

It is the goal of this section to succinctly (at least in a relative sense) derive the principal aspects of the standard model of particle physics from fundamental principles. The questions to be answered are: how do we build a complex framework consisting of a variety of particles and interactions that experimentally describes the universe (neglecting gravity) with startling accuracy? what are the guiding principles? and despite its success, why is the theory incomplete?

First we will describe the lagrangian formulation of classical mechanics. From here we introduce, classical field theory and the fundamental quantization of quantum mechanics to arrive at quantum field theory (QFT). After a brief discussion of global and local lagrangian symmetries in a QFT, we discuss gauge theories and how local gauge symmetries give rise to the interactions mediating the fundamental forces excluding gravity. Ultimately, we review spontaneous electroweak symmetry breaking as the source of the gauge boson masses and the higgs field.

- Energy and The Principle of Minimal Action: Here we will build up the concept

- Symmetry and Local Gauge Symmetry: What symmetries do we enforce upon the form of our theory and what are the consequences.
- Theory Renormalizability: What limits the type of terms we can include in our lagrangian as to preserve the ability to calculate the outcomes of scattering processes.

2.1.1 Quantum Field Theory

Lagrangian Mechanics

In lagrangian mechanics, the time evolution of some generalized coordinate q can be determined via the principle of minimal action $\delta S = 0$.

$$S[q(t)] = \int_{t_1}^{t_2} L\left(q, \frac{dq}{dt}, t\right) dt$$

where S is a functional of the time dependent generalized coordinate $q(t)$. Let $\dot{q} = \frac{dq}{dt}$
The equations of motion are derived by varying S

$$\delta S = \int_{t_0}^{t_1} \left[\frac{\partial L}{\partial \dot{q}} \delta \dot{q} + \frac{\partial L}{\partial q} \delta q \right] dt$$

Note that $\delta \dot{q} = \delta \frac{dq}{dt} = \frac{d(\delta q)}{dt}$. Integrate the first term by parts, and require that δq vanish at the boundaries:

$$\int_{t_0}^{t_1} \left[-\frac{d}{dt} \left(\frac{\partial L}{\partial \dot{q}} \right) \delta q + \frac{\partial L}{\partial q} \delta q \right] dt = \delta S = 0$$

by the principle of minimal action we have arrived at the euler equations of motion:

$$\frac{d}{dt} \left(\frac{\partial L}{\partial \dot{q}} \right) = \frac{\partial L}{\partial q}$$

For a generic lagrangian with potential energy term $V(q)$, $L = \frac{1}{2}m_q\dot{q}^2 - V(q)$ we obtain the equation of motion (or force law) $F = m\ddot{q} = -\frac{dV}{dq}$

Classical Field Theory

In comparison with classical mechanics, which deals with finitely many [cite:tong] general coordinates q_i , classical field theory deals with an infinite number of degrees of freedom $\phi_i(\vec{x}, t)$ [cite:tong] with a degree of freedom for each spatial coordinate \vec{x}, t and index i . For simplicity we use a single index μ for the four spacetime dimensions and utilize the einstein summation convention where repeated indicies are summed over. The corresponding action can be written in terms of a lagrangian density $\mathcal{L}(\phi, \partial_\mu\phi)$

$$S = \int dt L = \int d^3x \int dt \mathcal{L}(\phi, \partial_\mu\phi) = \int dx^4 \mathcal{L}(\phi, \partial_\mu\phi)$$

Similarly, we arrive at classical Euler-Lagrange Equations of motion:

$$\partial_\mu \left(\frac{\partial \mathcal{L}}{\partial(\partial_\mu\phi)} \right) = \frac{\partial \mathcal{L}}{\partial\phi}$$

We now consider the simple free lagrangian density for a real scalar field ϕ :

$$\mathcal{L} = \frac{1}{2}\partial_\mu\phi\partial^\mu\phi - \frac{1}{2}m\phi^2$$

we have achieved a relativistically invariance for free as all indicies are contracted. To see this, consider a lorentz transformation Λ on the kinetic term. The transformation induces $\phi(x) \rightarrow \phi'(x) = \phi(\Lambda^{-1}x) = \phi(y)$. The transformation is Λ as we actively rotate the coordinate system rather than rotating the field.

$$\partial_\mu\phi\partial^\mu\phi \rightarrow ((\Lambda^{-1})_\rho^\mu\partial^\rho\phi)((\Lambda^{-1})_\nu^\mu\partial_\nu\phi) = \eta^{\rho\nu}\partial_\rho\phi\partial_\nu\phi = \partial^\nu\phi\partial_\nu\phi$$

where we have used the fact that the spacetime metric is invariant under lorentz transformations.

$$\Lambda_\rho^\mu \eta^{\rho\lambda} \Lambda_\lambda^\nu = \eta^{\mu\nu}$$

As the action integrates over all space time, the change of variable from $x \rightarrow y$ is inconsequential and yield the same equations of motion. Applying the euler lagrange equation we arrive at the classical relativistically invariant klein gordon equation:

$$(\partial^2 - m^2)\phi = 0$$

taking the fourier transform of state ϕ :

$$\phi(\vec{x}, t) = \int \frac{d^3 p}{(2\pi)^3} e^{-i\vec{p}\cdot\vec{x}} \phi(\vec{p}, t)$$

Note that the $(2\pi)^3$ is a normalization convention on the field. We see that the solution satsfies:

$$\left(\frac{\partial^2}{\partial t^2} + (p^2 + m^2) \right) \phi(\vec{p}, t) = 0$$

From this we recognize that this is just the equation of motion for a harmonic oscillator with energy $\omega^2 = p^2 + m^2$

The Canonical Quantization

Quantum mechanics consists of 4 fundamental postulates. Here we enumerate their classical counter parts [cite.schrednicki]

1. **Particle State:** In classical mechanics a the state of a particle is determined by two variables $x(t)$ and $p(t)$. In quantum mechanics, the state is a vector $|\psi\rangle$ in a hilbert space \mathcal{H}
2. **Dynamic Variables :** Clasically, all dynamical variables are a function only $x(t)$ and $p(t)$. In quantum mechanics, classical variables represented as a function of x and p are instead represented by hermitian operators X and P that statisfy the commutation relation $[X, P] = \frac{i}{\hbar}$.
3. **Measurement:** Clasically, the particle state is unaffected by measurement and strictly deterministic based on the values of x and p . Quantum mechanically, a particle in a state $|\psi\rangle$ when measured will yield and eigenvalue ω of the operator Ω with probability $|\langle\omega|\psi\rangle|^2$. After measurement the particle state is the corresponding eigenvector $|\omega\rangle$
4. **Time Evolution:** Classically, p and x change with time according to hamiltons (or lagrangian) equations of motion. Quantum mechanics asserts the state vector evolves with time according to the Schrodinger equation: $i\hbar\frac{d}{dt}|\psi(t)\rangle = H|\psi(t)\rangle$. Where H is the hamiltonian with classical p and q replaced by the corresponding quantum mechanical operators

The canonical quantization consists of the second postulate that that measurement of position and momentum do not commute (postulate 2). This is the source of the famous heisenburg uncertainty principle that there are no simultaneously measurable states of p and q .

If we consider the quantum harmonic oscillator with hamiltonian:

$$H = \frac{p^2}{2} + \frac{1}{2}\omega^2 q^2$$

and define the creation (a^\dagger) and annihilation (a) operators:

$$a = \sqrt{\frac{\omega}{2}}q + \frac{1}{\sqrt{2\omega}}p \quad a^\dagger = \sqrt{\frac{\omega}{2}}q - \frac{1}{\sqrt{2\omega}}p$$

which yields the position and momentum operators in terms of the newly defined operators.

$$q = \frac{1}{\sqrt{2\omega}}(a + a^\dagger) \text{ and } p = -i\frac{\omega}{2}(a - a^\dagger)$$

substituting into the hamiltonian we find a simple solution after applying the commutation relation $[p, q] = -i$ (where we have set $\hbar = 1$):

$$H = \omega(a^\dagger a + \frac{1}{2})$$

Importantly we see via the relation $[H, a]|E\rangle = (E - \omega)a|E\rangle$ and $[H, a^\dagger]|E\rangle = (E + \omega)a^\dagger|E\rangle$ that the operators raise and lower the harmonic oscillator in multiples of ω . The energy levels are quantized in units of ω . Also called ladder operators, a and a^\dagger , raise and lower the energy state by 1 unit of ω with a ground state energy $\frac{\omega}{2}$.

If we now consider knowledge of classical field theory we can build a quantum field by promoting the coordinate q to a field ϕ . We now write the solution to the Klein-Gordon equation as an infinite sum of creation and annihilation operators that create or destroy a particle with energy $\omega_p^2 = p^2 + m^2$ designated by its four-momentum p . Taking the solution to fourier space:

$$\phi = \int d^4x \frac{1}{\sqrt{2\omega_p}} [a_p e^{ipx} + a_p^\dagger e^{-ipx}]$$

Although result only applies for a real scalar field (spin 0), the corresponding fermionic field (spin 1/2) field can be found similarly starting from the dirac equation.

2.1.2 Symmetries

Noether's Theorem

It cannot be understated the importance and the consequences of symmetries in the standard model. The invariance of the action (equivalently the equations of motion) under linear translations of the coordinates gives rise to conservation of momentum. Simillarly, rotations of the coordinate space yields the conservation of angular momentum. This is a consequence of noether's theorem, that every continuous symmetry of the action has a corresponding conservation law.

To be concrete, let us consider an action that is invariant under some field transformation $\phi \rightarrow \phi + \delta\phi$. If we consider a gauge transformation $\phi \rightarrow e^{i\beta}\phi$ then the infinitesimal transformation is $\delta\phi = i\beta\phi$. Where we are taking for granted that $\delta S = 0$ under this variation, or effectively $\delta\mathcal{L}$ up to surface terms in the action integral. More on this later.

$$\delta\mathcal{L} = \left[\frac{\partial\mathcal{L}}{\partial\phi} \delta\phi + \frac{\delta\mathcal{L}}{\partial_\mu(\partial_\mu\phi)} \delta(\partial_\mu\phi) \right] = i\beta \left[\frac{\partial\mathcal{L}}{\partial\phi} \phi + \frac{\partial\mathcal{L}}{\partial(\partial_\mu\phi)} (\partial_\mu\phi) \right]$$

We futher require that the solution satisfying the euler-lagrange equations, and exchange the first term:

$$= i\beta \left[\partial_\mu \left[\frac{\partial\mathcal{L}}{\partial(\partial_\mu\phi)} \right] \phi + \frac{\partial\mathcal{L}}{\partial_\mu\phi} (\partial_\mu\phi) \right] = i\beta \left[\partial_\mu \left[\frac{\partial\mathcal{L}}{\partial(\partial_\mu\phi)} \phi \right] \right] = \partial_\mu \left[\frac{\partial\mathcal{L}}{\partial(\partial_\mu\phi)} \right]$$

$$\partial_\mu j^\mu = 0$$

Where j^μ is the conserved current corresponding to the continuous symmetry. Now consider the consequences for fermionic lagrangian:

$$\mathcal{L} = \bar{\psi}(i\gamma^\mu \partial_\mu - m)\psi$$

the corresponding current is $j^\mu = i\bar{\psi}\gamma^\mu\psi = (\rho, \vec{j})$ where ρ is charge density and \vec{j} is electric current. We expand the index and $\partial_\mu = (\frac{d}{dt}, \vec{\nabla})$ we obtain the continuity equation:

$$\frac{d\rho}{dt} + \nabla \cdot \vec{j} = 0$$

Symmetry Groups and Algebras

cite.groups.resp.and.physics.HF.jones

To describe symmetry mathematically we need to discuss groups. A group is an algebraic structure (the field of math is known as abstract algebra and more specifically group theory) that consists of a set G (ex. Integers) and a pairwise operation (ex. multiplication) $a \cdot b = c$ where $a, b, c \in G$. The group must also contain an identity $i \in G$ (ex. 1) such that $i \cdot g = g$ for all $g \in G$. All elements $g \in G$ must have an inverse $g^{-1} \in G$ such that $g \cdot g^{-1} = g^{-1}g = i$. The operation must additionally satisfy associativity $(a \cdot b) \cdot c = a \cdot (b \cdot c)$. Importantly, the group does not necessarily need to be abelian $a \cdot b = b \cdot a$, a common example in physics is matrix in general multiplication (multiples of the identity matrix are abelian).

For example, we can consider the group of rotations $SO(3)$ (read special orthogonal group of dimension 3) about the origin in euclidian \mathbb{R}^3 under composition. Clearly the composition of two rotations is another rotation, the inverse rotation is just rotating back, and the identity is performing no rotation at all. The rotations can be represented by real 3 by 3 matrices, determinant ± 1 , where element inverses are their transpose $g^{-1} = g^T$. Interestingly, the group $SU(2) \cong SO(3)/\mathbb{Z}_2$, that is, $SU(2)$ is a double covering of $SO(3)$.

Sepcifically, a lie group is a continuous group with a multlicative law that is a differentiable function of the parameters. linear combinations of generator elements:

$$e^{-i\vec{\beta} \cdot \vec{T}} = e^{-i\beta^i T^i} = U_G(\vec{\beta})$$

where the T^i are the generator elements. For instance, we can build rotations in 3 dimensional space using the dimension 2 representation by exponentiating the pauli spin matrices $\vec{\sigma} = (\sigma_1, \sigma_2, \sigma_3)$ (note the conventional normalization) :

$$L_1 = \frac{\sigma_1}{2} = \frac{1}{2} \begin{pmatrix} 0 & 1 \\ 1 & 0 \end{pmatrix} \quad L_2 = \frac{\sigma_2}{2} = \frac{1}{2} \begin{pmatrix} 0 & -i \\ i & 0 \end{pmatrix} \quad L_3 = \frac{\sigma_3}{2} = \frac{1}{2} \begin{pmatrix} 1 & 0 \\ 0 & -1 \end{pmatrix}$$

In fact, generically the lie algrebra of a group G is defined by the commutation relations of its generators T^i , specifically:]

$$[T^i, T^j] = T^i T^j - T^j T^i = i c_{ijk} T^k$$

where c_{ijk} are known as the structure constants of the algebra. The algebra is abelian if and only if all $c_{ijk} = 0$. Otherwise, the c_{ijk} must be anti-symmetric in any of the two indicies.

In particular to quantum field theory, the Poincare symmetry group plays an important role in the source of the most fundamental conservation laws and the statistics of the quantum fields. The poincare Symmetry group consists of transformations of the form:

$$x'_\mu = \lambda_\mu^\nu x_\nu + a_\mu$$

where Λ_μ^ν is a lorrentz transformation from the lorrentz group $SO(3, 1)$ (boosts and rotations) and a_μ is a translation consisting of 4 single 4-vector $\mathbb{R}^{3,1}$.

The generators of the Poincare group can be enumerated as generalized angular momentum operators: $L_{\mu\nu} = i(x_\mu \partial_\nu - x_\nu \partial_\mu)$ with the commutation relations:

$$[L_{\mu\nu}, L_{\rho\sigma}] = -i(\eta_{\mu\rho}L_{\nu\sigma} - \eta_{\nu\sigma}L_{\mu\rho} + \eta_{\nu\sigma}L_{\mu\rho} - \eta_{\mu\rho}L_{\nu\sigma})$$

However, by decomposing the operators into rotations and boosts these relations become much simpler. Define:

$$J_i = \frac{1}{2}\epsilon_{ijk}L_{jk} \quad P_i = i\partial_i \quad K_i = L_{0i}$$

Where J and P are the familiar angular and linear momentum operators. We obtain more familiar commutation relations:

$$\begin{aligned} [J_i, J_j] &= i\epsilon_{ijk}J_k & [P_0, J_j] &= 0 \\ [P_i, J_j] &= i\epsilon_{ijk}P_k & [P_0, K_i] &= iP_i \\ [P_i, K_j] &= iP_0\delta_{ij} \end{aligned}$$

For a given lie algebra, the dimension of the representation of the group is physically related to the quadratic casimir. For a given concrete representation L_n for a n dimensional representation, the quadratic casimir C_2 can be written as:

$$L_n^2 = C_2(L_n)I$$

where I is the identity. For example, for the group algebra for rotations $SU(2)$ we define j as $n = 2j + 1$ and consider the $j = 0, 1/2$, and 1 representations. For $j = 0$ we have $n = 1$ in which case, the rotation is always trivial to the state. For $j = 1/2$

we have $n = 2$ with the traceless generators:

$$L_1 = \begin{pmatrix} 0 & 0 & 0 \\ 0 & 0 & -i \\ 0 & i & 0 \end{pmatrix} \quad L_2 = \begin{pmatrix} 0 & 0 & i \\ 0 & 0 & 0 \\ -i & 0 & 0 \end{pmatrix} \quad L_3 = \begin{pmatrix} 0 & -i & 0 \\ i & 0 & 0 \\ 0 & 0 & 0 \end{pmatrix}$$

The lorentz group can further be decomposed into $SO(3,1) \cong SU(2) \times SU(2)$ where $SU(2)$ is the group of matrices with determinant ± 1 where the inverses are the conjugate transpose: $g^{-1} = (g^T)^*$. The fundamental fields in the SM lagrangian are characterized by the four corresponding combinations of $SU(2)$ representations. The $(0,0)$ representation of $SU(2) \times SU(2)$ corresponds to scalar spin 0 fields ϕ . The two chiral representations $(1/2,0)$ and $(0,1/2)$ correspond to fermionic matter fields ψ . The $(1/2,1/2)$ representation corresponds to the fundamental vector boson fields W_μ, B_μ, G_μ and the fields after electroweak symmetry breaking. W^\pm, Z^0, A_μ .

Let us now consider a field transformation $\phi_a \rightarrow \phi'_a$ under some lie algebra with generators L_i such that the transformation is $U_g(\beta)$. Consider the heisenburg picture of quantum mechanics where operators evolve but the states remain fixed.

$$\langle O' \rangle = \langle \psi | U_g^{-1}(\beta) O U_g(\beta) | \psi \rangle$$

$$O' = U_g^{-1}(\beta) O U_g(\beta)$$

we obtain a transformed quantum field:

$$\phi'_a = e^{-i\vec{\beta} \cdot \vec{T}} \phi_a e^{-i\vec{\beta} \cdot \vec{T}}$$

expanding the exponentials we see that:

$$\phi'_a = \phi_a - i[\vec{\beta} \cdot \vec{T}, \phi_a] + \frac{(-i)^2}{2} [\vec{\beta} \cdot \vec{\tau}, [\vec{\beta} \cdot \vec{T}, \phi_a]] + O(\beta^2)$$

Where L^i is the concrete representation of T^i . applying $[T^i, \phi_a] = -L_{ab}^i \phi_b$ gives the field transformation law:

$$\phi'_a = \left(e^{i\vec{\beta} \cdot \vec{L}} \right)_{ab} \phi_b$$

and similarly the conjugate field ϕ_a^\dagger transforms in the adjoint representation:

$$\phi_a^\dagger = \left(e^{-i\vec{\beta} \cdot \vec{L}} \right)_{ab} \phi_b^\dagger$$

Local Gauge Invariance and the Covariant Derivative

cite-peskin-pg482 Lets consider what happens when we promote the lagrangian symmetry of fields under the Standard Model gauge symmetries to a local symmetry. Local in the sense that a space dependent transformation for example, the $U(1)$ gauge symmetry transforms the field ψ as:

$$\psi(x) \rightarrow e^{-\alpha(x)} \psi(x)$$

If we then consider a direction derivative in the direction n^μ as defined:

$$n^\mu \partial_\mu \psi(x) = \lim_{\epsilon \rightarrow 0} \frac{\psi(x + \epsilon n) - \psi(x)}{\epsilon}$$

This is not going to have a simple transformation law, since the two states are not at the same point in sample time. We need a connection such that we have a simple transformation law. Consider:

$$n^\mu \partial_\mu \psi(x) = \lim_{\epsilon \rightarrow 0} \frac{1}{\epsilon} (\psi(x + \epsilon n) - U(x + \epsilon n, x) \psi(x))$$

where $U(x, y)$ is our connection and transforms as:

$$U(x, y) \rightarrow e^{i\alpha(x)} U(x, y) e^{-i\alpha(y)}$$

such that when we apply the transformation to the directional derivative we obtain:

$$n^\mu \partial_\mu \psi(x) = \lim_{\epsilon \rightarrow 0} \frac{1}{\epsilon} e^{i\alpha(x+n\epsilon)} (\psi(x + \epsilon n) - U(x + \epsilon n, x) \psi(x))$$

Now lets expand the transformation for an infinitesimal ϵ :

$$\begin{aligned} U(x + \epsilon n, x) &\approx U(x, x) + c\epsilon n^\mu A_\mu(x) + O(\epsilon^2) \\ &= 1 + c\epsilon n^\mu A_\mu(x) + O(\epsilon^2) \end{aligned}$$

Where we have used the fact that the connection between x and itself is trivial and specified some arbitrary (but very suggestive of our final answer) constant $c = ie$. If we would then like to see how this field A_μ transforms we need to check the $U(x, y)$ transformation:

$$\begin{aligned} e^{i\alpha(x)} U(x + \epsilon n, x) e^{-i\alpha(y)} &= (1 + i\alpha(x + n\epsilon))(1 - ie\epsilon n^\mu A_\mu)(1 - i\alpha(x)) \\ &= 1 + i\alpha(x + n\epsilon) - ie\epsilon n^\mu A_\mu - i\alpha(x) \end{aligned}$$

comparing this to the expansion of $U(x + \epsilon n, x)$ we see:

$$\begin{aligned} 1 + ie\epsilon n^\mu A_\mu(x) &= 1 + i\alpha(x + n^\mu \epsilon) - ie\epsilon n^\mu A_\mu(x) - i\alpha(x) \\ A_\mu(x) &= \left[\frac{\alpha(x + n^\mu \epsilon) + \alpha(x)}{en^\mu \epsilon} + A_\mu(x) \right] \\ A_\mu(x) &= \left[-\frac{1}{n^\mu} \frac{1}{e} \partial_\mu \alpha(x) + A_\mu(x) \right] \end{aligned}$$

If we pick the axes such that $n^\mu = 1$ then we have the transformation law for the gauge field: $A_\mu(x) \rightarrow A_\mu(x) - \frac{1}{e}\partial_\mu\alpha(x)$.

2.1.3 The Standard Model Lagrangian

The Standard Model of particle physics is a quantum field theory of 3+1 dimensional spacetime governed by a lagrangian with four sectors and three local gauge symmetries developed to describe the physics of fundamental particles in the physical, observable universe.

The SM lagrangian has 3 types of fundamental fields spin-0 (scalar), spin-1/2 (dirac). and spin 1 (vector). The field content of the theory is listed in Table 2.2 with the associated mass dimensions. Dimensional analysis tells us the mass dimension of the lagrangian is 4 as dictated by the action being unitless. Requiring dimension 4 of each individual term and requiring that all indices are contracted (lorentz invariance) is highly constraining to the types of terms within the lagrangian. The types of interactions (after electroweak symmetry breaking) are listed in Table 2.3.

It is important to understand the principal components of the theory, so we can separate the aspects which are emergent from the underlying assumptions and those which are put in by hand. Here we list

- **Relativistic Theory:** The Lagrangian must be invariant under lorentz transformations as well as rotations and translations in 3+1 dimensional spacetime.
- **Matter:** There are three families of fermionic particles each consisting of an up-type quark, down-type quark, a lepton, and associated neutrino.
- **Fundamental Charges:** Each particle transforms as a multiplet of the gauge symmetries as dictated in ???. This sets which forces interact with which particles.

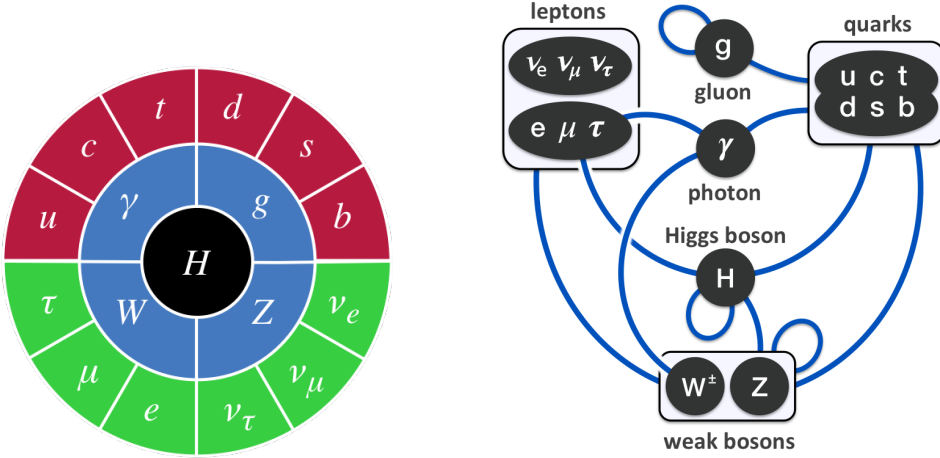


Figure 2.1: The

- **Gauge Interactions:** The fundamental action must be invariant under local gauge transformations.
- **Free Parameters:** The Lagrangian includes 19 free parameters which set the experimentally observed fermion masses, interaction strengths, mass-flavor mixing, the vacuum potential and the possible cp violating terms (Table ??).

The simplicity of the governing assumptions and naturalness of free parameters are certainly an ambition of any theory of fundamental particle physics, but a more aesthetically pleasing theory is not necessarily the ultimate goal. The Standard Model, is a tool towards finding a more complete theory. The theory admits its incompleteness in its formulation (ex. the exclusion of gravity), but achieves incredible theoretical predictions as accurate as 1 part in 10^{11} (cite-find-g-2-result).

$$\begin{aligned}\mathcal{L}_{SM} &= \mathcal{L}_{Gauge} + \mathcal{L}_{Fermion} + \mathcal{L}_{Higgs} + \mathcal{L}_{Yukawa} \\ &= \left(-\frac{1}{4} F_{\mu\nu} F^{\mu\nu} \right) + (\bar{\psi} i \gamma^\mu \partial_\mu \psi) + \left(\frac{1}{2} (\partial_\mu \phi)^2 + V(\phi) \right) + (\bar{\psi}_i y_{ij} \psi_j \phi)\end{aligned}$$

Table 2.1: Standard Model particle representations under the symmetry groups $SU(2)$ and $SU(3)$ respectively n_2 and n_3 . Also listed is associated electroweak hypercharge Y as well as the electric charge Q

	q_L	l_L	u_R	d_R	e_R	ν_R	ϕ
n_3	3	1	3	3	1	1	1
n_2	2	2	1	1	1	1	2
$Y_{U(1)}$	1/6	-1/2	2/3	-1/3	-1	0	1/2
$Q = Y + T_L^3$	2/3	-1/3	2/3	-1/3	-1	0	0

Table 2.2: cite-tully-particle: The fundamental fields types contained in the SM Lagrangian

Field	Lagrangian Term	Field Dim. [Mass]
Scalar Field	$(1/2)(\partial_\mu\phi)(\partial^\mu\phi)$	$[\phi] = M^2$
Dirac Field	$\bar{\psi}M\psi$	$[\psi] = M^{3/2}$
Field Stress Tensor	$-(1/4)F_{\mu\nu}F^{\mu\nu}$	$[F_{\mu\nu}] = M^2$
Vector Field	$F_{\mu\nu} = \partial_\mu A_\nu - \partial_\nu A_\mu$	$[A_\mu] = M$

Gauge Sector

The gauge sector consists of the field stress energy tensor of the 3 corresponding types of gauge bosons: G^i (gluons of the color force), W^i (W's of the weak force) and B (of the weak hypercharge). Here the index i enumerates their multiplicity. There are 8 gluons, 3 W's and a single B. Ultimately, we will arrive have 8 gluons, W^\pm and the photon A^μ because the $SU(2) \times U(1)$ symmetry is spontaneously broken and the

Table 2.3: cite-tully-particle: The types of terms included in the Standard Model Lagrangian

Coupling Type	Lagrangian Term	Coupling Dim [Mass]
Gauge Coupling	$g\psi\gamma_\mu\psi A^\mu$	$[g] = 1$
Triple Gauge Coupling	$A_\mu A^\mu \partial_\nu A^\nu$	$[g] = 1$
Quartic Gauge Coupling	$g^2(A_\mu A^\nu)^2$	$[g] = 1$
Yukawa Coupling	$g\psi\psi\phi$	$[g] = 1$
Scalar Coupling w/ Gauge Bosons	$\tilde{g}A_\mu A^\mu \phi$	$[\tilde{g}] = M$
	$gA_\mu(\partial^\mu\phi)\phi$	$[g] = 1$
Scalar self-couplings	$\tilde{g}\phi^3$	$[\tilde{g}] = M$
	$g\phi^4$	$[g] = 1$

Table 2.4: The 19 free parameters of the Standard Model with values as dictated by experimental observation

Category	Name	Parameter	Remarks
Lepton Masses	Electron, Tau, and Mu	m_e, m_μ, m_τ	$m_l = (\lambda_l \nu)/2$
Fermion Masses	Up, Charm, Top Down, Strange, Bottom	m_u, m_c, m_t m_d, m_s, m_b	
CKM Matrix	Mass-Flavor Mixing Angles CP Violating Phase	$\theta_{12}, \theta_{23}, \theta_{13}$ δ	
Higgs Parameters	Vacuum Expectation Value Higgs Mass	ν m_h	$\nu = \mu/\sqrt{\lambda}$ $m_h^2 = -2\mu^2$
Force Strength	Gauge Couplings	g, g', g_s	$\alpha, \alpha_w, \alpha_s$
CP Violating Terms	Vaccum QCD Angle	θ_{QCD}	unobserved

scalar ϕ takes on a new vaccum state. More on this later.

$$\mathcal{L}_{Gauge} = -\frac{1}{4}F_{\mu\nu}^i F^{\mu\nu i} = -\frac{1}{4}G_{\mu\nu}^i G^{\mu\nu i} - \frac{1}{4}W_{\mu\nu}^i W^{\mu\nu i} - \frac{1}{4}B_{\mu\nu} B^{\mu\nu} \quad (2.1)$$

where the double scripts correspond to the commutation relations for the gauge group algebra.

$$X_{\mu\nu}^i = [D_\mu X_\nu, D_\nu X_\mu] = \partial_\mu X_\nu^i - \partial_\nu X_\mu^i - g f_{ijk} X_\mu^j X_\nu^k \quad (2.2)$$

where g is the coupling constant, the D_μ terms correspond to the covariant derivative and the f_{ijk} are the corresponding structure constants for the non-abelian groups that arise from the non commuting generators of the algebra. In full, the field stress tensor terms are:

$$G_{\mu\nu}^i = \partial_\mu G_\nu^i - \partial_\nu G_\mu^i - g_s f_{ijk} G_\mu^j G_\nu^k$$

$$W_{\mu\nu}^i = \partial_\mu W_\nu^i - \partial_\nu W_\mu^i - g \epsilon_{ijk} W_\mu^j W_\nu^k$$

$$B_{\mu\nu} = \partial_\mu B_\nu - \partial_\nu B_\mu$$

Yukawa Sector

The fermion sector consists of the kinetic energy terms for each quark (up and down types) and leptons (lepton, neutrinos) in the standard model. The left handed quarks transform as an $SU(2)$ doublet:

$$q_{mL\alpha}^0 = \begin{pmatrix} u_{m\alpha}^0 \\ d_{m\alpha}^0 \end{pmatrix}_L \quad \text{and} \quad l_{mL} = \begin{pmatrix} \nu_m^0 \\ e_m^{-,0} \end{pmatrix}_L \quad (2.3)$$

where the subscript m denotes the family (1st, 2nd and 3rd generation) and α denotes the color charge (red, green, and blue). As the $SU(2)_L$ symmetry only acts on the left handed fermions we further separate the fermion sector into left and right components:

$$\begin{aligned} \mathcal{L}_{fermion,L} &= \bar{q}_{mL}^0 i\gamma^\mu D_\mu q_{mL}^0 + \bar{l}_{mL}^0 i\gamma^\mu D_\mu l_{mL}^0 \\ \mathcal{L}_{fermion,R} &= \bar{u}_{mR}^0 i\gamma^\mu D_\mu u_{mR}^0 + \bar{d}_{mR}^0 i\gamma^\mu D_\mu d_{mR}^0 + \bar{e}_{mR}^0 i\gamma^\mu D_\mu e_{mR}^0 + \bar{\nu}_{mR}^0 i\gamma^\mu D_\mu \nu_{mR}^0 \end{aligned}$$

The yukawa sector uniquely contains a large number of the free parameters in the standard model (13 of 19). The individual masses of each fermion and lepton are generated by the y_{ij} terms which are set to agree with experimental values (9 free parameters). This sector also implicitly includes parameters characterizing the mis-match mixing between the quark flavor and mass eigenstates which occur after electroweak symmetry breaking (4 parameters). The mixing is characterized by the 3x3 unitary Cabibbo-Kobayashi-Maskawa (CKM) matrix V^{CKM} . The convention is chosen that flavor states u^I for up type quarks are aligned with the mass states u and the down type quarks are rotated through the transformation $d_i^I = V_{ij}^{CKM} d_j$. From the unitarity condition, the matrix can be parameterized in 4 parameters: three mixing angles $\theta_{12}, \theta_{23}, \theta_{13}$ and a CP violating phase δ :

$$\begin{aligned}
\begin{pmatrix} d^I \\ s^I \\ b^I \end{pmatrix} &= \begin{pmatrix} V_{ud} & V_{us} & V_{ub} \\ V_{cd} & V_{cs} & V_{cb} \\ V_{td} & V_{ts} & V_{tb} \end{pmatrix} \begin{pmatrix} d \\ s \\ b \end{pmatrix} \\
&= \begin{pmatrix} c_{12}c_{13} & s_{12}c_{13} & s_{13}e^{-i\delta} \\ -s_{12}c_{23} - c_{12}s_{23}s_{13}e^{i\delta} & c_{12}c_{23} - s_{12}s_{23}s_{13}e^{i\delta} & s_{23}c_{13} \\ s_{12}s_{23} - c_{12}c_{23}s_{13}e^{i\delta} & -c_{12}s_{23} - s_{12}c_{23}s_{13}e^{-i\delta} & c_{23}c_{13} \end{pmatrix} \begin{pmatrix} d \\ s \\ b \end{pmatrix}
\end{aligned}$$

where $c_{ij} = \cos \theta_{ij}$ and $s_{ij} = \sin \theta_{ij}$. It is important to note a similar matrix exists for leptons and is used for the study of neutrino oscillations known as the Pontecorvo-Maki-Nakagawa-Sakata (PMNS) matrix but is assumed to be 1 in the standard model.

Higgs Sector

The higgs sector consists of terms related to the single scalar field ϕ that transforms as a doublet of $SU(2)$ $\phi = (\phi^+ \phi^0)$.

$$\mathcal{L}_{higgs} = (D^\mu \phi)^\dagger (D_\mu \phi) + \mu^2 \phi^\dagger \phi + \lambda (\phi^\dagger \phi)^2 \quad (2.4)$$

This sector contains only two free parameters: μ and λ . The two parameters set the minimum and stability of the vaccum of the theory ($\langle \phi \rangle = \nu = \sqrt{\frac{-\mu^2}{\lambda}}$) and set the masses of the fermions and gauge bosons after electroweak symmetry breaking.

2.1.4 Electroweak Symmetry Breaking (EWSB)

Expanding the kinetic term for the field phi about the vaccum $\langle \phi \rangle = \nu$ in the gauged theory we find:

$$(D^\mu \phi)^\dagger (D_\mu \phi) = \frac{1}{\sqrt{2}} \begin{pmatrix} 0 & \nu \end{pmatrix} \left| \partial_\mu + ig \frac{\tau}{2} \cdot W_\mu + i \frac{g'}{2} B_\mu \right|^2 \frac{1}{\sqrt{2}} \begin{pmatrix} 0 \\ \nu \end{pmatrix}$$

Considering the weak gauge term:

$$\tau \cdot W = \begin{pmatrix} W_{\mu,3} & W_{\mu,1} - iW_{\mu,2} \\ W_{\mu,1} + iW_{\mu,2} & -W_{\mu,3} \end{pmatrix}$$

adding in the diagonal B_μ terms and taking the square (ignoring the partial terms)

$$(D^\mu \phi)^\dagger (D_\mu \phi) \supset \frac{\nu^2}{8} [g^2(W_1^2 + W_2^2) + (g'B_\mu - gW_{\mu,3})^2]$$

Now if we perform a redefinition of the gauge fields into mass eigenstates we arrive at a clean expression:

$$\begin{aligned} W_\mu^\pm &= \frac{1}{\sqrt{2}}(W_{\mu,1} \pm iW_{\mu,2}) \\ A_\mu &= \frac{1}{\sqrt{g^2 + (g')^2}}(g'W_{\mu,3} + gB_\mu) = \sin \theta_W W_\mu^3 + \cos \theta_W B_\mu \\ Z_\mu &= \frac{1}{\sqrt{g^2 + (g')^2}}(g'B_\mu - gW_{\mu,3}) = \sin \theta_W B_\mu - \cos \theta_W W_\mu^3 \end{aligned}$$

Here we have defined the electroweak mixing angle θ_W in terms of a right triangle with legs g and g' . With this substitution,

$$\begin{aligned} (D^\mu \phi)^\dagger (D_\mu \phi) &= \frac{\nu^2 g^2}{4} W_\mu^- W_\mu^+ + \frac{(g + g')\nu^2}{8} Z_\mu^2 + (0 \times A_\mu^2) \\ &= \frac{1}{2} m_W^2 W_\mu^- W_\mu^+ + \frac{1}{2} m_Z^2 Z_\mu^2 + (0 \times A_\mu^2) \end{aligned}$$

Electroweak symmetry breaking has generated the mass terms for the gauge bosons! $m_{W^\pm} = \frac{\nu g}{\sqrt{2}} = 90.385$ [GeV], $m_Z = \frac{\nu}{2}\sqrt{g + g'} = \frac{m_W}{\cos \theta_W} = 91.1876$ [GeV] and the massless photon A_μ .

2.1.5 Divergences in the Standard Model

To explain why we need a mechanism like EWSB to generate the masses for the gauge bosons, we need to understand how we have motivated the terms of the Standard Model Lagrangian.

2.1.6 Maxwell's Laws

After, electroweak symmetry breaking we would like to perform a sanity check that we can revive the well established equations of Maxwell governing electrodynamics. Keeping only the terms that contain the field A_μ :

$$\mathcal{L}_{EM} = -\frac{1}{4}F_{\mu\nu}F^{\mu\nu} - ie\bar{\psi}\gamma^\mu A_\mu\psi \text{ for } F_{\mu\nu} = \partial_\mu A_\nu - \partial_\nu A_\mu$$

where by definition $F_{\mu\nu} = \partial_\mu A_\nu - \partial_\nu A_\mu$. Applying the left side of Euler-Lagrange we find (FIX-ME):

$$\partial_\mu \left(\frac{\partial \mathcal{L}}{\partial(\partial_\mu A_\nu)} \right) = -\frac{1}{2}\partial_\mu \left[\left(\frac{\partial}{\partial(\partial_\mu A_\nu)} F_{\mu\nu} \right) F^{\mu\nu} \right] = -\frac{1}{2}\partial_\mu [(1 - \delta_\nu^\mu)F^{\mu\nu}] = -\frac{1}{2}\partial_\mu F^{\mu\nu}$$

The other term is simply $\frac{\partial \mathcal{L}}{\partial A_\mu} = -ie\bar{\psi}\gamma^\mu\psi = J^\mu = (\rho, \vec{J})$. Where ρ is charge density and \vec{J} is current. This yields our first equation:

$$\partial_\nu F^{\nu\mu} = J^\mu \tag{2.5}$$

recognizing the field stress tensor is antisymmetric we can apply a partial derivative and contract with the indices of the 4 dimensions anti-symmetric symbol to obtain:

$$\epsilon_{\theta\rho\mu\nu}\partial\rho F_{\mu\nu} = 0 \tag{2.6}$$

Using these two laws and suggestively defining $E^i = F^{0i}$ and $\epsilon^{ijk}B^k = F^{jk}$ simple substitution

Don't forget that the assumptions to get here were simply the existence of energy terms for the field stress tensor and the fermionic field ψ (here the electron) and geometric arguments about the continuity in the derivative under the $U(1)$ gauge symmetry in the Lagrangian. Everything we understood about electromagnetism naturally arises (including the gauge freedom of the field \vec{A}). Thats just awesome.

2.1.7 Feynman Diagrams

Historically, the outcome of a scattering event in a quantum field theory was incredibly tedious to calculate. One of Feynman's greatest contributions to the field of particle physics was an organizational tool group and quickly calculating terms in the perturbative expansion of the action. The diagrams, which take the form of a directed graph of lines and vertices provided a succinct representation of a complex calculation that was intuitive to work with.

To calculate a given scattering amplitude, one simply constructed all of the applicable diagrams between the incoming particles (say a proton-proton collision) and the outgoing final state say $q\bar{q}$. Lines represented particles and vertices represented interacting terms in the lagrangian where four-momentum conservation was enforced. Internal lines of the diagram (not initial or final state particles) were virtual and were allowed to go off shell.

Let us enumerate the feynman rules for calculating

- External lines:
- Internal lines:
- Vertices:

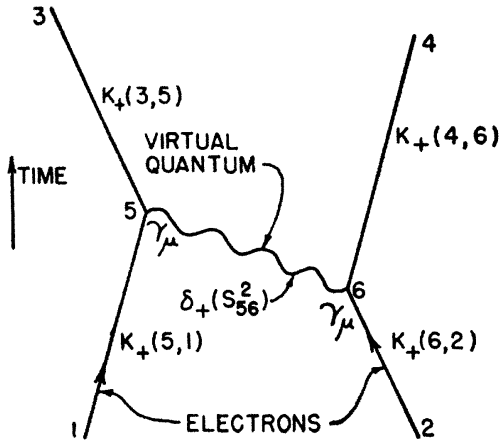


Figure 2.2: The feynman diagram for describing t-channel scattering of two electrons through the echange of a photo. This particular figure was the example used in feynman's original paper describing the pictoral representation of calculating matrix elements. (cite-first-feynman diagram)

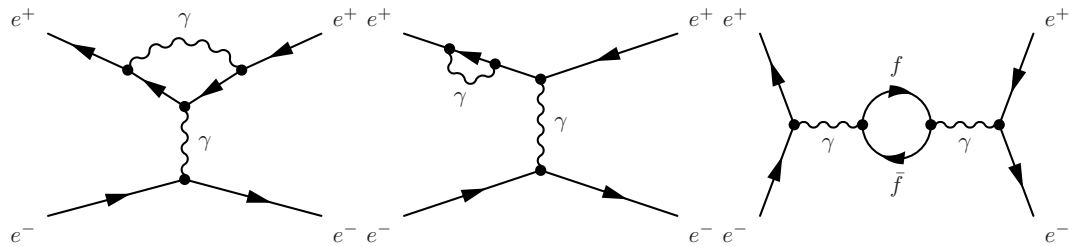


Figure 2.3: Radiative corrections at one loop in electron scattering. The Vertex correction for interaction strength (left). Th self-energy correction for the electron (middle) The photon self-energy correction (right)

- Symmetry Factors:

2.1.8 Radiative Corrections (Loop Diagrams)

The perturbative expansion of the scattering matrix introduces momenta unconstrained by the in-going and out-going particles that must be integrated out in our calculation of a scattering amplitude.

2.2 Beyond the Standard Model

2.2.1 Open Questions and Incompleteness in the Standard Model

- Gravity
- The Hierarchy Problem
- Neutrino Masses The Standard Model does not contain neutrino masses
- Dark Matter There is no fundamental candidate for dark matter observed in the universe
- Stabilization of the Higgs Mass
- UV Completeness
- Strong CP Problem

2.2.2 Supersymmetry

2.3 Long-lived Signatures

2.3.1 Standard Model Particles with Long Lifetimes

The standard model already includes a variety of particles that can generate displaced vertices (Table 2.5 Table 2.6). For example, $B^0 \rightarrow J/\psi K^{*0}$ with $K^{*0} \rightarrow K^+ \pi^-$ generates a 4 track vertex. Such a vertex is commonly utilized in b-tagging. Of particular interest to single displaced jet identification outside of the b-tagging regime are charge neutral SM particles decaying to charged particles with a few centimeter lifetime: Λ^0 , K_S^0 . Such particles would have no track leading to the primary vertex and vertices far outside the b lifetime. The most relevant of processes being:

Name	Content	Particle	Mass [MeV]	τ_0 [sec]	$c\tau$ [cm]
Pion	ud	π^\pm	139	2.6×10^{-8}	7.8×10^2
Kaon	$u\bar{s}$	K^\pm	497	1.23×10^{-8}	3.7×10^2
K Short	$\frac{1}{\sqrt{2}}(d\bar{s} - s\bar{d})$	K_s^0	497	0.896×10^{-10}	2.68
K Long	$\frac{1}{\sqrt{2}}(d\bar{s} + s\bar{d})$	K_L^0	497	5.1×10^{-8}	1.5×10^3
D	$c\bar{d}$	D^\pm	1869	1×10^{-12}	3.0×10^{-2}
B meson	ub	B^\pm	5279	1.6×10^{-12}	4.8×10^{-2}
strange B	$s\bar{b}$	B_s^0	5366	1.5×10^{-12}	4.5×10^{-2}
charmed B	$c\bar{b}$	B_c^0	6275	4.5×10^{-13}	1.4×10^{-2}

Table 2.5: Mesons with proper lifetimes greater than 10^{-2} cm

Name	Content	Particle	Mass [MeV]	τ_0 [s]	$c\tau_0$ [cm]
Lambda	uds	Λ^0	1115	2.6×10^{-10}	7.8
bottom Lambda	edb	Λ_b^0	5620	1.4×10^{-12}	4.2×10^{-2}
Sigma plus	uus	Σ^+	1189	8×10^{-11}	2.4
Sigma minus	dds	Σ^-	1197	1.4×10^{-10}	4.2
Xi zero	uss	Ξ^0	1314	4×10^{-13}	1.2×10^{-2}
Xi minus	dss	Ξ^-	1321	1.6×10^{-10}	4.8
charmed Xi +	usc	Ξ_c^+	2467	4.42×10^{-13}	1.3×10^{-2}
charmed Xi	dsc	Ξ_c^0	2471	1.12×10^{-13}	3.3×10^{-2}
bottom Xi	dsb	Ξ_b^-	5792	1.56×10^{-12}	4.7×10^{-2}
bottom Omega	ssb	Ω_b^-	6054	1.13×10^{-12}	3.3×10^{-2}
Omega minus	sss	Ω^-	1672	8×10^{-11}	2.4

Table 2.6: Baryons with proper lifetimes greater than 10^{-2} cm

1. $K_s^0 \rightarrow \pi^+ \pi^-$ 69% of all K_s^0 decays

2. $\Lambda^0 \rightarrow p \pi^-$ 64% of all Λ^0 decays

Jets containing prompt and non-prompt K_s and Λ^0 will contain tracks with large impact parameters, and large impact parameter significance. When a vertex is fit to the matched tracks we expect small track multiplicity relative to the GeV to TeV long-lived particles this identification targets. It is important to separate this contribution from the detector effects like nuclear interactions.

Particles of a characteristic lifetime τ decay with a falling exponential. For reference, a table describing the percent of decays that will occur at various distances is

Distance (λ)	Probability of Decay
0.01	1%
0.1	9.5%
0.25	22%
0.5	39%
0.75	52%
1	63%
1.5	77%
2	86%
3	95%
5	99.3%

Table 2.7: A reference table for the cumulative probability for a particle of lifetime λ to have decayed after a given distance. Distance is in multiples of lambda.

shown in Table 2.7. Even lifetimes 10 and 100 times the size of the tracker, we would still expect 10% and 1% respectively to occur within the tracker. For particles of lifetime λ we expect 0.6% to decay beyond 5λ .

2.3.2 Split-Susy and Naturalness at the LHC

The expectation of discovering supersymmetry (SUSY) at the TeV scale has been largely motivated by arguments based on naturalness. Since the mass of the Standard Model Higgs boson is sensitive to the high energy scale where SUSY is broken (m_{SUSY}), its mass, of order the electroweak scale, ($m_h \approx m_{EW} \ll m_{SUSY}$) would need to be tuned to order m_{EW}^2/m_{SUSY}^2 . To avoid fine-tuning, we would like $m_h^2 \approx m_{SUSY}^2 \implies m_{SUSY} \leq 1$ TeV. More specifically, knowing $m_H \approx 125$ GeV we expect light SUSY partners (in particular, light stops) near < 1 TeV to stabilize the quadratic divergences of 1 loop corrections to the Higgs mass [citation:*light_stops*].

Unfortunately these scalar partners have yet to be discovered.

It is important to note that the stability of the Higgs boson mass is not the only fine-tuning problem in particle physics. When the same argument is made for the cosmological constant we arrive at $\Lambda \geq m_{SUSY}^4$, where experimentally $\Lambda = 10^{-59}$

TeV⁴. If we use the same SUSY scale as we did for the Higgs mass, $m_{SUSY} = 1$ TeV we have a new fine tuning problem of 10^{60} .

As addressed by Arkani-Hamed and Dimopoulos [citation:*nima_lhc*], many theoretical approaches have been motivated by a natural explanation for the Higgs mass while separately seeking an explanation of the cosmological constant through some other mechanism. Arkani-Hamed and Dimopoulos propose a reconsideration of naturalness, entertaining the idea that fine tuning could have a role to play in beyond the Standard Model physics. Conceivably, both Λ and m_h fine tuning could be resolved by the same mechanism. This un-natural model was further investigated by Giudice and Romanino [citation:*split_susy*] and dubbed “split supersymmetry”.

Split SUSY assumes a much higher SUSY scale $m_{SUSY}^2 \gg 1$ TeV where all scalars (excluding the Higgs) become very heavy $O(m_{SUSY})$ and the lightest sparticles (Higgsinos and gluinos) are kept at the TeV scale by requiring the lightest neutralino to be a good dark matter candidate.

Because the scalars are so much heavier, the decay of gluinos through squarks is suppressed. The characteristic signature of split supersymmetry is thus long-lived gluinos; such processes with long lifetimes are rare in the SM.

2.3.3 Hidden Valley Models

Chapter 3

Collider Physics and Phenomenology

3.1 Introduction

In the previous chapter, we outlined how we reach a theory like the standard model from fundamental principles, but a considerable amount of physics is required to reach a practical theoretical description of what occurs inside of the experiment. The goal of this section is to connect the matrix elements \mathcal{M} from the quantum field theoretic description of the Standard Model to the Monte Carlo simulations used to test a given theory. First, we will discuss the how we can compare the matrix amplitudes with the observations in a physical detector. After, we will the discuss the considerations that must be made for the fact the LHC collides hadrons rather than fundamental particles. Finally, we will discuss the framework used to describe the particles actually observed in the detector after the hard scattering occurs where perturbative physics breaks down and calculations from first principles cannot be performed. Generic principles for parton showering and hadronization models will be examined.

3.2 From Matrix Elements to Cross Sections

In high energy experimental particle physics the key quantity (besides particle quantum numbers and masses) is the cross section σ of the process. This is the rate or in essence, the probability that an event occurs. It is the proportionality between the number of observed collisions and the rate at which the Large Hadron Collider delivers collisions L (the luminosity) expressed simply as:

$$N_{events} = L \times \sigma$$

site-peskin Consider a target of particles type A and density ρ_A and aim particles type B with density ρ_B . If the lengths of the bunches of particles are l_A and l_B then the cross section of the processes is defined for a beam with cross-sectional area as:

$$\sigma \equiv \frac{N_{events}}{\rho_A l_A \rho_B l_B A}$$

Inverting this and assuming that we have constant density along the beams length:

$$N_{events} = \frac{\sigma N_A N_B}{A} = \sigma N_A n_B \quad (3.1)$$

by comparing this with the relation for N_{events} above containing luminosity, we see the luminosity is in effect counting the number of colliding particles per unit area. More incident particles and a more focused beam means more scattered events. In the last equality we have introduced the impact parameter density n_B for the incident B particles.

However, the the end results of feynman diagram calculations yield scattering amplitudes which are matrix elements of scattering a given intial state into a given final state, not a cross section. We have to further develop the stocastic interaction of two particles into something more concrete experimentally.

First, we need must think about the quantum fields within the beams that are colliding. To do so we set up two initial wave packets A and B in a limit of definite momentum p_A and p_B and evolve them for a very long time with the time evolution operator $\exp(-iHt)$ and then consider the final state wave packets with the correct final state particles. This in turn will give us the probability amplitude for producing that final state.

$$\mathcal{P} = |\langle \phi_1 \phi_2 \dots | \phi_A \phi_B \rangle|^2$$

Now consider the number of incident particles colliding along the z -axis, but with non-trivial transverse displacement, also referred to as impact parameters b_i . We will take the perspective that A is a target and B is collinear with the target and account for the shift in position with an explicit factor of $\exp(-ib \cdot k_B)$. The properly normalized expression then reads:

$$|\phi_A \phi_B\rangle = \int \frac{d^3 k_A}{\sqrt{2E_A}(2\pi)^3} \int \frac{d^3 k_B}{\sqrt{2E_B}(2\pi)^3} \phi_A(k_A) \phi_B(k_B) e^{-ib \cdot k_B}$$

For a single target A and a beam B with constant impact parameter density $n_B = N_B/A$ we can write the the number of events as

$$N_{events} = \sum_{\text{incident particles } i} \mathcal{P}_i = \int d^2 b n_B(b) \mathcal{P}(b) = n_B \int d^2 b \mathcal{P}(b)$$

Comparing this to Equation 3.1 we can write the cross section as:

$$\sigma = \int d^2 b \mathcal{P}(b)$$

and the properly normalized differential cross section for scattering into a the infinitesimal final state momentum element is:

$$d\sigma = \left(\prod_f \frac{d^3 p_f}{(2\pi)^3 2E_f} \right) \int d^2 b \left(\prod_{i=A,B} \int \frac{d^3 k_i}{(2\pi)^3 \sqrt{2E_i}} \phi_i(k_i) \int \frac{d^3 \bar{k}_i}{(2\pi)^3 \sqrt{2\bar{E}_i}} \phi_i^*(\bar{k}_i) \right) \\ \times e^{ib \cdot (\bar{k}_S - k_B)} |\langle \{p_f\} | \{k_i\} \rangle|^2$$

We have 6 dummy integrals to do in \bar{k} over the 3 momentums of particle A and B so count our delta functions. The $d^2 b$ integral gives 2 delta functions in the transverse momentum $(2\pi)^2 \delta^2(k_B^\perp - \bar{k}_B^\perp)$. We have 8 delta functions from the matrix element enforcing that the process to conserve energy and momentum $\delta^4(k_A + k_B - \sum p_f)$ and in the complex conjugate with the dummy variable \bar{k} : $\delta^4(\bar{k}_A + \bar{k}_B - \sum p_f)$. Performing the transverse integrals in \bar{k}_B sets $\bar{k}_B^T = k_B^T$ which in combination with the transverse barred amplitude delta functions give $\bar{k}_A^T = k_A^T$. The remaining 2 integrals in z require some properties of delta functions:

$$\int d\bar{k}_A^z d\bar{k}_B^z \delta(\bar{k}_A^z + \bar{k}_B^z - \sum p_f^z) \delta(\bar{E}_A + \bar{E}_B - \sum E_f)$$

We can integrate the first B integral considering \bar{k}_B^z to be a function of \bar{k}_A^z and writing the barred energy terms in the momentums and masses:

$$\int d\bar{k}_A^z \delta \left(\sqrt{\bar{k}_A^2 + m_A^2} + \sqrt{\bar{k}_B^2 + m_B^2} - \sum E_f \right)$$

We now need to use the property that $\delta[f(x)] = \sum_i (\delta(x_i)/|f'(x_i)|)$ where x_i are the zeros of the function $f(x)$. Note that given our parameterization from the first delta

function $\partial_{\bar{k}_A^z}(\bar{k}_B^2) = -2\bar{k}_B^z$.

$$\begin{aligned} & \int d\bar{k}_A^z \left(\frac{1}{2} \frac{2\bar{k}_A}{\sqrt{\bar{k}_A^2 + m_A^2}} - \frac{1}{2} \frac{2\bar{k}_B}{\sqrt{\bar{k}_B^2 + m_B^2}} \right)^{-1} \delta(\bar{E}_A + \bar{E}_B - \sum E_f) \\ &= \int d\bar{k}_A^z \frac{1}{\frac{\bar{k}_A}{E_A} - \frac{\bar{k}_B}{E_B}} \delta(\bar{E}_A + \bar{E}_B - \sum E_f) = \frac{1}{\beta_A - \beta_B} \end{aligned}$$

The 6 remaining integrals in k_A and k_B remain:

$$\begin{aligned} d\sigma = & \left(\prod_f \frac{d^3 p_f}{(2\pi)^3 2E_f} \right) \frac{|\mathcal{M}|^2}{2E_A 2E_B |\beta_A - \beta_B|} \int \frac{d^3 k_A}{(2\pi)^3 \sqrt{2E_i}} |\phi_A(k_A)|^2 \\ & \times \int \frac{d^3 k_B}{(2\pi)^3 \sqrt{2E_i}} |\phi_B(k_B)|^2 \delta^4(k_A + k_B - \sum p_f) \end{aligned}$$

To proceed further, we must consider the quality of measurements made by particle detectors. Real detectors cannot measure arbitrarily small spreads in the momentums $k_A + k_B$. The measurements made in a realistic experimental setup are not sensitive to the spread of momentum in the initial wave packets ϕ_A and ϕ_B . Given this, we can take the central value $k_A + k_B = p_A + p_B$ to be a good approximation for the delta function. With this approximation, we can move the delta function outside the integral and perform the integrals using the unit normalization condition of the two fields ϕ_i :

$$d\sigma = \left(\prod_f \frac{d^3 p_f}{(2\pi)^3 2E_f} \right) \frac{|\mathcal{M}|^2}{2E_A 2E_B |\beta_A - \beta_B|} (2\pi)^4 \delta^4(p_A + p_B - \sum p_f) \quad (3.2)$$

Let's consider the simple case of $2 \rightarrow 2$ scattering and use the energy delta function of the 4 remaining delta functions to compute integral over the final state. To do so, we go to the center of mass frame where $|p_1| = |p_2| = P$, $\vec{p}_1 = -\vec{p}_2$, $E_{cm} = 2P$. We

first integrate p_2 to invorce 3-momentum conservation

$$\int \left(\frac{d^3 p_1}{(2\pi)^3 2E_1} \right) \left(\frac{d^3 p_2}{(2\pi)^3 2E_2} \right) (2\pi)^4 \delta^4(P - \sum p_f)$$

now switching to a spherical integral with a jacobian $p_1^2 dp_1 d\Omega$ where $d\Omega$ is and infinitesimal solid angle.

$$\int \frac{dp_1 p_1^2 d\Omega}{(2\pi)^3 (2\pi)^3 2E_1 2E_2} (2\pi) \delta(E_{cm} - E_1 - E_2)$$

here we use the same delta function identity to obtain:

$$\begin{aligned} \int d\Omega \frac{p_1^2}{(2\pi)^2 2E_1 2E_2} \left(\frac{p_1}{E_1} + \frac{p_2}{E_2} \right)^{-1} &= \int d\Omega \frac{p_1^2}{(2\pi)^2 2E_1 2E_2} \left(\frac{E_1 E_2}{p_1(E_1 + E_2)} \right) \\ &= \int d\Omega \frac{p_1}{16\pi^2 E_{cm}} \end{aligned}$$

Combining the result for the final state integral with Equation 3.2:

$$\left(\frac{d\sigma}{d\Omega} \right)_{CM} = \frac{1}{2E_A 2E_B |\beta_A - \beta_B|} \frac{p_1}{16\pi^2 E_{cm}} |\mathcal{M}|^2$$

Now if we assume the masses of the four particles are the same (or negligible at the energies involved) and substitute $\beta = p/E$:

$$\left(\frac{d\sigma}{d\Omega} \right)_{CM} = \frac{|\mathcal{M}|^2}{64\pi^2 E_{cm}^2}$$

This is the relation between the rate at which a detector will observe a $2 \rightarrow 2$ process proportional to the matrix element derived from the feynman diagrams governing the process.

3.3 Luminosity

$$L = \frac{f}{\pi} \frac{N_p N_{p^c}}{n_b} \frac{\gamma}{\sqrt{\beta_x^* \beta_y^* E_x^* E_y^*}} \quad (3.3)$$

- f : revolution frequency of the beams.
- N_p the number of protons in the beam
- n_b the number of proton bunches
- $\beta_{x,y}^*$ the transverse wavelengths of the beatatron oscillations
- $E_{x,y}^*$ the transverse emittance of the beams
- γ : relativistic factor

To increase luminosity, this parameterization tells us we want a high frequency of collisions, high proton density within the bunches, small oscillations transverse to the ideal path, and a small average spread in position momentum space. The small spread in phase space (low emittance) means the particles are confined to a small area and have roughly the same momentum. This results in a high probability of interaction.

3.4 Parton Model of Hadron Collisions

cite:qcd-collider-physics-ellis

For a collision of two protons like that of the LHC (or proton anti-proton for Tevatron) the hard scattering process is not between the individual hadrons, but hadron's inner structure: the quarks and gluons. Unlike, a lepton collider, where the full four vector is controlled by the collider, the energy of any given hard hadron-hadron scattering process is probabilistic in nature, as the individual partons have some unknown fraction of the proton energy.

The cross section for a process for two hadrons with four-momentum P_1 and P_2 can be written:

$$\sigma(P_1, P_2) = \sum_{i,j} \int dx_1 dx_2 f_i(x_1, \mu) f_j(x_2, \mu) \hat{\sigma}_{ij}(p_1, p_2, \alpha_S(\mu), Q) \quad (3.4)$$

where the momentum of the partons participating in the hard interaction are $p_i = x_i P_i$ $i = 1, 2$. The scale of the hard scattering is denoted by Q . This would be m_W for W boson production. The f_i are the quark or gluon distributions within the protons. These are the parton distribution function (PDFs). The short distance cross section $\hat{\sigma}$ can be calculated as a perturbative series in the asymptotically small running QCD coupling α_S . The factorization scale μ is an arbitrary parameter that is chosen as the boundary between the long and short distance interaction physics. The boundary at μ separates the soft emitted partons that should be considered part of the hadron and the partons emitted at large transverse momentum that should be considered part of the hard process. In general, this be set near the order of the process scaled Q .

If we consider the ratio of the actual $\sqrt{\hat{s}}$ of the hard process relative to the proton \sqrt{s} we define τ , the loss of energy between the COM collision of the proton and the individual partons

$$\frac{s}{\hat{s}} = \frac{(p_1 + p_2)^2}{(x_1 p_1 + x_2 p_2)^2} = \frac{2p_1 \cdot p_2}{2x_1 x_2 p_1 \cdot p_2} = \frac{1}{x_1 x_2} = \frac{1}{\tau}$$

Now lets consider the total cross section σ_{TOT} which consists of the parton luminosity L_{ij} for two individual partons i and j and the corresponding cross sections σ_{ij} . We assume that the cross section $\hat{\sigma}$ is only a function of \hat{s} , (a property that holds true for many processes, but not in general). Let τ_0 be the minimum τ at which the process

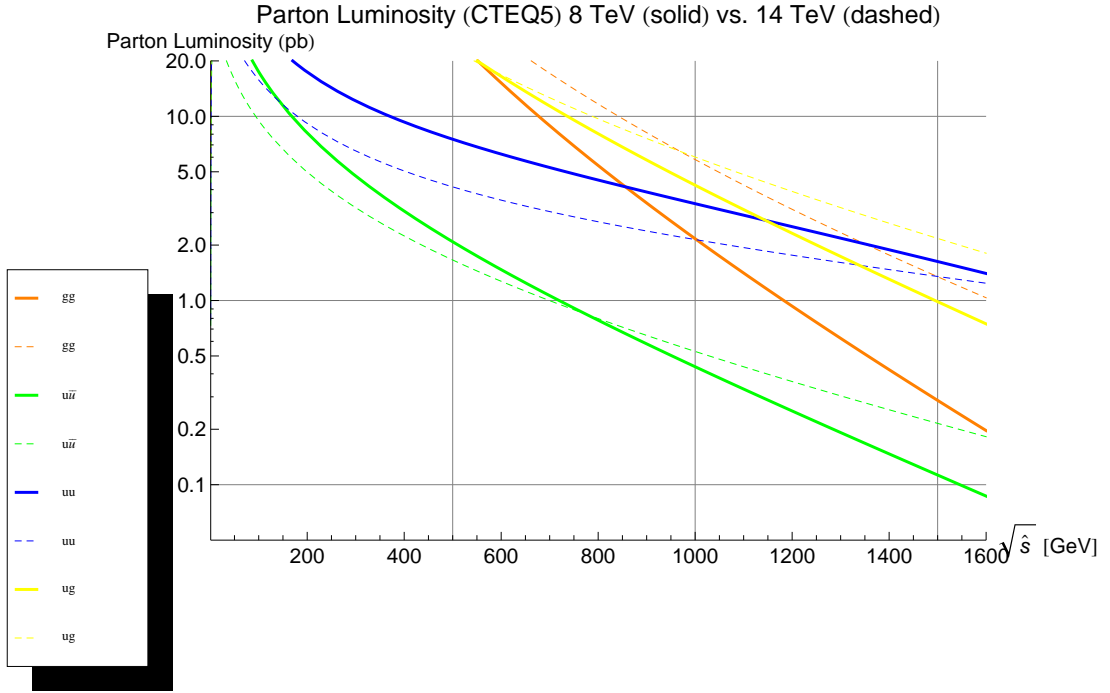


Figure 3.1: Contours of the parton luminosity function derived from CTEQ5 parton distribution functions for $\sqrt{s} = 8$ TeV and $\sqrt{s} = 14$ TeV. Contours are separated by collisions the individual partons in the collision.

can occur.

$$\begin{aligned}\sigma_{TOT} &= \sum_{i,j} \sigma_{ij} L_{ij} = \sum_{i,j} \int_{\tau_0}^1 \frac{dL_{ij}}{d\tau}(1) \hat{\sigma}_{ij} d\tau \\ &= \sum_{i,h} \int_{\tau_0}^1 \frac{dL_{ij}}{d\tau} d\tau \left(\frac{\hat{s}}{s\tau} \right) \hat{\sigma}_{ij} = \sum_{i,j} \int_{\tau_0}^1 \frac{d\tau}{\tau} \left(\frac{1}{s} \frac{dL_{ij}}{d\tau} \right) (\hat{s} \hat{\sigma}_{ij})\end{aligned}$$

Here the center term is referred to as the parton luminosity function and contains the parton distribution functions with some extra accounting for the parton types to avoid double counting:

$$\tau \frac{dL_{ij}}{d\tau} = \frac{1}{1 + \delta_{ij}} \int_0^1 dx_1 dx_2 \times [(x_1 f_i(x_1, \mu^2) x_2 f_j(x_2, \mu^2)) + (1 \leftrightarrow 2)] \delta(\tau - x_1 x_2)$$

3.5 Kinematic Conventions for Collider Physics

In experimental particle physics, due to cylindrical symmetry of our detectors it is preferable to make a change from a cartesian energy and momentum parameterization to rotationally-symmetric parameterization about the collision access. Furthermore, since the center of mass frame between the two colliding particles is generally moving relative to the lab frame, we would like parameterization of our problem which is invariant under longitudinal boosts. First, we will motivate using hyperbolic functions of rapidity to parameterize energy and momentum. Let's recall define the hyperbolic trigonometric functions:

$$\cosh(x) = \frac{e^x + e^{-x}}{2} , \quad \sinh = \frac{e^x - e^{-x}}{2}, \text{ and } \tanh^{-1} x = \ln \left(\sqrt{\frac{1+x}{1-x}} \right)$$

combining \cosh and \tanh^{-1} conveniently gives the relativistic γ factor for $x = \beta$:

$$\cosh(\tanh^{-1} x) = \frac{1}{2} \left(\sqrt{\frac{1+x}{1-x}} + \sqrt{\frac{1-x}{1+x}} \right) = \frac{1}{2} \left(\frac{(1+x) + (1-x)}{\sqrt{1-x^2}} \right) = \frac{1}{\sqrt{1-x^2}}$$

and similarly derived:

$$\sinh(\tanh^{-1} x) = \frac{x}{\sqrt{1-x^2}} = x\gamma(x)$$

If we define $w = \tanh^{-1}(\beta)$ we can conveniently write the energy and momentum as:

$$E = \gamma m = m \cosh w$$

$$|p| = \gamma m \beta = m \sinh w$$

Now lets re-write a lorrentz boost γ along the z-axis in terms of w :

$$E' = \gamma(E - \beta p_z) = E \cosh w - p_z \sinh w p'_z = \gamma(p_z - \beta E) = p_z \cosh w - E \sinh w \quad (3.5)$$

We now set $w = y = \tanh^{-1}(\beta_z^*)$ where β_z^* is the boost required to reach the frame where the particle is moving only transversely to the beamline p_μ^* . We can then reach the lab frame by performing the transformation from the $*$ frame. First lets write the four vector in the $*$ frame

$$\begin{aligned} p_\mu^* &= (E, p_x, p_y, 0) = (\sqrt{p_T^2 + m^2}, p_T \sin \phi, p_T \cos \phi, 0) \\ &\rightarrow p_\mu^{lab} = (m_T \cosh y, p_T \sin \phi, p_T \cos \phi, m_T \sinh y) \end{aligned}$$

where $m_T = \sqrt{m^2 + p_T^2}$, $p_T = \sqrt{p_x^2 + p_y^2}$, and y is the definition of rapidity generally used in particle physics. In the limit of light masses relative to the transverse energy of a collision, as is generally the case for collisions at the Large Hadron Collider:

$$p^\mu = p_T(\cosh \eta, \sin \phi, \cos \phi, \sinh \eta)$$

From the experimental perspective, what is most important about this definition is that there is a simple geometric relation between pseudorapditiy and the angle of the particle relative to the beam line. To see this, we go back to the definition of rapidity and take $\beta \rightarrow 1$ or equivalently $|p| = E$:

$$y = \tanh^{-1}(\beta_z^*) = \ln \left(\sqrt{\frac{1 + \beta_z^*}{1 - \beta_z^*}} \right) \approx^{\beta \rightarrow \infty} \ln \left(\sqrt{\frac{1 + p_z/|p|}{1 - p_z/|p|}} \right)$$

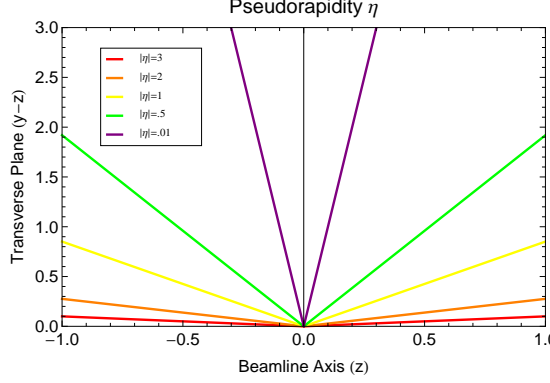


Figure 3.2: Lines of constant pseudorapidity in the z-y plane

Now if we consider the angle with the beamline in the lab frame θ we use a half angle trigonometric identity.

$$1 + \cos \theta = 1 + \frac{p_z}{|p|} = 2 \cos^2(\theta/2)$$

$$1 - \cos \theta = 1 - \frac{p_z}{|p|} = 2 \sin^2(\theta/2)$$

combining this with the approximation with massless limit of y we obtain pseudorapidity η :

$$\eta = \ln \left(\sqrt{\frac{\cos^2(\theta/2)}{\sin^2(\theta/2)}} \right) = -\ln \left(\tan \frac{\theta}{2} \right)$$

The energies of particles at the LHC are typically negligible in mass relative to their energies and the approximation $\eta \approx y$ is accurate. This has a number of useful applications. Firstly, differences in rapidity are invariant under longitudinal Lorentz boosts along the beam axis which can be seen by applying the transformation in terms of γ factors to $y_1 - y_2$ as found in Equation 3.5. Given this relation, pseudorapidity provides an intuitive geometric interpretation as the angle from the beam axis. The ray extending directly transverse from the collision point is $\eta = 0$ with symmetric

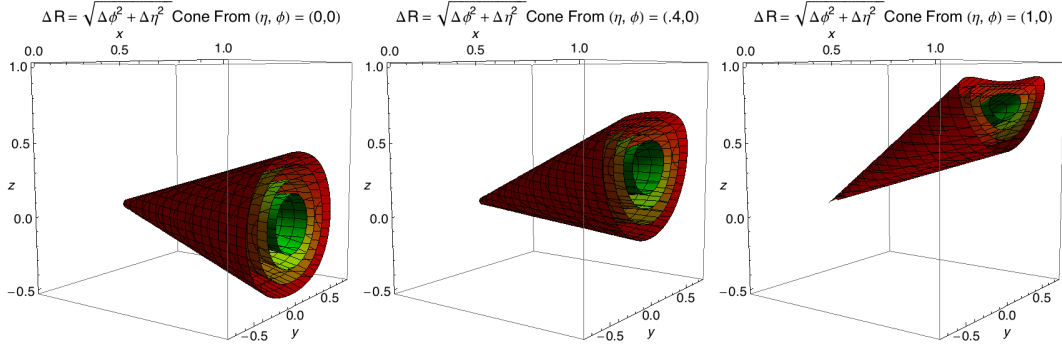


Figure 3.3: Contours of constant ΔR from the $\eta_0, \phi_0 = 0, 0$

values $\pm |\eta|$ to either side of this ray along the z-axis Figure 3.2.

$$\Delta R = \sqrt{(\Delta\phi)^2 + (\Delta\eta)^2}$$

Fixed values of ΔR form a solid angle “cone” extending from the interaction point outward. This can be seen by using our definition of η to convert from cylindrical coordinates to (x, y, z) and consider the distance relative to the point (η_0, ϕ_0)

$$\Delta R = \sqrt{(\phi_0 - \tan^{-1}(y/x))^2 + \left(\eta_0 + \log\left(\tan\frac{\cos^{-1}(z/\sqrt{x^2 + y^2})}{2}\right)\right)^2}$$

3.6 Showering

After the initial hard process is simulated, even if performed at high orders in perturbation theory, we have not described the large multiplicity and variety of particles which result from the showering of free quarks (Fig. 3.4). We might even take for granted (as experimentalists that is) that high energy proton collisions yield collimated showers of hadrons we more commonly refer to as *jets*.

As the collisions are made between hadrons, the dominant fraction of the total cross section is governed by the dynamics of QCD. The strength of QCD is set by

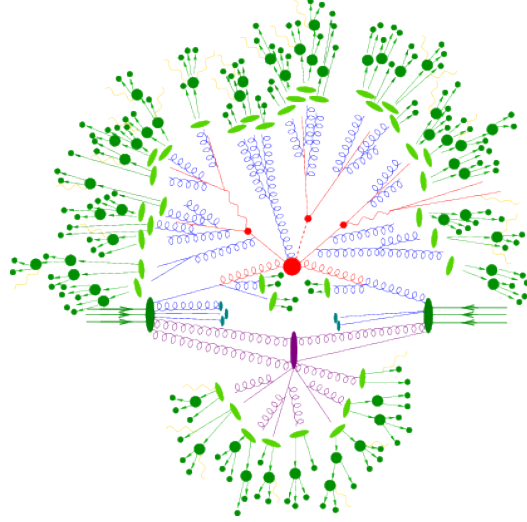


Figure 3.4: A graphic depiction of the showering and hadronization process. The incoming protons can be seen as the two sets of three incoming arrows representing the proton quark content.

the strong coupling $\alpha_s(q^2)$ where the q^2 dependence arises from loop corrections to the tree level feynman diagram vertices (cite-tully).

$$\alpha_s(q^2) = \frac{12\pi}{(33 - 2n_f) \ln(q^2/\Lambda_{QCD}^2)} \quad (3.6)$$

Here n_f is the number of flavors of participating fermions in the interaction and $\Lambda_{QCD} = 0.1 - 0.3$. Here we notice two important features. As q^2 becomes large, the interaction becomes asymptotically weak and the physics is perturbative. As $q^2 \rightarrow \Lambda_{QCD}$ the theory is strongly coupled ($\alpha > 1$) and a perturbative approach leaves higher order terms that cannot be neglected (cite-ellis-qcd).

We need a method to evolve the high energy states to some low energy cut off where the physics is clearly non-perturbative. This scale is typically taken to be on the order of momentum transfer $t^2 = 1 \text{ GeV}^2$. This constitutes a natural division of labor for generating physics events between the perturbative hard scattering, the approximately perturbative showering, and the non-perturbative physics of hadronization. The terms fragmentation and hadronization are often used interchangeably to describe

the non-perturbative of this division. However, in certain contexts, hadronization can refer to both the parton showering as well as hadron formation.

In experimental high energy particle physics the term Monte Carlo (MC) is used as a short hand for simulated physics samples, however the Monte Carlo method of generating these samples means something specific. Monte Carlo methods generally rely on using random numbers to simulate

(cite-ellis-qcd) The monte carlo method of generating parton branching is stated as: given some virtual mass scale t_1 and momentum fraction x_1 generate (t_2, x_2) after one step in the branching evolution. To perform this step-wise evolution of the parton branching we need shower evolution equations.

(cite-mrenna-showering) Consider the branching of a particle a : $a \rightarrow bc$ with a momentum scale Q^2 . We denote energy and momentum fraction imparted to particle b as z such that particle c receives $1 - z$. We introduce the momentum transfer variable motivated by Equation 3.6 $t = \ln(Q^2/\Lambda^2)$ yielding a differential element $dt = d\ln(Q^2) = dQ^2/Q^2$. The differential probability for the particle a to branch is given:

$$d\mathcal{P} = \sum_{b,c} \frac{\alpha_{abc}}{2\pi} P_{a \rightarrow bc}(z) dt dz$$

where the sum is over all possible branchings and α is the appropriate coupling (α_{EM}, α_S) for the branching evaluated at the appropriate scale. We enumerate the kernels that map the momentum fraction from splitting to the possible states after

branching:

$$\begin{aligned}
P_{q \rightarrow qg}(z) &= C_F \frac{1+z^2}{1-z} & P_{q \rightarrow q\gamma}(z) &= e_q^2 \frac{1+z^2}{1-z} \\
P_{g \rightarrow gg}(z) &= N_C \frac{(1-z)(1-z)^2}{z(1-z)} & P_{l \rightarrow l\gamma}(z) &= e_l^2 \frac{1+z^2}{1-z} \\
P_{g \rightarrow q\bar{q}}(z) &= T_R(z^2 + (1-z)^2)
\end{aligned}$$

where $C_F = 4/3$ is a color factor, N_C is the number of colors in QCD, $T_R = n_f/2$ is half the number of allowed $q\bar{q}$ flavors. e_i^2 is the charge squared of the quark or lepton.

Lets define an integral over the probability distribution for some fixed t between the minimally allowable momentum fraction z_- and the maximum z_+ as:

$$\mathcal{I}_{a \rightarrow bc}(t) = \int_{z_-(t)}^{z_+(t)} dz \frac{\alpha_{abc}}{2\pi} P_{a \rightarrow bc}(z)$$

From this here we can find the total probability of branching as a sum over the possible branching states $p_{branch} = \sum_{bc} \mathcal{I}_{bc}(t)$. If we consider the probabiity of no branching occurring $(1 - p_{branch})$ in some finite interval (t, t_0) as the product of differential time steps δt , we obtain an exponential:

$$\begin{aligned}
\mathcal{P}_{no-branch}(t_0, t) &= \prod_{\delta t \in (t, t_0)} (1 - p_{branch}) \approx \lim_{N \rightarrow \infty} \sum_{k=0}^N \frac{N!}{(N-k)!k!} 1^{N-k} (-p_{branch})^k \\
&= \sum_{k=0}^{\infty} \frac{1}{k!} (-p_{branch})^k = \exp(-p_{branch})
\end{aligned}$$

Such that the total probability of not branching within a givern t interval is given:

$$\mathcal{P}_{no-branch}(t_0, t) = \exp \left(- \int_{t_0}^t dt' \sum_{b,c} \mathcal{I}_{a \rightarrow bc}(t') \right) = S_a(t)$$

Where we have introduced the notation $S_a(t)$ for what is referred to as the Sudakov form factor (cite-sudakov). With this single parameterization we can write the probability of not branching as a ratio of $S_a(t)$ functions (since the ratio of exponentials will just alter the integral bounds):

$$\mathcal{P}(t_2, t_1) = \frac{S_a(t_2)}{S_a(t_1)}$$

Note here that t is not time, but rather serves a proxy for time, where the final state showering occurs from an intial t_{max} set by the hard scattering and progressively becomes smaller through the branching process.

The Monte Carlo process generates a random number \mathcal{P} and solves for t_2 in terms of t_1 . The process is then applied to the newly branched particles b and c . If t_2 is smaller than the scale set for hadronization, then the showering process terminates. Eventually from the monotonicity of t_i the cascade terminates and the generation process is handed off to hadronization.

3.7 Hadronization

When the quark model, the eight-fold way, was originally introduced in 1961, it was a large simplification of the space of observed particles. Each combination of possible light quarks was observed in nature (the third generation had not yet been discovered). However, a single “bare” quark had never been observed despite experimental efforts. Today we understand that it is the inherent nature of the strong force that prevents light quarks from being liberated from their hadronic bound states. The discovery of the top quark, who’s width is larger than Λ_{QCD} , will decay before hadronization takes place allowing for the study of a “bare” quark. In this section, we briefly discuss the way monte carlo simulation models the non-perturbative confinement of quarks.

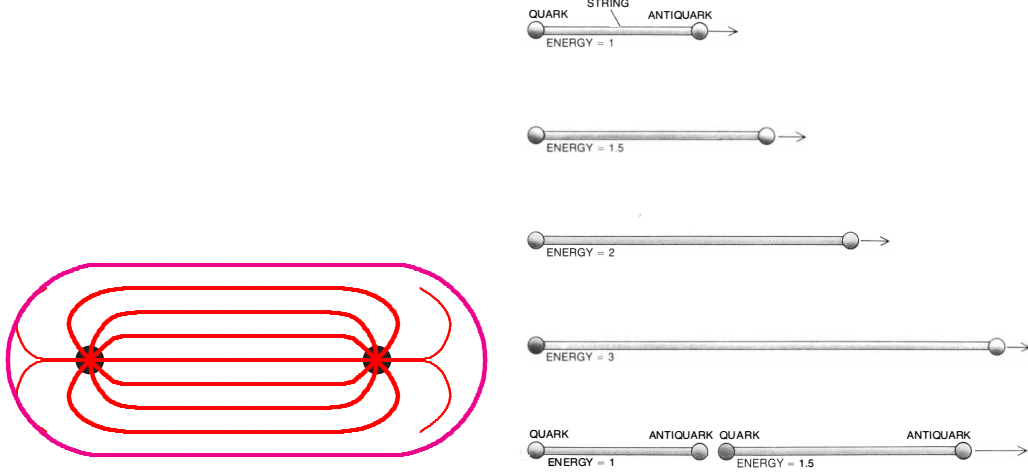


Figure 3.5: The flux between a quark and anti-quark

(cite-ellis) When we leave the showering process, we are left with a large number of virtual particles on the order of the cutoff t_{min} . Although this parameter is unrelated to the hadronization process, an ideal hadronization model would use the chosen value of t_{min} to compensate for effects of having a hard cutoff value for the showering. As t_{min} is increased, there are fewer particles that are increasingly off-shell. These virtual particles should be able to hadronize, however, the favored values of t_{min} to begin the hadronization step tend to be a few times the scale of hadronization $\Lambda_{QCD} \approx 0.1 - 0.3$ GeV. This is suggestive that the extensions of perturbation theory are more reliable than models of hadronization.

(cite-mc-review) It is important to state that there are only models of hadronization and no calculations from first principles. Even lattice QCD calculations which are made on euclidean space times fail for processes which are inherently minkowskian such as hadron formation. Two main categories of hadronization models exist. The string model which transforms virtual particles directly into hadrons and the cluster model which uses an intermediate clustering step.

The string model, the most well known of which is the Lund String Model (cite-lund-string), relies on an assumption of linear confinement. One expects a linear

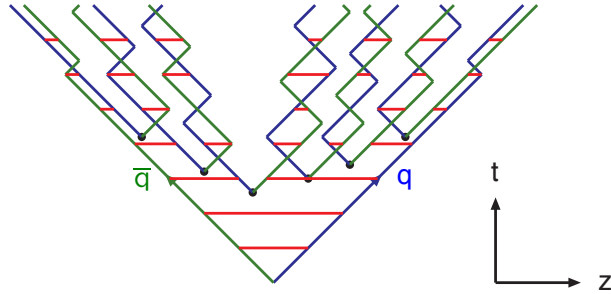


Figure 3.6: The flux between a quark and anti-quark (left) (cite-string-stretch)

potential $V(r) = \kappa r$ at long distances, where the string constant $\kappa \approx 1$ GeV/fm $\approx .2$ GeV 2 . In general, there is an additional coulomb potential at shorter distances, but it is an assumption of the Lund model that this term is negligible. It is important to note that string model of hadronization should not be confused with the string theory where strings serve as the fundamental . The linear confinement of QCD is best visualized as a color flux tube being stretched between a quark and anti-quark (Figure. 3.6). As the two quarks are increasingly separated in space, the flux tube is stretched maintaining constant energy per unit length κ . The lorentz covariant and causal description of this energy flow uses a massless one dimensional string that parameterizes the axis of a cylindrically symmetric flux tube.

In the simple case of quark anti-quark production, the two quarks separate from each other along the z axis and the potential energy stored in the string increases. When the potential energy is large enough, the string can break through the production of a new quark anti-quark pair. These breaks typically occur between 1 and 5 fm in the rest frame of the pair, however in the lab frame these processes highly length contracted. After the break, widening regions of no flux arise.

The string model contains a large number of parameters related to flavor properties and must be determined from data

The cluster model is based on the precontainment properties of parton showers which lead to color singlet clusters. The cluster hadronization begins with non-

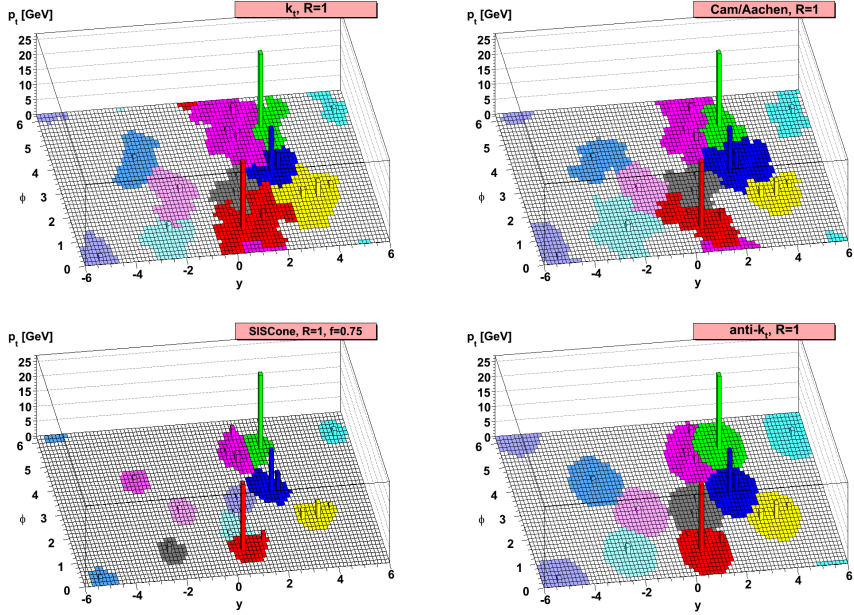


Figure 3.7: Comparisons made between varied clustering algorithms.

perturbative splitting of gluons into quark anti-quarks pairs. Clusters are formed from color-connected pairs. Most clusters undergo two body phase-space decays, with heavier clusters decaying first to lighter clusters. Cluster models tend to describe the data less accurately than string models, but using fewer parameters.

The incredibly dense and active environment of hadronic collisions could lead to significant collective effects which are not considered in current hadronization models.

3.8 Hadron Decay

3.9 Jet Clustering

Once the showering and hadronization have constructed the final state particles we need a way of clustering the numerous deposits or particles in the final state simulation and data. While in simulation one can trace the hadrons back through their branching

tree to their mother particle from the hard interaction, data has no truth information. This problem necessitates a fast algorithm that takes as input energy deposits in the detector and outputs clusters with kinematic properties representative of the hard scattering process quarks and gluons.

Any desirable clustering algorithm must satisfy collinear and infrared safety. An algorithm that is collinear safe, is insensitive to the

The most commonly utilized clustering algorithm is anti-kt (Figure 3.7) which takes a size parameter R corresponding the $(\Delta R)^2 = (\Delta\eta)^2 + (\Delta\phi)^2$. The resultant four momentum of the cluster is given by the four-momentum sum of the individual deposits.

Jets must be calibrated in data to account for energy lost. Common techniques include

Additionally as luminosity increases and there are increasingly more interactions per event, jets must be corrected for additional clustered energy not related to the primary interaction. For this, an average energy density ρ is calculated event by event and $\rho \times A$ is subtracted from the jet energy where A is the jet area.

For 2015 data, at $\sqrt{s} = 13$ TeV the size parameter for the displaced jets analysis was fixed at a cone size $R = 0.4$. Larger size parameters as well as different algorithms are utilized for boosted hadronic decays of bosons,

Chapter 4

CERN Laboratories

4.1 Financial and Organizational Structure

4.1.1 Funding Model

The CERN operating budget provided by the individual member states. The size of the contribution is determined:

“using the arithmetic average of three years of Net National Income values until year before last year and applying the corresponding annual average exchange rate for each year”

Here the Net National Income is defined as:

Figure 4.1: Net National Income for member countries over the three year period used in the average generating the 2015 budget for CERN Laboratories

Table 4.1: Country Contributions 2015 cite:cern-budget. The total budget for CERN in 2015 was 1127 Million Swiss Francs cite:total-budget. The USD/CHF exchange rate as of 01-01-2015 was 0.994 and 0.999 as of 12-31-2015 cite:xchange-rates. Countries contributing less than 5% are excluded from the list (Switzerland contributes 3.87%). The average contribution from the top 5 countries which comprise 68.8 of the operating budget is 0.068 million swiss franc per billion dollars USD of gross domestic product. For the United States a comparable contribution (1224 Million USD) would be larger than the 2015 operating budget

Country	GDP	Abs (Rel) Cont.	(Cont/GDP) $\times 10^{-6}$
Germany	\$3.36T	231M CHF (20.5%)	68 CHF/USD
France	\$2.24T	170M CHF (15.1%)	75 CHF/USD
UK	\$2.86T	161M CHF (14.3%)	56 CHF/USD
Italy	\$1.82T	125M CHF (11.1%)	69 CHF/USD
Spain	\$1.19T	88M CHF (7.82%)	74 CHF/USD
USA	\$18.03T	-	-

Table 4.2: CMS Gender Demographics by Age as of 2014. Age groups are separated by age range. Columns represented the fraction of the total CMS. 4119 Males and 863 females for an overall gender ratio of 4.77 men to every 1 female.

Age Range	% of Men	% of Women	Male/Female Ratio
< 25	12.6%	19.4%	3.1
25-29	20.0%	24.0%	4.0
30-34	12.8%	15.0%	4.2
35-39	9.7 %	8.4%	5.0
40-44	8.5%	8.3 %	4.9
45-49	8.3%	7.2 %	5.5
50-54	8.5%	7.0%	5.8
55-59	6.6%	5.0%	6.3
60-64	5.2%	2.6%	9.8
65-69	3.8%	2.1%	8.7
>69	4.1%	0.6%	34

Table 4.3: Differences in Absolute NNI vs GDP for the year 2015. Ordering remains fixed by absolute contribution size.

Country	GDP [USD]	NNI [USD]	NNI/GDP	NNI/Capita
Germany	3.36T	3.31T	0.99	40.6k
France	2.24T	2.27T	1.01	34.4k
UK	2.86T	2.33T	0.81	35.8k
Italy	1.82T	1.84T	1.01	30.3k
Spain	1.19T	1.33T	1.12	28.6k
USA	18.03T	15.67	0.87	48.7k

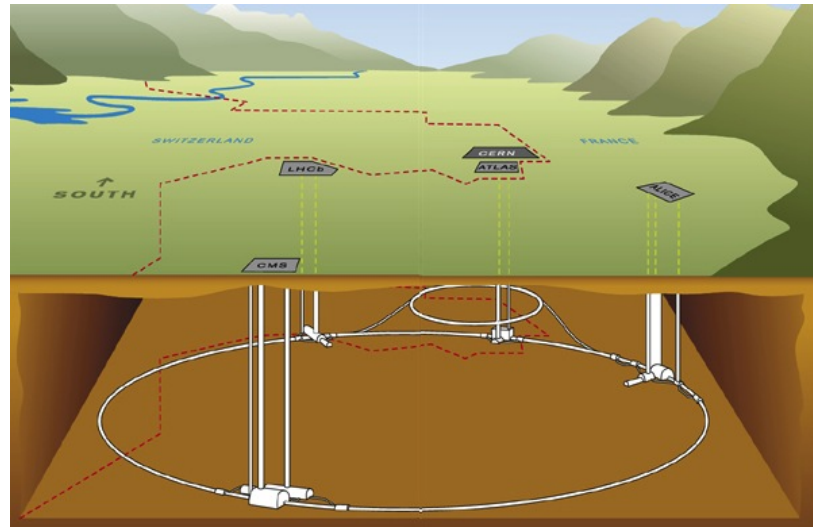


Figure 4.2: The LHC tunnel installed on the border of Geneva, Switzerland and France. The experiments are distributed along the circumference of the ring.

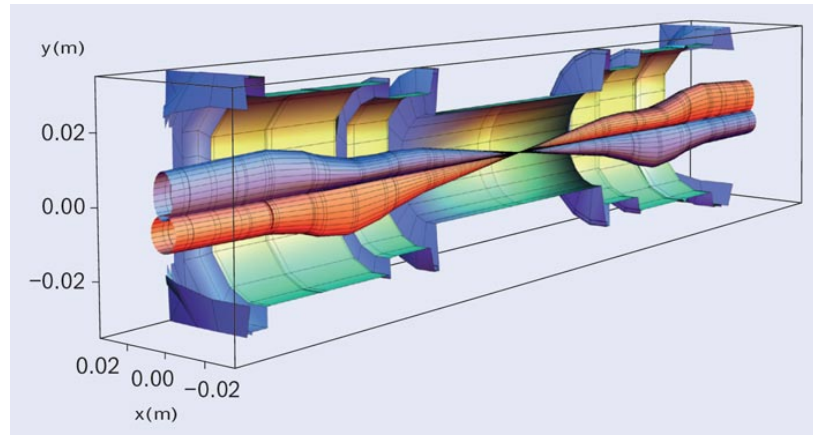


Figure 4.3: Squeeze

4.1.2 Organizational Structure

4.2 The Large Hadron Collider

The bunches of protons in the LHC are bent into a circular trajectory by more than 1200 superconducting dipole magnets and are focused and maintained close to the ideal orbit around the ring by hundreds of superconducting quadrupole magnets.

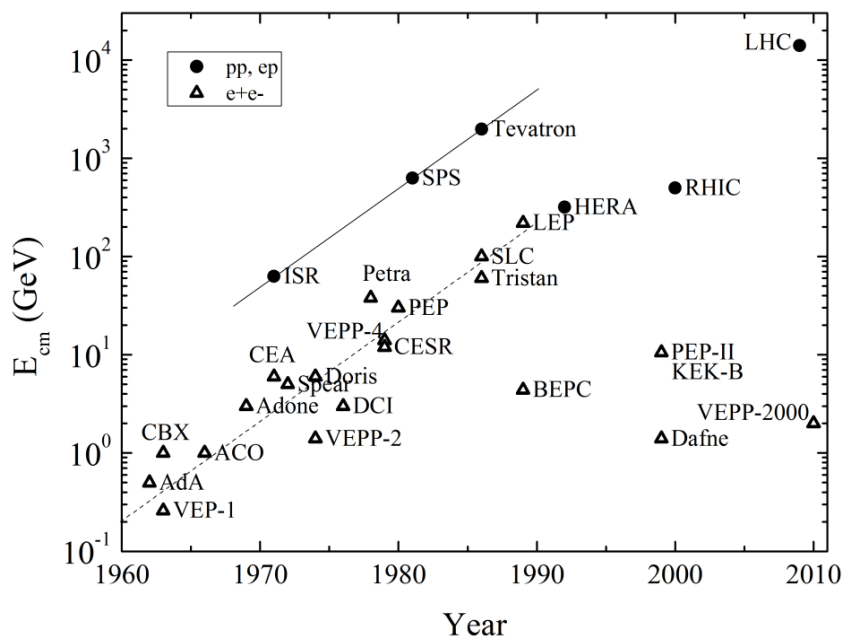


Figure 4.4: Historical Progression of collider energies

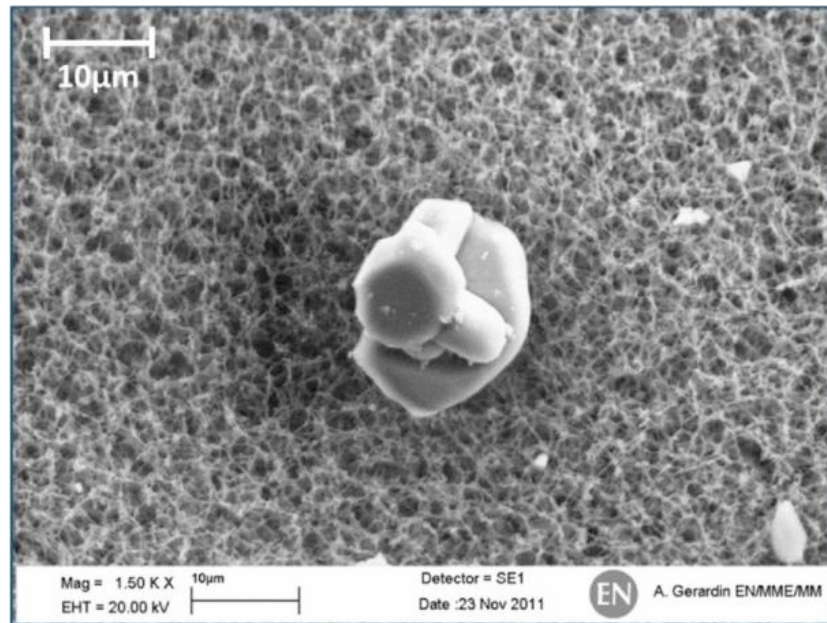


Figure 4.5: Unidentified Falling Objects (UFOs)

Table 4.4: LHC Running Parameters cite:LHC_PARAMETERS_ONLINE.pdf

Parameter	Value	Remarks
Circumference (km)	26.7 km	100-150 m underground
Number of Dipoles	1232	Nb-Ti Cables
Length of Dipole	13.3 m	
Dipole Field Strength	8.4 T	Results from high beam energy
Operating Temperature	1.9 K	He cooled superconducting magnets
Current in Dipole Coils	13kA	Results from high magnetic field
Beam Intensity	0.5 A	
Beam Stored Energy	362 MJ	1MJ melts 2kg Cu
Magnet Stored Energy / octant	1100 MJ	

Thousands of corrector magnets around the ring allow the beam to be steered closer to the ideal orbit, make the focusing independent of the particles' energy variations within a bunch, and cancel the effects of higher order multipoles in the fields induced by small field imperfections in the main magnets. The radiofrequency (RF) field in superconducting cavities is placed periodically around the ring and accelerates the protons from the injection energy of 450 GeV to the final operating energy, which is designed to be 7 TeV per beam. The RF field also causes the protons to be bunched, as only particles at or near a certain "equilibrium phase" on the RF wave will be accelerated stably. Special quadrupoles around each interaction region focus the bunches down to a small transverse size, to increase the likelihood of a proton-proton collision each time two bunches pass through each other.

Chapter 5

The Compact Muon Solenoid Experiment

Physics from a theoretical point of view can consider particles in terms of their kinematic phase space, however we cannot make direct measurements of the hard scattering process. Instead, detectors are built to indirectly measure the energy and momenta of the final state particles. To do this, a layered system of sub detectors is used to perform particle identification. By relying on known interactions of standard model particles with detector materials strong probabilistic statements can be made the flavor of particles in a given collision. By building a hermetic detector and integrating the various subdetectors in a given solid angle, one obtains a wholeistic view of the fundamental physics. This chapter will discuss each subdetector, the particles it is used to identify, and the underlying physics which allows the individual measurements to be made.

The Compact Muon Solenoid (CMS) Detector is a general-purpose detector consisting of an all silicon tracker, a precision electromagnetic calorimeter (ECAL), a hadron calorimeter (HCAL), a 4 T superconducting solenoid and muon chambers. The solenoid deflects charged particles whose paths are traced in the tracker, making

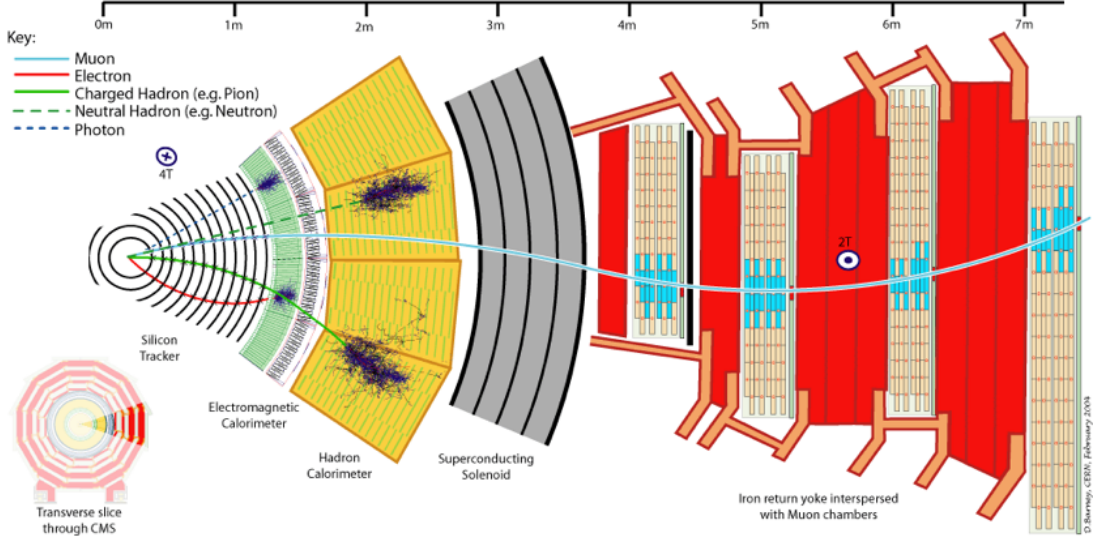


Figure 5.1: A tear-away view of the inner detectors of CMS.

it possible to reconstruct the particles' momentum. The two calorimeters reconstruct the energy of and identify photons, electrons and hadronic jets. As shown in Figure ?? the detector has cylindrical symmetry about the interaction point where the proton beams collide. By maintaining near full coverage of the interaction point it is possible to detect signatures such as neutrinos or other weakly interacting particles as missing energy.

5.1 Superconducting Solenoid

It is worth beginning this discussion with the central feature the rest of the detector is built, the design 4 T superconducting solenoidal magnet. For scale, a typical refrigerator magnet is on the order of 10^{-2} T and the MRI magnets can range between 0.5-3.0 T. The magnetic field is used to measure the momentum of charged particles by bending their trajectories. As the size of the bend is proportional to the field and inversely to the momentum of the particle, a stronger field is required to measure higher energy particles.

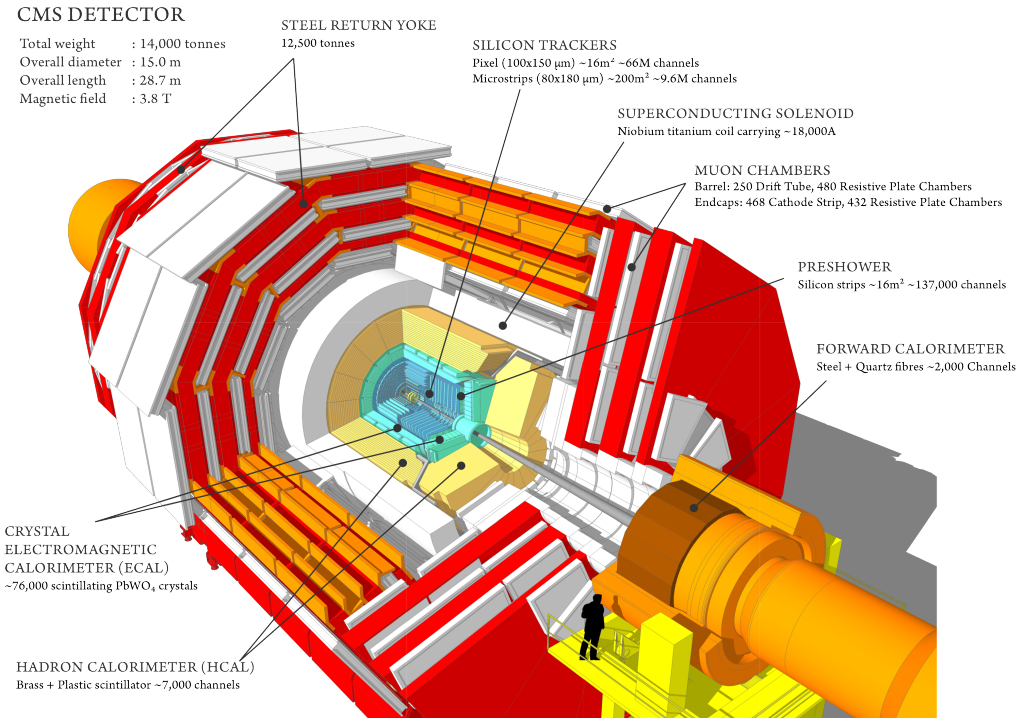


Figure 5.2: Cut away view of the CMS Detector

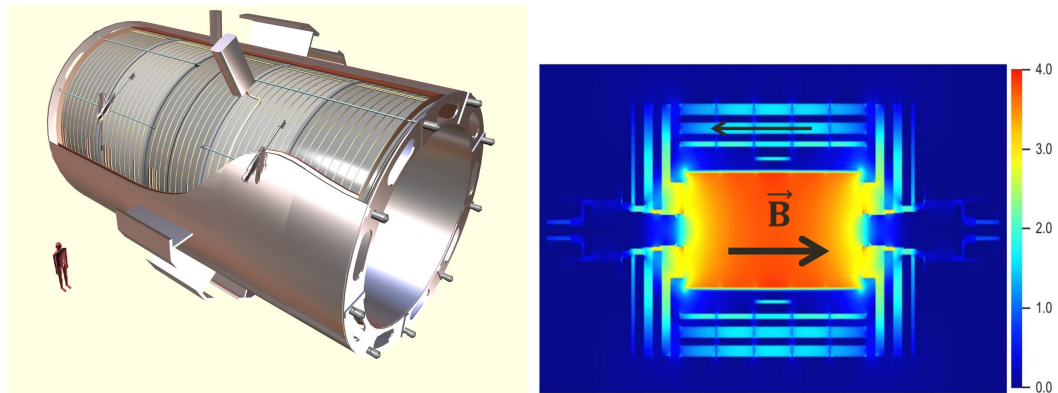


Figure 5.3: The CMS solenoid with a human for scale

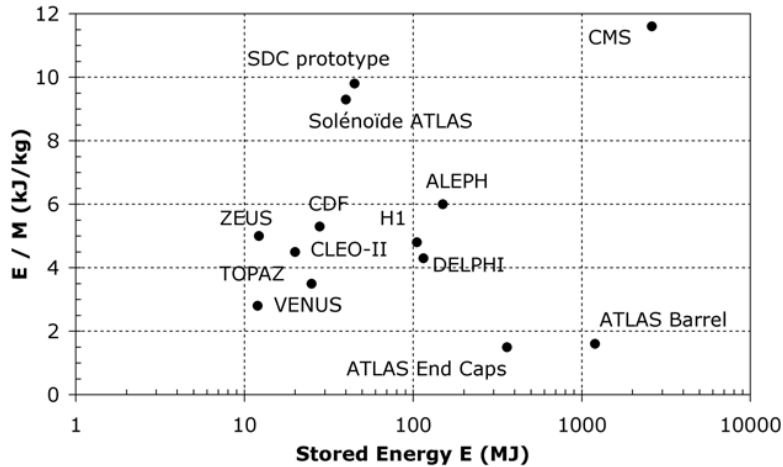


Figure 5.4: The CMS solenoid with a human for scale

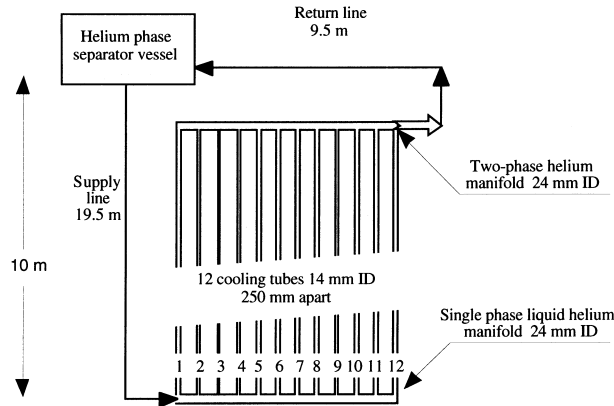


Figure 5.5: A sub circuit of the CMS thermosiphon

The magnet is 6 meters in diameter with 12.5 meters in length. The magnetic field is generated 2180 turns wound in four layers of Niobium Titanium conductors inside an alumnuminum cylinder carrying a nominal current of 20 kA. At the design field strength the solenoid a stores magnetic field of 2.66 GJ, the largest stored energy of any magnet ever built. The energy to mass ratio is 11.6 kJ/kG a indentifying feature in the historical context of detector magnets (Figure 5.5).

To operate in a superconducting state, the system is cooled 4.5 K with a thermosiphon (cite-quench-production). A thermosiphon is an indirct cooling method

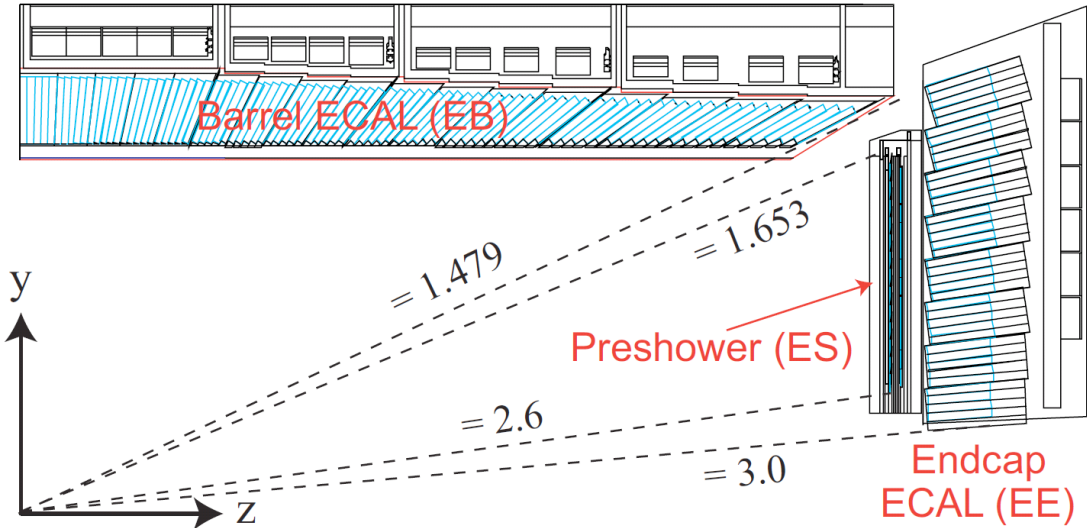


Figure 5.6: Kinematic coverage of the electromagnetic calorimeter (ECAL) barrel and endcap

utilizing passive heat exchange where rather than pumping the liquid helium the flow is induced thermally.

The system requires 3 days to reach cool the system from room to operating temperature.

The magnet is supplemented by a iron return yoke to

5.2 Electromagnetic Calorimeter (ECAL)

The electromagnetic calorimeter (ECAL) exists to measure the energy of electromagnetic showers of electrons and photons.

For high energy electromagnetic objects, that is above the mass threshold of pair production: $\gamma \rightarrow e^+e^-$, the interaction with matter occurs as an electromagnetic shower. In this shower, photons pair produce electron-positon pairs and electrons undergo bremmstrahlung radiation: $e^\pm \rightarrow \gamma e^\pm$. This processes continues until the individual particles in the shower cannot continue $1 \rightarrow 2$ processes and instead undergo multiplicity preserving interactions such as compton scattering and ionization.

The detector material (for CMS a scintillating crystal) is characterised the shower's Moliere Radius, defined as the radius (transverse to the incidence) of a cylinder that contains 90% of the shower. For the CMS ECAL, crystals are of approximately the Moliere radius 2.2 cm. The material can further be characterized by it's radiation length, the typical amount of matter the incident particle can traverse before an interaction. The CMS crystals have a relatively short radiation length of 0.9 cm. Each crystal is approximately 25 radiation lengths = 23 cm.

The crystal energy resolution as a function of energy is characterised as:

$$\frac{\sigma(E)}{E} = \frac{S}{\sqrt{E}} \oplus \frac{N}{E} \oplus C \quad (5.1)$$

Here σ is the gaussian standard deviation of the energy measurement, the operator \oplus signifies addition in quadrature, S the stochastic term, N the electronic readout noise, and C the constant term which does not scale with energy. The stochastic term S comes from the statistical nature of the photoelectric shower and the containment within the crystal. The readout term arises from the electronics noise in the preamplifier and digitization of the signal. The constant term C is caused by non uniformities between the many crystals and is ultimately dominated by the crystal to crystal intercalibration. As the first two term scale inversely with energy the constant term for high energy photons and electrons > 50 GeV is dominant. The design energy resolution for high energy photons like those found in the discovery of the Higgs boson is $< 0.5\%$

The ECAL consists of 75,848 Lead Tungstate PbWO₄ scintillating crystals Fig. ???. The ECAL is separated into two sections: the Endcaps and the Barrel. The Barrel consists of 61200 2x2x23 cm³ crystals separated into 36 Supermodules and is contained in $|\eta| < 1.48$. The Endcaps are separated into 4 Dees (Fig. 5.8) of 3662 crystals with each crystal measuring 3x3x22 cm. The 4 dees cover a pseudorapidity

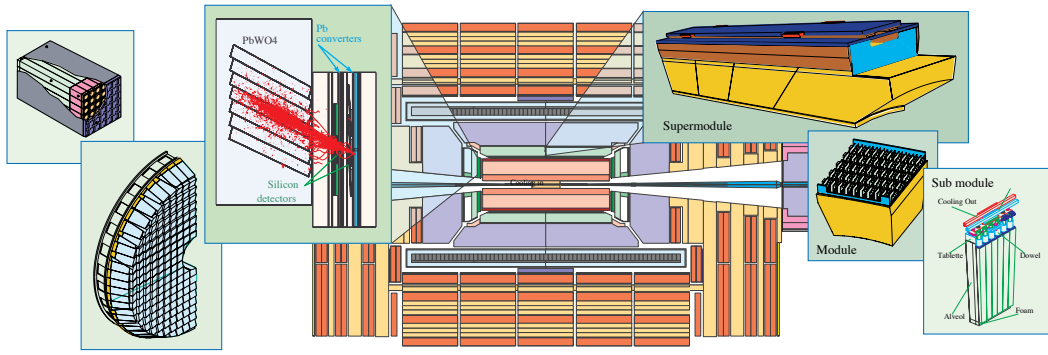


Figure 5.7: A single CMS ECAL Crystal (top left) tearaway view of distribution of crystals (top right) The construction of a single supermodule (bottom)



Figure 5.8: The ECAL barrel installed within CMS (left) A single Dee of the ECAL endcap (right)

range between $1.48 < |\eta| < 3.0$. The Endcaps are behind a preshower detector, composed of two lead absorbers interleaved with silicon detectors. The preshower covers the pseudorapidity range of $1.653 < |\eta| < 2.6$ with each silicon sensor covering a square area of 63 mm x 63 mm divided into 32 strips. The preshower is designed to give significantly better spatial resolution than using the endcap alone to aid in the separating single photons and $\pi^0 \rightarrow \gamma\gamma$ decays used to calibrate the endcap. As the first layer is 2 radiation wavelengths thick such that the majority of incident single photons will begin to shower before reaching the second layer.

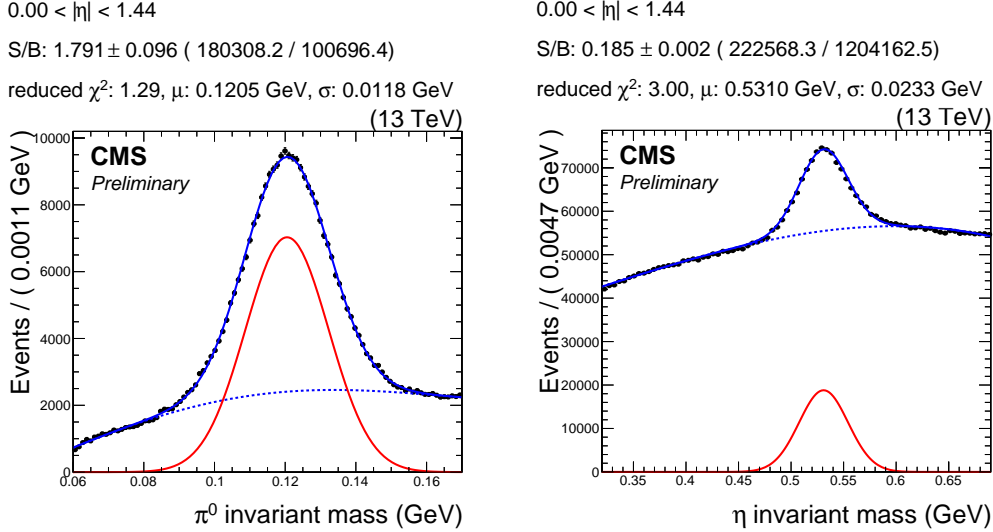


Figure 5.9: Calibration stream outputs for the pizero and eta barrel trigger paths

The preshower converts many of the photons, which assists in distinguishing directly produced photons from pairs of photons resulting from neutral pion decays.

The light in each crystal is collected as a current and amplified by avalanche photodiodes (APDs) in the barrel region and vacuum phototriodes (VPTs) in the endcap. This transition is necessary as the endcap region must be tolerant to much higher levels of radiation damage from softly scattered (low momentum transfer Q^2) interactions.

The detector is calibrated with a method that reconstructs the mass of neutral pion and eta-mesons to precisely calibrate the entire ECAL. The copious production of these particles in hadronic jets at the LHC allows us to perform this calibration rapidly, even at very low luminosity.

Under irradiation, the crystals undergo transpacency changes due to the formation of color centers, which interestingly recover spontaneously when there is no radiation present. As the crystal transparency affects the energy measurent, the crystal transparency is continuoulsy monitored by a laser monitoring system. The system takes advantage of a 3 μ s gap in the LHC bunch train to inject the pulses at a rate of 100

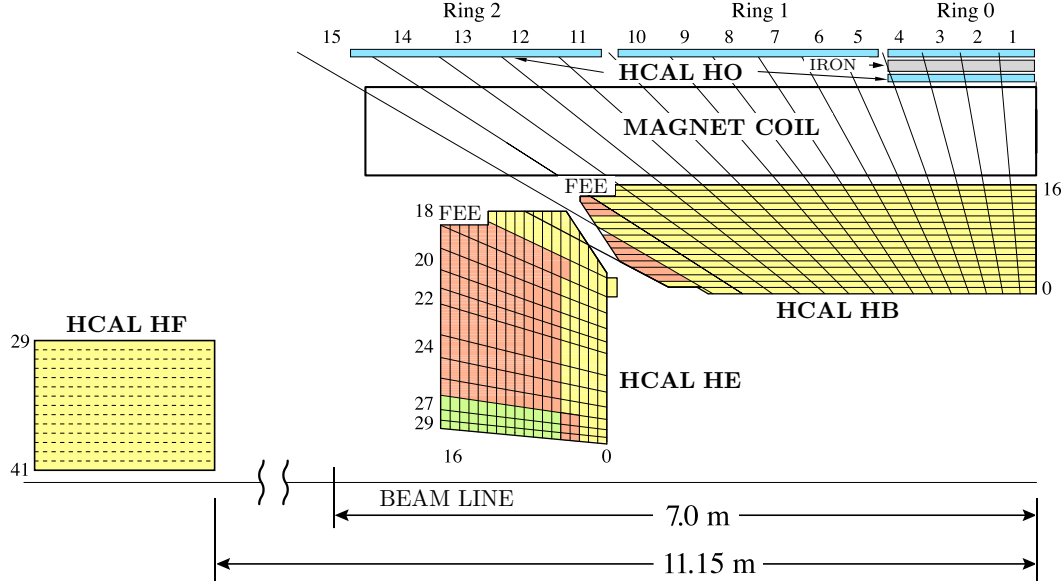


Figure 5.10: Kinematic acceptance of the CMS HCAL

Hz. This rate allows for a measurement of every crystal to be made at least every 30 minutes. In the barrel, only laser pulses of known wavelength are injected through optical fibers. In the endcap, LEDs provide an additional wavelength.

The presence of the preshower also causes some degradation of the Endcaps' energy resolution relative to the Barrel.

5.3 Hadronic Calorimeter (HCAL)

Surrounding the ECAL. The Hadronic Calorimeter (HCAL) is hermetic (full coverage of interaction), non-compensating (asymmetric electromagnetic and hadronic energy response), sampling calorimeter (showering material differs from measurement material) designed to measure the the energy of neutral hadrons which would not deposit significant energy in the ECAL.

The ratio of energy between the two detectors for defined solid angle, H/E , is a commonly used particle identification criterion.

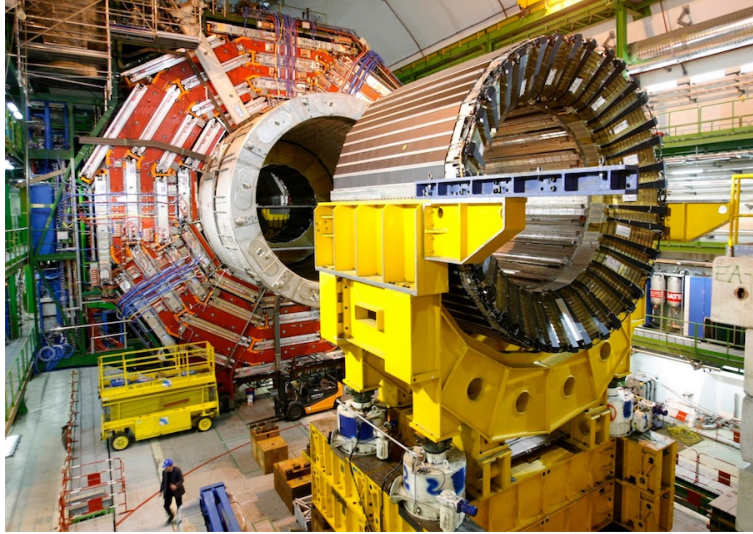


Figure 5.11: The CMS HCAL outside of the detector

The HCAL consists of 9072 channels divided between four sections: the barrel (HB), the endcap (HE), two forward calorimeters (HF) and an outer hadron calorimeter (HO). The barrel and endcap of the HCAL cover $|\eta| < 4$. The forward detectors extend the subdetector's reach to $|\eta| = 5$. As the HCAL is radially limited by the design of the enclosing solenoid, the HO is built around the solenoid to measure any leaked energy from high momentum showers. The towers are segmented into towers that project into η, ϕ space with $\Delta\eta \times \delta\phi = 0.087 \times 0.087$ for $|\eta| < 1.6$ and $\Delta\eta \times \delta\phi = 0.17 \times 0.17$ for $|\eta| > 1.6$.

The HF subdetector is a cherenkov light detector using quartz fibers within 165 cm of steel absorber. Photomultiplier tubes (PMTs) connected to the fibers convert the detected light to a detectable signal. Cherenkov detectors utilize the characteristic electromagnetic “sonic boom” created by particles traveling faster than light can travel in a material. As the angle of emission and intensity of the radiation depends on the velocity of the particle. For energetic particles $E > 1$ GeV the energy lost to the radiation is negligible (cite-the-physics-of-particle-detectors-book).

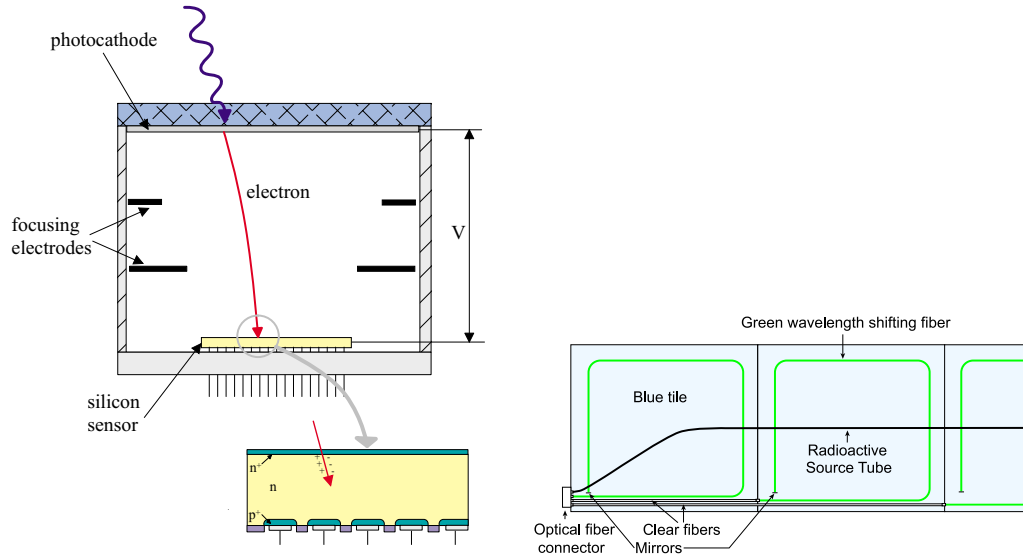


Figure 5.12: (Left) Diagram of a typical HPD under a potential difference V (cite-hpd-cern) (Right) 2 visible scintillator plates of 16 (cite-hcal-calib)

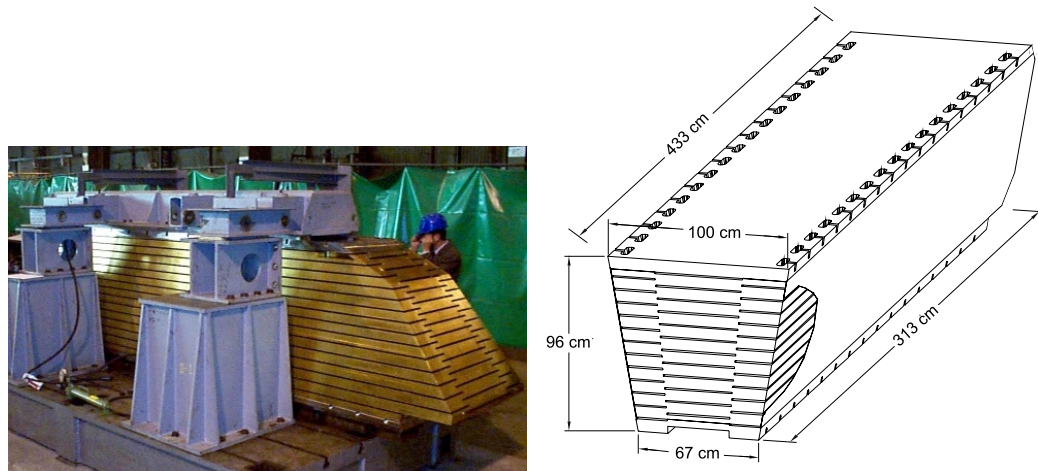


Figure 5.13: (Left) A single wedge of the CMS HCAL barrel (Right) Scintillator trays 5.12 are inserted into slots at the end of the wedge (cite-hbcalib)

Unlike electromagnetic showers, hadronic interaction cross sections are an order of magnitude smaller for the same material. To compensate cost effectively, hadronic calorimeters are constructed from dense materials such as copper, iron, lead, uranium, and tungsten (cite-tully). In general, hadronic showers produce irregularly shaped deposits and varied particle content when compared to electromagnetic showers.

The detector is constructed as alternating layers of brass absorber and plastic scintillator. The light is merged, wavelength shifted and measured by hybrid photodiodes (HPDs) with 17 channels per HPD. The HPD (Figure 5.12) functions by converting light into photoelectrons emitted at the photocathode and accelerated by a potential difference of 8-10 kV toward the silicon layer. The absorbed energy in the silicon sensor induces electron hole pairs which induce a detectable current. The light is wavelength shifted to avoid a loss in photons when piping light to the HPDs through a small cross sectional fiber. We are able to evade phase space conservation (photon flux per unit area) by redefining the phase space element in a lower energy wavelength spectrum.

Large deposits of energy reconstructed as purely hadronic energy in the HCAL is of particular interest to the study of long lived decays when the long-lived decay occurs inside of the HCAL calorimetetry. Although not studied here, large signal to background discrimination can be found by requiring a calorimeter deposit to have no associated tracks and a large ratio of hadronic energy H/E . It is also of concern that the HCAL is known to report have spurious noise that generally result in the mis-measurement of missing energy, but would mimics the signature of long lived decays. It is possible that using a coincidence of activity in the muon spectrometer could suppress these events.

5.4 Tracking Layers

The CMS tracker's purpose is to reconstruct the trajectories (or simply "tracks") of the charged particles copiously produced in hadron collisions. Using knowledge of the magnetic field along trajectory with position measurements taken from multiple layers of silicon strips and pixels, the helicoidal tracks are fit and kinematic parameters extracted.

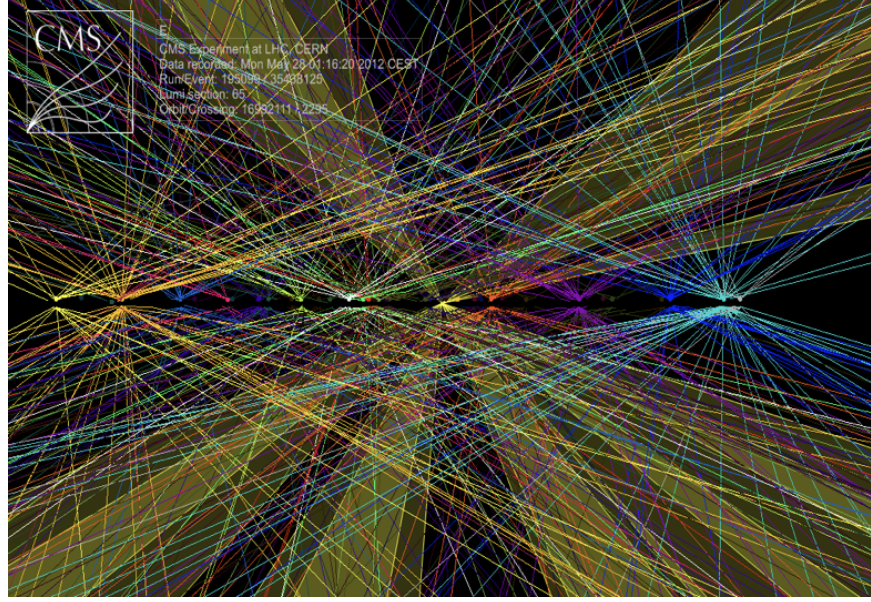


Figure 5.14: Pileup Interactions

A charged particle in a uniform magnetic field (like that of the CMS Solenoid) are parameterized by 5 parameters:

- d_ρ : the distance of closest approach to the reference point
- ϕ_0 : azimuthal angle specifying the reference point to the helix center
- p_t^* : charged signed transverse momentum
- d_z : signed distance of the helix from the reference point in the z direction
- $\tan \lambda$: the slope of the track

using these parameters, the trajectory is parameterized in the turning angle ϕ :

$$x = x_0 + d_\rho \cos \phi_0 + \alpha p_t^* (\cos \phi_0 - \cos(\phi_0 + \phi))$$

$$y = y_0 + d_\rho \sin \phi_0 + \alpha p_t^* (\sin \phi_0 - \sin(\phi_0 + \phi))$$

$$z = z_0 + d_z - \alpha p_t^* \tan \lambda \cdot \phi$$

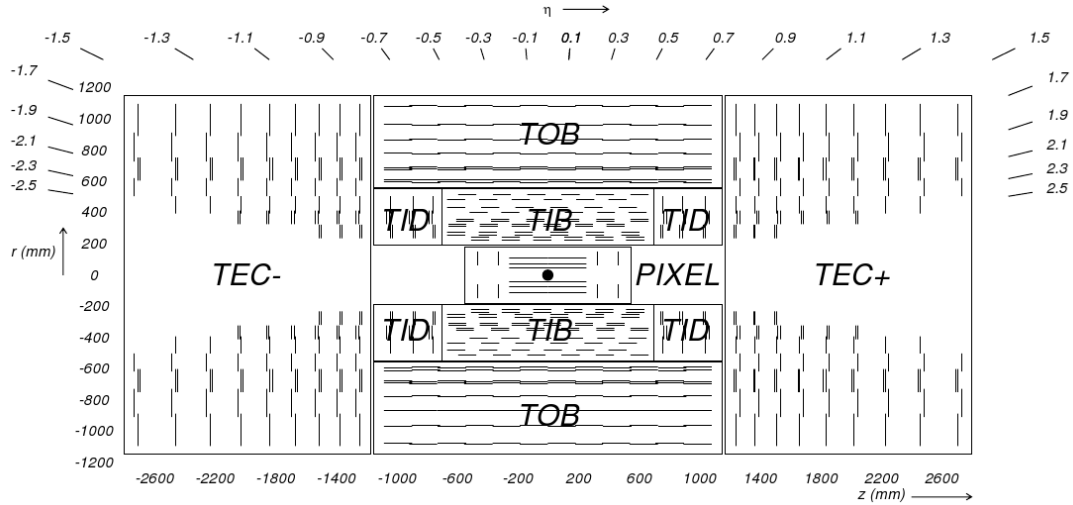


Figure 5.15: Kinematic acceptance of the CMS tracker

It is important to note that tracks do not necessarily have the same reference point. For CMS, each individual track parameter is computed against a reference point determined by the the closest point of approach to the beamline. For prompt physics, this reference point coincides with the collision vertex used to compute the kinematic parameters for calorimeter jets. In contrast, when tracks are displaced, the reference point used for the track is not the same as the reference point for the calorimeter jet *eta* and ϕ . This mis-match of coordinate systems affects the ultimate track and jet association.

By fitting trajectories to vertices the tracker enables the reconstruction of the hard interaction position (Figure 5.14). As only one vertex is typically of interest, identifying background vertices and subtracting their contribution is of increasing importance with the increasing instantaneous luminosity.

As photons and electrons exhibit nearly identical signatures in the ECAL, the reconstruction of the track associated to electrons is of particular interest.

The CMS tracker is the worlds largest all silicon detector with a sensitive area larger than 200 m^2 (Figure 5.17) (cite-2014-tracker-performance). The tracker consists of 10 layers in the barrel region: 4 inner barrel layers (TIB) and 6 outer barrel

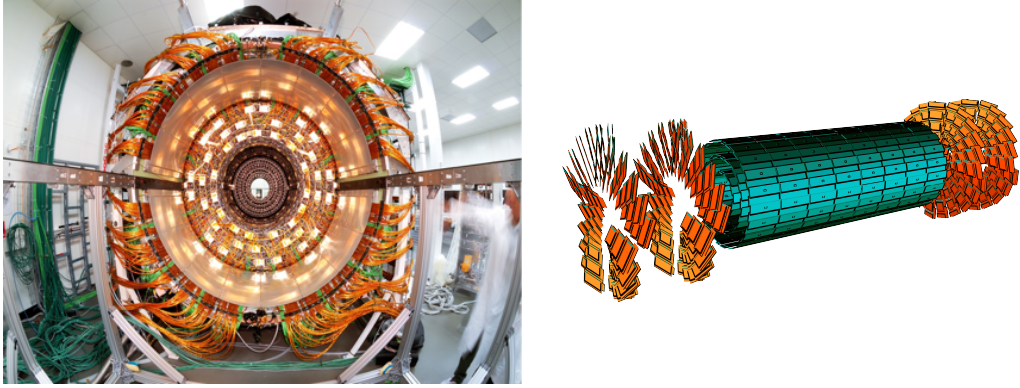


Figure 5.16: The CMS Pixel detector

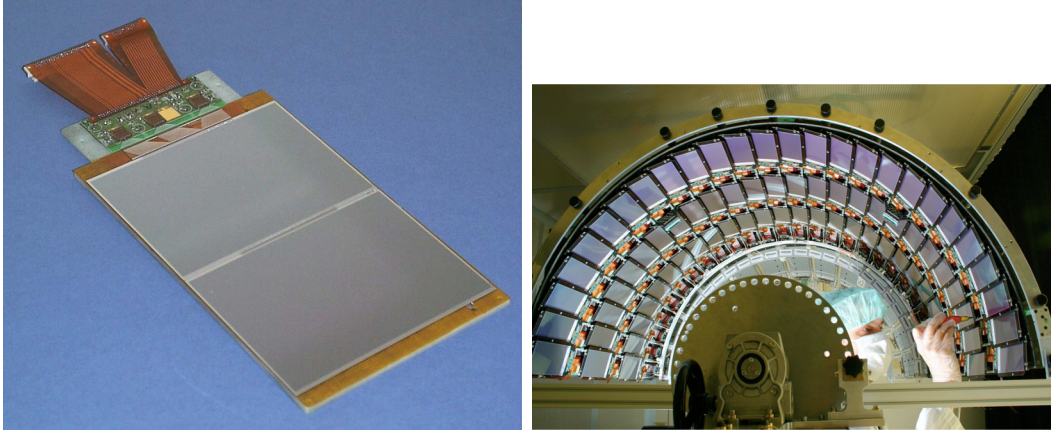


Figure 5.17: A single CMS tracker module (left) and a tracker inner barrel module (right)

layers (TOB). The endcap is made up of 12 disks: 3 inner disks (TID) and 9 endcap disks (TEC).

The CMS pixel detector (Figure 5.16) consists of three layers are radii of 5.3 cm, 7.2 cm and 11 cm and 2 disks on each size of the barrel at 34.6 and 46.6 cm from the either side of the interaction point.

Track reconstruction is degraded by the interaction with the tracker material. With some finite probability as a function of the material density and thickness, the track with randomly scatter.

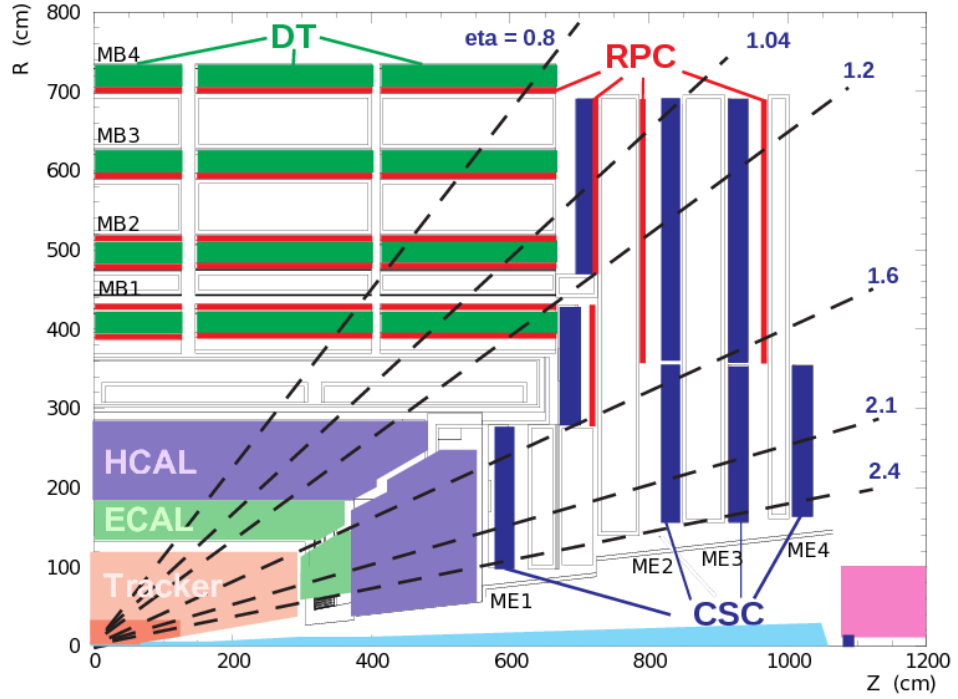


Figure 5.18: Kinematic acceptance of the CMS Muon System

High energy charged particles for which the detector volume and strength of the magnetic field do not permit the track to bend cause significant degradation of momentum resolution as well as charge sign determination. For low energy tracks, the magnetic field

5.5 Muon Spectrometer

The Compact Muon Solenoid's name is partly taken from the Muon subsystem which is built to identify and measure the trajectories of muons. The search for displaced jets uses only calorimeter quantities and inner tracking correspondingly no sensitivity to muons and no muon vetos. This section is included only for completeness.

The muon system consists of 3 separate detectors: drift tubes (DT's), resistive plate chambers (RPCs), and cathode strip chambers (CSCs). All three systems rely on the ionization of a gas medium caused by the charged muon's traversal through

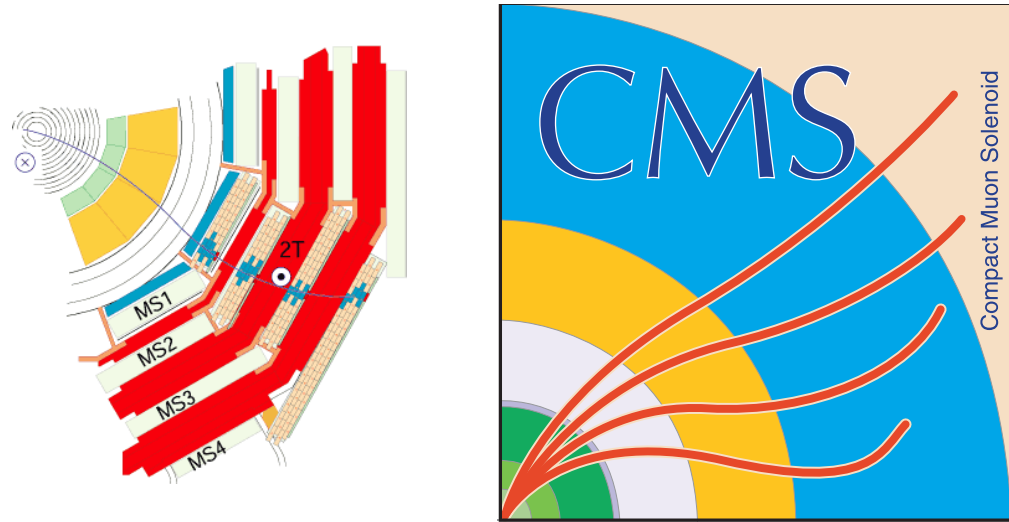


Figure 5.19: Slice of the muon detector (left) and cms logo (right)

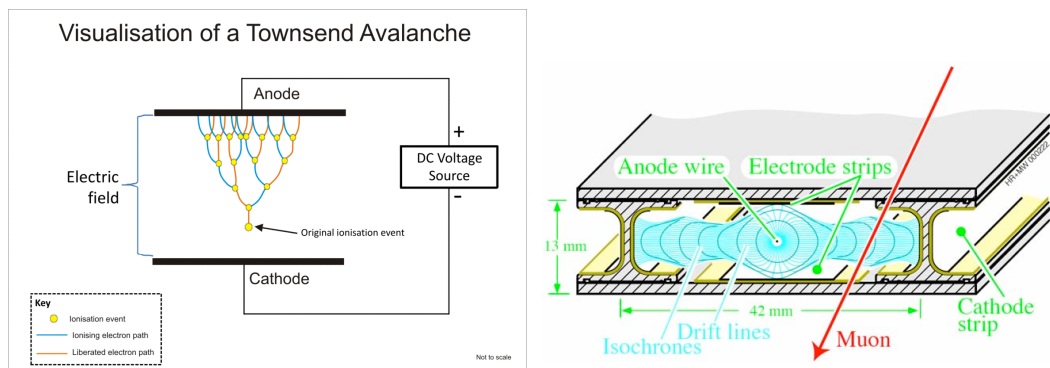


Figure 5.20: When a gaseous medium is ionized by the track of a muon the resulting liberated electrons are accelerated in the electric field and collide with gas molecules. The result is an avalanche of electrons collected at the anode. The process is known as a Townsend Avalanche (left). The drift tube design showing the drift lines.

the detector. The detectors are multi-layered and sandwiched between layers of the iron return yoke (Figure 5.18). The iron layers aid in particle identification by stopping nearly all other particle activity before the final detector layer. As muons are very weakly interacting, they should be the only particles reaching the edge of the detector. When the magnetic field changes outside of the solenoid, muon tracks will change curvature in the muon system as depicted in the CMS logo (Figure 5.19). The second measurement made in the muon spectrometer improves the momentum resolution for energetic muons $> 100\text{GeV}$, however lower momentum muons are dominated by a increase of multiple scattering from the additional detector material.

In the context of long-lived searches it is interesting that the muon is the only long-lived fundamental particle, with a finite lifetime of $\tau_0 = 2.2\mu\text{s}$ or equivalently $c\tau_0 = 660\text{m}$. The dominant decay to an electron and two neutrinos is suppressed by requiring the muon decay with an offshell decay through the much heavier W . This method of generating long-lived signatures mirrors the motivations of split supersymmetry where the gluinos are long-lived as they must decay through much heavier squarks. If this were the end of the story we would expect $\approx 1\%$ of muon decays to occur before the final layer. However, a moderately energetic muon will experience time dilation $c\gamma\tau_0$ in the lab frame with $\gamma = E/m = (1 \text{ GeV})/105 \text{ MeV} \approx 10$. Accordingly, on detector length scales $O(10 \text{ m})$ energetic muons can be considered stable.

The drift tube system located in the barrel region covers $|\eta| < 1.2$ with 4 concentric rings (segmented in $r = 4.0, 4.9, 5.9, 7.0 \text{ m}$) referred to as “stations”. Five divisions are also made in the z direction referred to as “wheels” partitioned into 12 sectors of 30 degrees. The three inner cylinders have 60 chambers each and the outer cylinder has 70. Each chamber measures $3.0\text{m} \times 2.5\text{m}$. Each chamber is divided into 3 (or 2) super layers with 4 drift cells per layer (2 in ϕ , 2 in z). The drift cells use anode wires at voltage of $+3.6 \text{ kV}$, electrode strips at 1.8kV and -1.2kV cathode strips to detect the

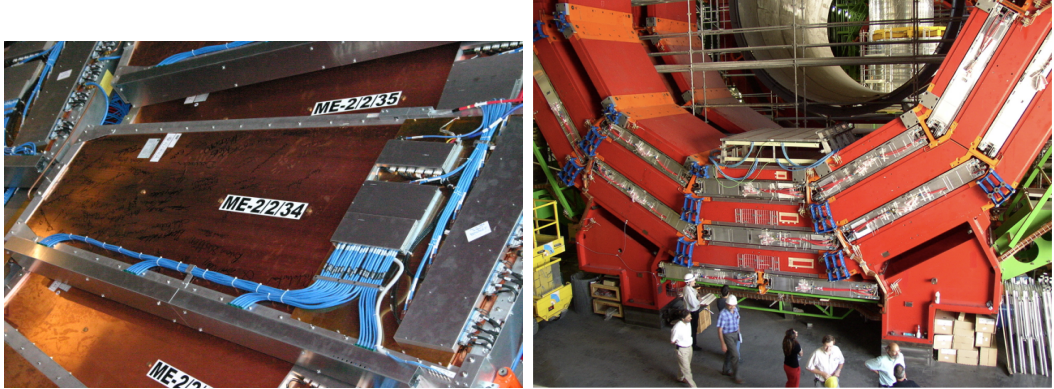


Figure 5.21: The Muon Cathode Strip Chamber

localized ionization showers from muon tracks (Figure ??). The full system includes 172,000 wires. The maximal path of drift is 21 mm corresponding to a drift time of 380ns in a gas mixture of 85% Argon and 15 % CO₂. (cite-complete-cms-description)

The CSCs and DTs are located in the endcap region. The CSCs are located between $0.9 < |\eta| < 2.4$ and the RPCs between $0.9 < |\eta| < 1.6$. There are 4 stations for each endcap. The CSCs are trapezoidal multiwire proportional chambers comprised of 6 wire planes interleaved with 7 cathode panels. The chambers extend 1.7 (or 3.4) m in the radial direction covering 10 or 20 degrees. Each chamber layer Wires running in the ϕ direction define a tracks radial position. The ϕ coordinate along the wires is obtained by interpolating charges induced on the cathode strips.

5.6 Trigger System

The CMS Trigger System exists as a filter through which events are determined to be interesting or useful enough to be written down. The name comes from the nature of algorithms used to determine what to write down. If an event passes any of the online algorithms, this “triggers” the collision to be written down in its entirety regardless of the goals of the path in particular (albeit with some notable exceptions). It is both unnecessary and impractical to record every collision the LHC delivers. The

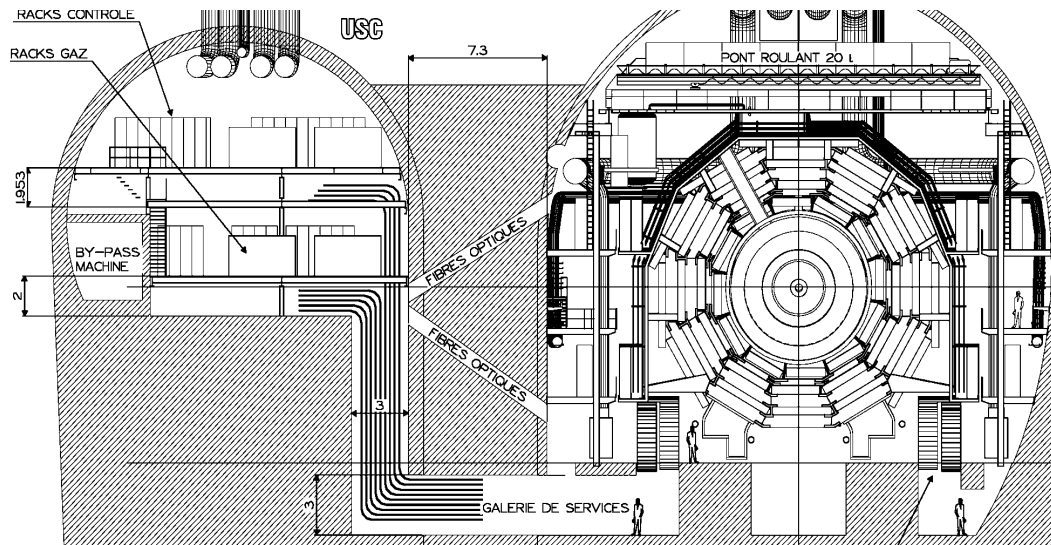


Figure 5.22: Location of the counting room relative to the experimental hall

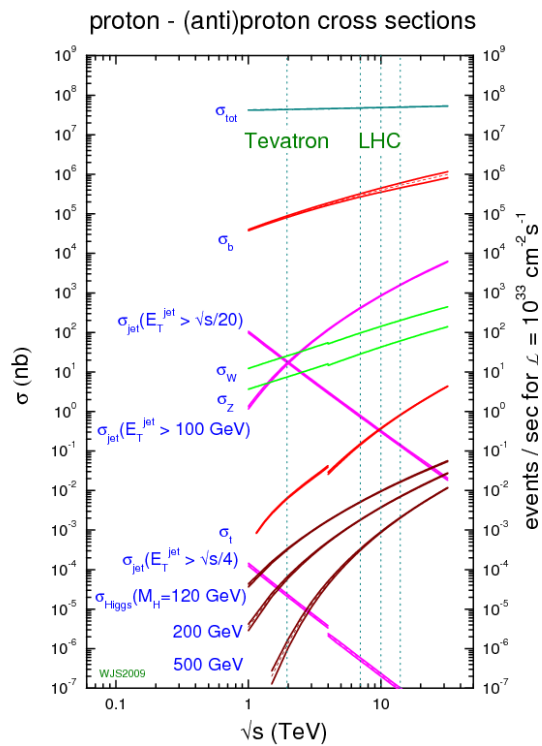


Figure 5.23: Common cross sections of proton collisions as a function of the center of mass energy \sqrt{s}

low momentum transfer hadronic events contained in the vast majority of proton collisions is well understood from past experiments. Figure ?? shows typical physics processes for proton-proton scattering. Events such as the production of a b quark occur at $\approx 10^6$ Hz at a luminosity of $\mathcal{L} = 10^{33}$ cm $^{-2}$ whereas processes of interest, such as the production of the Higgs is much lower at $\approx 10^{-2}$ Hz.

The LHC has beam crossings at a rate of ≈ 40 MHz with each crossing coming spaced at ≈ 25 ns. The number of inelastic collisions per bunch cross crossing is given by the total inelastic cross section times the luminosity divided by the bunch collision rate. This is respectively $8.5 \times 10^{-26} \text{cm}^2 \times 10^{34} \text{cm}^{-2}\text{s}^{-1} / (40 \times 10^6 \text{s}^{-1}) \approx 24$ (cite:arXiv:1204.5689). The collisions are stored with an average file size 1 MB in their unprocessed form in a format referred to as **RAW**. However the bandwidth for the combined constraints of acquisition rate, storage and processing, is limited to 10^3 Hz and equivalently 10^3 MB/s. Generally, all but one of the inelastic collisions is interesting and a large excess of activity is generated in the detector electronics. The trigger must be robust enough to select these events efficiently while remaining efficient in maximizing the limited bandwidth.

The CMS Trigger system is designed to read events at the event crossing frequency and generate the factor 10^5 of rejection between the crossing frequency and the archival capacity. This factor is too large to achieve in a single step given the complexity of triggers and event reconstruction necessary to build efficient algorithms. Therefore the task is split into two steps The Level 1 (L1) and High Level (HLT) Trigger systems (Figure 5.24). The L1 system is a coarse study of an event designed to be fast and capable of analyzing every event at 40 MHz. The HLT provides the flexibility the L1 lacks permitting as much event reconstruction

The most obvious criterion for interesting events are hard physics events with high momentum transfer, q^2 , and correspondingly large transverse momentum. As the protons collide with effectively no transverse momentum, any event with significant

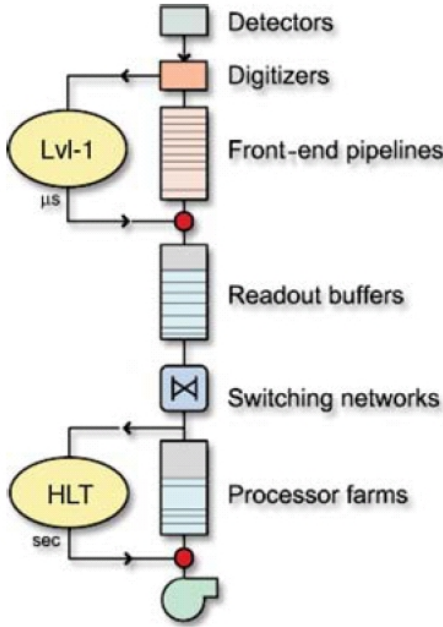


Figure 5.24: A diagrammatic representation of the level 1 and HLT trigger processing (cite-tridas-tdr)

deposits of transverse energy (or even missing transverse momentum) is indicative of a hard physics process. The total transverse energy of an event falls off exponentially, so a simple way to reduce the rate of processed events is to raise the energy requirements of accepted events. However, given the increasing luminosity of the LHC the thresholds are encroaching upon Standard Model physics processes like single W production where triggering on every single-electron event is a reaching kinematically limited regime.

The particulars of a given high level trigger path is dictated by their use case. Generally, analyses searching for new physics are categorized by their final state signature. Correspondingly, the trigger requires loose identification on the objects of that signature such as the isolation and shape of energy deposition. Additional, global requirements such as angular separation, or the invariant mass of two objects is common as well. Once the event has passed the Level 1 and HLT Triggers, tighter and

more computationally costly selection can be made offline where we are unrestricted by bandwidth limitations.

5.6.1 Level 1 (L1) Trigger

The L1 Trigger is built using custom hardware composed of field programmable gate arrays (FPGAs), application-specific integrated circuits (ASICs) and programmable look up tables (LUTs).

The Trigger Primitive Generators (TPGs) are locally constructed from the energy deposits in the calorimeters or hits/track-segments in the muon chambers. The regional reconstruction applies coarse pattern recognition to the primitives and combines them. Together the Global Calorimeter Trigger (GCT) and Global Muon Trigger (GMT) are processed at the global trigger (GT) to decide whether or not an event is kept. It is important to note that there is no inner tracking performed at this level (only muon specific tracking). Track building is time intensive and cannot, in its current state, be performed reliably at speeds comparable to the bunch crossing frequency. Future upgrades are planned to include tracking at the L1 which would significantly aide in the detection of soft hadronic signatures with specific track topologies (ex. displaced signatures and VBF SM Higgs Production in decays to $b\bar{b}$).

The jet trigger primitives are built from transverse regions of 12 x 12 grids constructed from

The regional calorimeter trigger (RCT) collects regional transverse energy sums segmented in variable size trigger tower arrays summed between the ECAL and transversely adjacent HCAL within $|\eta| < 5.0$. Electrons and photons use the same size

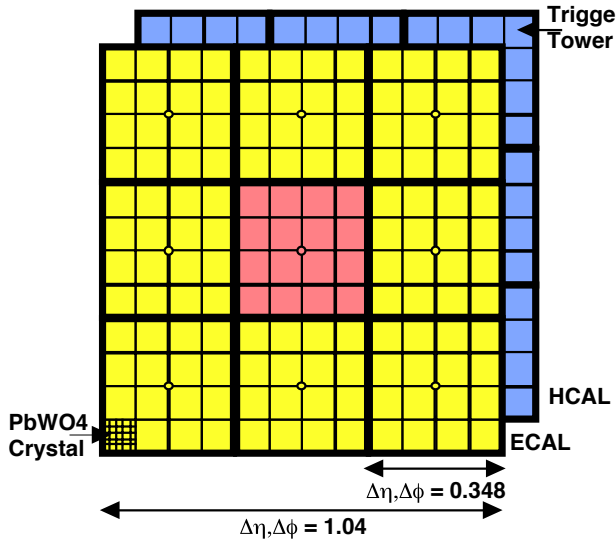


Figure 5.25: A representation of a jet as assembled from the ECAL and HCAL trigger primitives. (cite-tridas-tdr)

Table 5.1: High Level Trigger filter farm configuration in 2015 (cite-clint-timing)

Install Year:	2011	2012	2015
CPU	X5650	E6-2670	E6-2680v3
Architecture	Westmere	Sandy Bridge	Haswell
CPUs per board	2	2	2
Cores/CPU	6	8	12
RAM	24 GB	32 GB	64 GB
Clock Rate (w/Boost)	2.66 (3.06) GHz	2.60 (3.30) GHz	2.50 (3.30) GHz
Total Cores (Boards)	3456 (288)	4096 (256)	8640 (360)

5.6.2 High Level Trigger (HLT)

Algorithms at trigger stage are referred to as paths. The entire collection of paths is referred to as a trigger menu. As the physics goals of the experiment change and machine luminosity ramps, the menu must evolve and adjust the thresholds within a given menu. The HLT is a crucial component of CMS data taking, as new physics that is never written down is never discovered. Problems with the offline reconstruction can be fixed at a later date by reprocessing the RAW data, but problems with the

online reconstruction as performed by the trigger paths) is permanent in the data collected.

The paths are configured as a series of re-usable modules that either build an object (producers) or terminate the execution of the path based on some quantity (filters). The paradigm ensures, that a producer which creates, say, the sum of transverse energy in the detector, is processed exactly once, despite being used by multiple paths. Ensuring that modules are reusable and reused greatly minimizes timing overhead of additional paths. Common sequences, such as unpacking the calorimeter energy, are utilized by nearly every trigger. CMS as an experiment excels from a monolithic approach to its software where, the same software (known as CMSSW) is for analysis and data processing is used online.

The development, debugging, and testing of these menus is a large organizational effort that requires the input from nearly every level of the experiment. Physics Object Groups (POGs) e/gamma, Muons, Jets, and B physics must build the online recommendations for object identification and ensure their performance with the varied paths which use them. Physics Groups (Higgs, Exotica, SUSY, etc.) must develop paths and justify the added physics value of the individual paths in terms of their sensitivity. The Detector Performance Groups (DPGs) must provide object energy calibrations for the online energy reconstruction which differs significantly from the offline reconstruction.

Additionally, the DPGs must implement separate data streams, which save a much smaller event content, to calibrate the detector. For instance a separate data stream exists for collecting the copious production of π^0 and η^0 mesons which predominantly decay to two photons. The stream performs only the reconstruction of the ECAL and searches for low p_t clusters within an invariant mass window. Saving only the hits corresponding to these clusters reduces the event size from 1 MB to 2kB allowing the

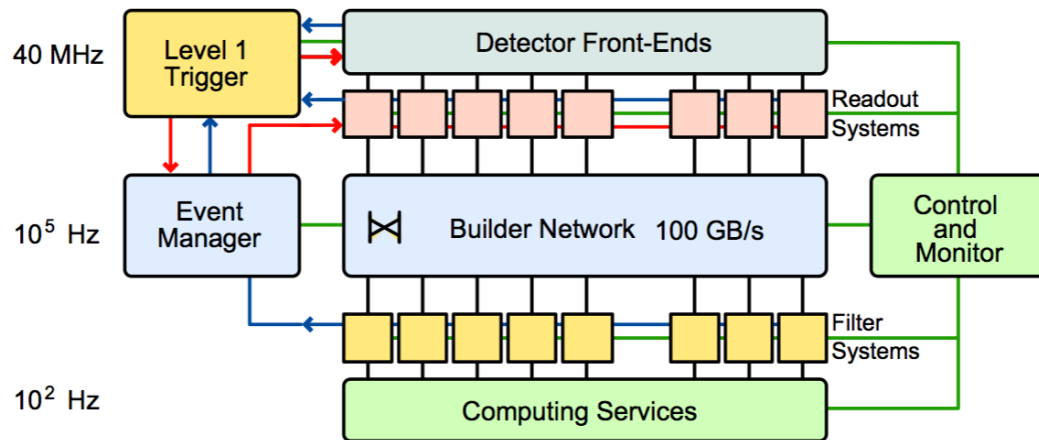


Figure 5.26: A diagrammatic representation of the level 1 and HLT trigger processing

stream to acquire events at a rate of 7kHz while maintaining a small bandwidth. For comparison, the physics data stream writes at 1000 Hz.

The CMS HLT System is built from a varied collection of commercially available CPUs comprising more than 16,000 cores in 2015 (Table 5.26).

5.6.3 DAQ

Chapter 6

Studies of Displaced Jet Tagging Variables

6.1 Introduction

The identification of jets originating from b quarks (b -tagging) was originally developed and successfully utilized for the discovery of the top quark. Among other applications, b -tagging is now a tool for studying the Higgs and searching for beyond the standard model (BSM) physics. Since its inception, b -tagging has evolved including the implementation of particle flow, refined secondary vertex algorithms, and advanced multivariate techniques. The strength of b -tagging is not restricted to its signal to background differentiation, but includes the community sized impact of a well defined and supported physics object definition.

The b -tagging algorithms are publicly documented with corresponding working points and data/mc factors derived by the physics object group (POG in CMS). The algorithms are integrated directly into the experiment software allowing fast adoption of subsequent improvements. The object can then be used interchangeably as part of a large toolkit of jets, leptons, taus, photons, and missing energy.

Past searches (list references here) by CMS and ATLAS experiment for long lived particles decaying to jets rely significantly on secondary vertexing of displaced tracks. As the ability to vertex the jet is highly dependent on the ability to reconstruct highly displaced tracks, the existence of a vertex, although the highly separating between signal and background is often the most inefficient selection criteria (especially at long life times on the scale of the detector). Of particular concern is that current vertexing algorithms may not perform effectively for non-SM jet vertices such as found in Emerging Jets [citation].

The case of long lived particle that decay outside of the detector remains outside the scope of jet-tagging, but remains an interesting use case in conjunction with the tag definitions.

Analyses utilizing the tags should expect strong topological sensitivity for ≥ 2 displaced jets, electrons, and taus regardless of their configuration of a long lived X decay. Lifetime sensitivity is expected for decays which occur for transverse distances between 1mm to 2m, corresponding to outside of the lifetime of b hadrons up to the edge of the HCAL.

6.1.1 Significant differences with respect to b-tagging

Given the close analogy to b -tagging techniques, it is important to clarify where b -tagging algorithms are inefficient and where they can be extended.

For shorter lifetime regimes ($c\tau < 1$ mm), b -tagging can still identify displaced jets, but leaves room for new techniques. Heavy long-lived resonances undergoing a 2 body decay will have significantly more momentum transverse to the flight direction of the long lived particle (when compared to a b decay). This angle is a powerful discriminant to background nuclear interactions and is strongly correlated with the boost of the mother particle. Under the assumption that the angle is small, b -tagging uses only positively signed impact parameters for track identification (corresponding

to to decays downstream of the flight path). Heavy particles produced nearly at rest will decay isotropically with impact parameters of negative sign (when decays occur backward relative to the mother's momentum direction).

For longer lifetimes, a transition occurs at distances larger than a few centimeters where new issues undaddressed by b-tagging arise. Although the b meson is displaced it is comparably straightforward to discern the primary vertex of the event. This allows b-tagging algorithms to more accurately calculate longitudinal quantities, such as 3D track impact parameters. For displaced jets, this is not the case and utilizing longitudinal quantities relative to a mis-identified primary vertex can yield sub-optimal performance. Pixel hit requirements are explicitly required for tracks used in b -tag secondary vertexing, but displaced jets decays can occur outside the pixel layers. In addition, b-tagging algorithms include upper bounds on longitudinal and transverse impact parameters to limit contributions from nuclear interactions.

o

6.2 Samples

6.3 Signal Samples

Two signal samples are used to study displaced identification which we will refer to as $XX4J$ and GUN . Both samples are generated using PYTHIA 8 (cite-pythia).

The $XX4J$ sample consists of the direct pair production of two neutral X^0 's with finite lifetime. Each X^0 decays to u,d,s,c, and b with equal probability. This sample is generated with flat pileup between 10 and 50 with 25 ns bunch crossing code for cmsDriver as `Flat_10_50_25ns`. It is important to note that due to pile up interactions, these samples contain both prompt and displaced jets. In this sample,

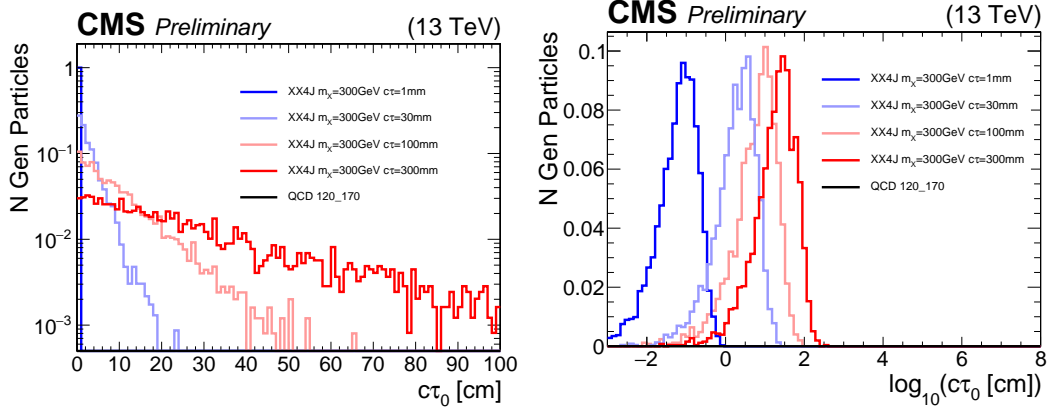


Figure 6.1: The proper $c\tau_0$ of the XX4J samples. The samples are generated with exponential lifetime distributions $e^{-x/c\tau_0}$ which have mean $c\tau_0$ and exponential slope $1/c\tau_0$.

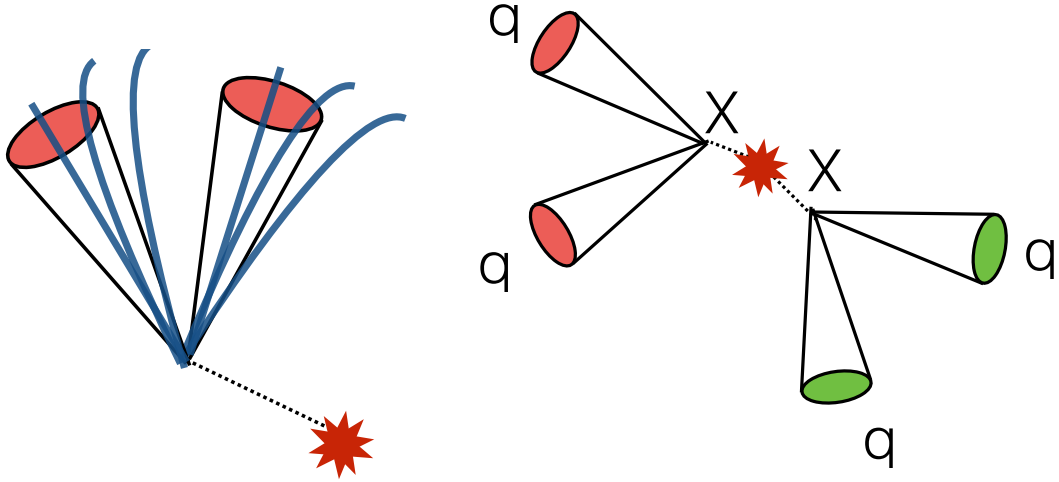


Figure 6.2: The topology of the two samples used in the study *GUN* (left) and *XX4J* (right)

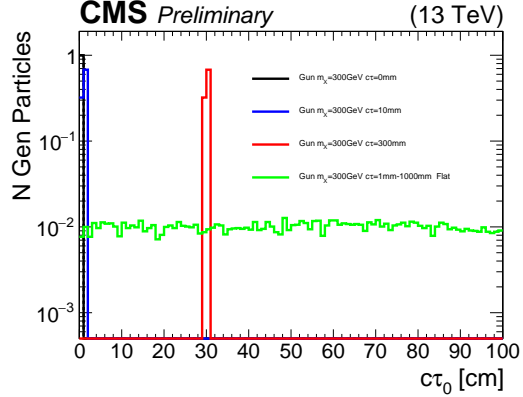


Figure 6.3: The proper $c\tau_0$ of the displaced di-jet gun samples. The samples are generated with either flat, or delta function $\delta(c\tau_0 - c\tau'_0)$ lifetime distributions

variables for displaced jet identification generally have two distinct populations of jets.

The $XX4J$ samples are generated with varied lifetimes and masses (Fig. 6.1). Each X^0 has an exponential lifetime distribution $e^{-x/c\tau_0}$ with mean $c\tau_0$ and slope $1/c\tau_0$.

The second sample is a displaced di-jet gun sample denoted *GUN*. This sample is generated using the `PythiaPtGun` interface. A single X^0 particle is generated with flat $50 < p_t < 500$ GeV, flat ϕ , and flat $-2.4 < \eta < 2.4$. The X^0 decays to a pair of d quarks with 100% branching fraction. Each event will thus contain a single displaced vertex. The configuration for the gun parameters is shown below. Small modifications to CMSSW are required to create a Pythia rather than HEPMC Particle with a finite lifetime.

The resonance is decayed within pythia and passed directly to hadronization bypassing all process level pythia effects: initial state radiation, final state radiation, and beam remnants. Furthermore, the event is reconstructed without pileup mixing. This sample is generated to have a sample of reconstructed tracks that only originate from a displaced vertex without the complications of correctly. One important side effect of simulating without pileup is the lack of a reconstructed primary vertex.

The proper lifetime distribution of the sample is chosen to be either a delta function $\delta(c\tau_0 - c\tau'_0)$ or flat between 1mm and 1000mm (Fig. 6.3). Additionally two prompt dijet gun samples are built for comparison. One sample with lifetime 0mm decaying to two b-quarks and one sample with lifetime 0mm decaying to two d-quarks. A reminder that the decay length in the lab frame will differ by a factor $\gamma\beta$ from the proper lifetime .

The reconstructed calo jet transverse momentum for varied lifetimes is not especially sensitive to the lifetime of the decaying X^0 (Fig. ??) until very long lifetimes. The flat lifetime gun sample develops high transverse momentum (relative to the shorter lifetime) jets when the long lived X^0 decays at a transverse distance far enough from the beamline to be reconstructed as a single jet, or decaying entirely inside the calorimeter.

6.4 Individual Variable Studies

6.4.1 Impact Parameter Information

The tracks originating from a decay at a displaced vertex will have large impact parameters relative to the true primary vertex. The impact parameter is calculated by starting from the particle trajectory at the innermost measurement point and extrapolating backward to the minimum distance between the track and jet direction \vec{j} (Fig 6.5). Here, the track is linearized by taking the line tangent to the track at this point. The minimum distance from this linearized track to the primary vertex gives the magnitude of the impact parameter. We will refer to the vector pointing from the primary vertex to the point of minimum distance as \vec{IP} (Fig. 6.4).

The sign of the impact parameter is given as the sign of the scalar product between \vec{IP} and the direction of the jet: $\vec{IP} \cdot \vec{j}$. For decays where the calo jet direction is accurately reconstructed, the impact parameter of displaced tracks will have positive

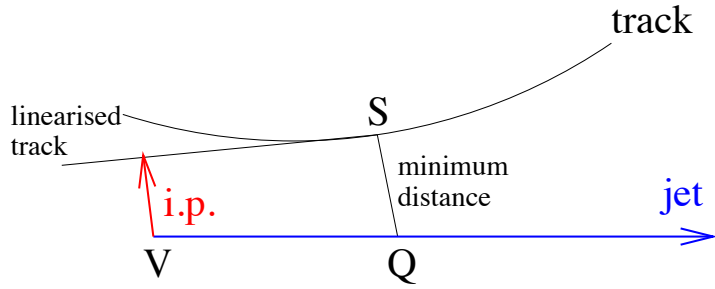


Figure 6.4: Diagram depicting the impact parameter calculation. V is the position of the primary vertex. $\vec{j} = \vec{V}\vec{Q}$ is the direction of the calo jet. S is the point on the track extrapolation backward from the inner hit which is closest to the jet axis. From S the track is linearized and extrapolated backwards. The impact parameter magnitude is the minimal distance on the linearized track from the primary vertex. We will denote the vector from the primary vertex to the point of minimal distance on the linearized track as \vec{IP}

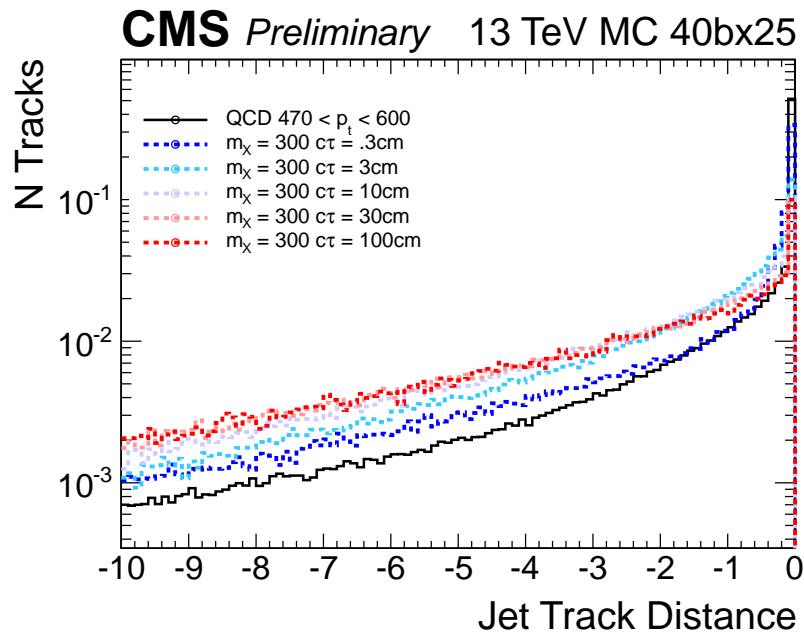


Figure 6.5: The closest distance between the jet axis and track

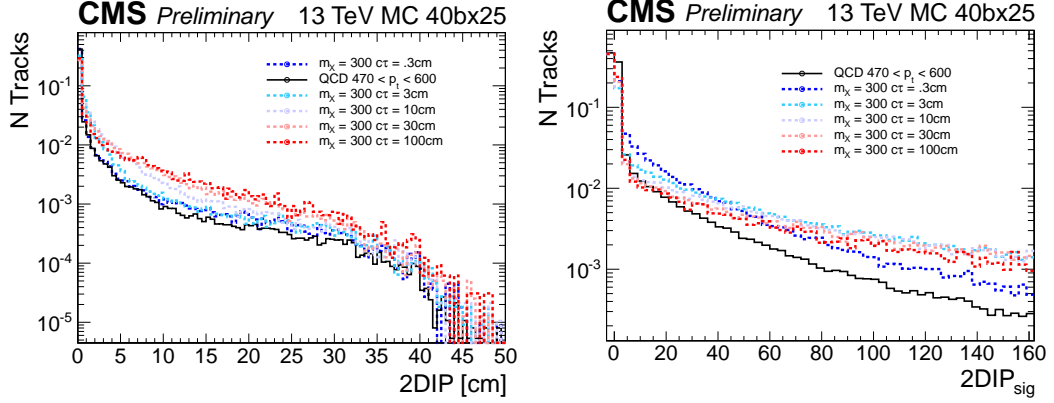


Figure 6.6: The same samples in Fig ?? are shown. (Left) The 2D impact parameter of tracks matched to calo jets matched to generator quarks with $\Delta R < 0.5$. (Right) 2D impact parameter significance of the same tracks. All distributions are normalized to 1.

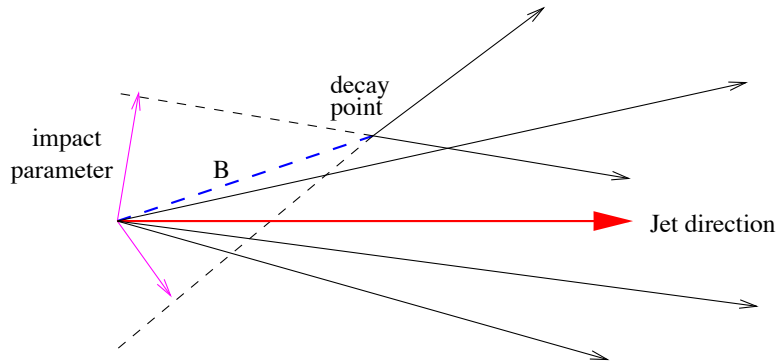


Figure 6.7: Diagram of a B hadron decay showing the mis-alignment of the jet direction from a calo jet and the decay vertex

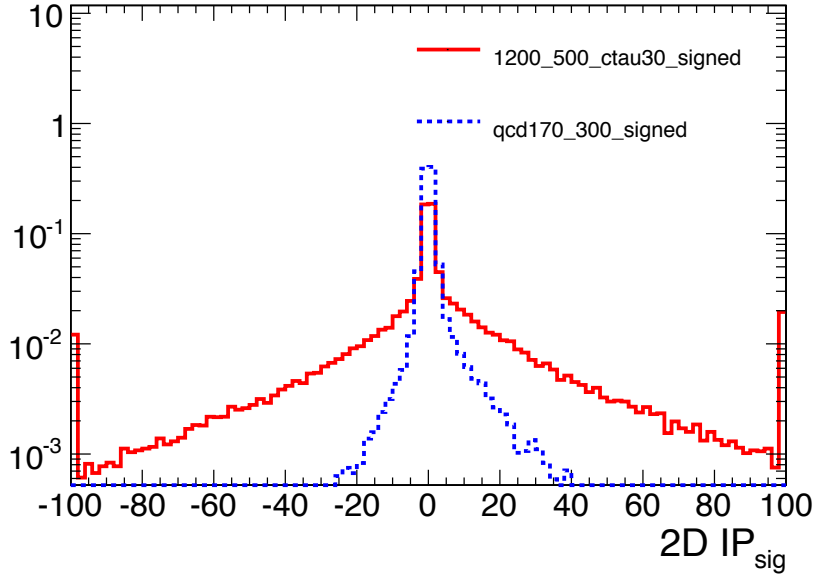


Figure 6.8: Comparison of the $2DIP_{sig}$ of tracks within 1) QCD jets and 2) the less boosted decay of a heavy higgs $H^0 = 1200\text{GeV}$ decaying to two long lived X^0 with $m_X = 500\text{GeV}$. As not all tracks are down stream of long lived flight direction there are tracks with large negative values of $2DIP_{sig}$. The contribution of B mesons producing tracks with large positive $2DIP_{sig}$ can be sign in the asymmetry of the QCD distribution

sign, corresponding to the decay occurring down stream of the jet direction. As the accuracy of the jet direction reconstruction depends on the lifetime of the particle producing the jets (Fig. 6.7), we opt to use un-signed IP significance to identify displaced jets (Fig. 6.6). In example, a case when the signal has large negative values of $2DIP_{sig}$ is shown in Fig 6.8. It is important to note that as most *GUN* samples (excluding the prompt samples) do not have a reconstructed primary vertex, a fake primary vertex with a nominal error is introduced in the calculation. This biases the impact parameter significance relative to the $XX4J$.

To account for the tracking resolution impact parameter significance is introduced. Tracks with impact parameter consistent with the primary vertex relative to the tracking resolution given small impact parameter significance < 5 . For decays

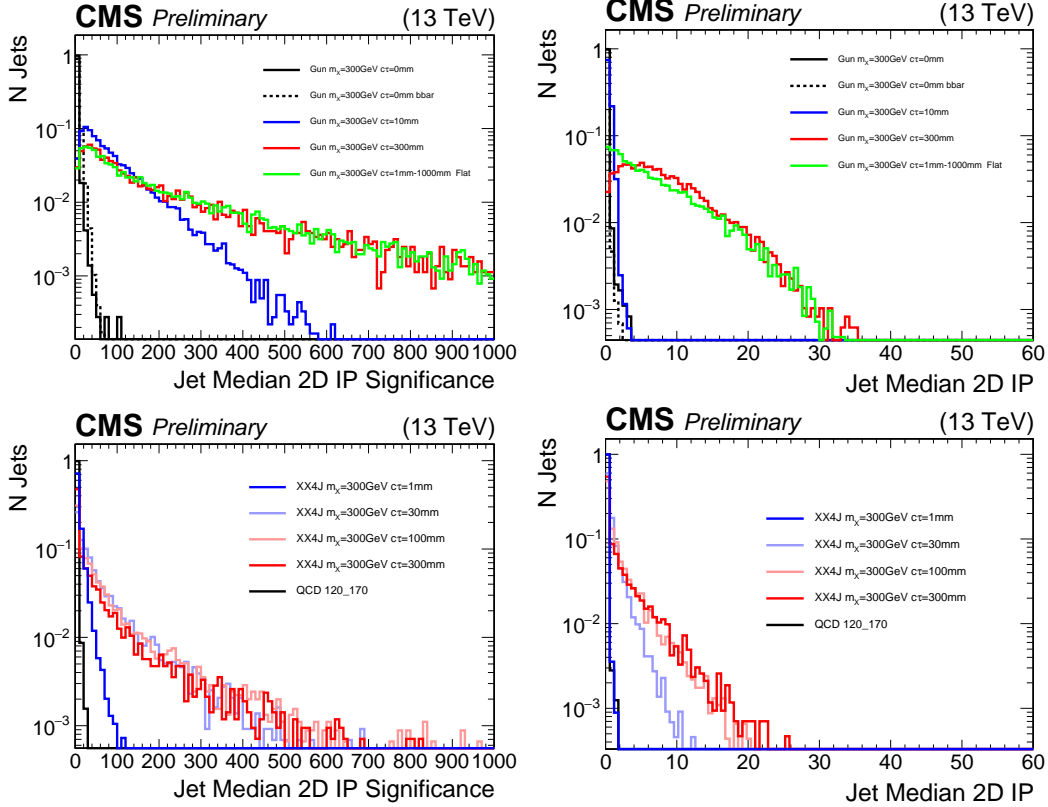


Figure 6.9: Unsigned 2D impact parameter for the $XX4J$ and GUN samples

within $L_{xy} < 10$ mm significance gives significant improvements in signal background separation relative to the absolute impact parameter value Fig. 6.9.

Impact parameter tag info is reconstructed with limited requirements on the tracks. No maximum longitudinal or transverse impact parameter is enforced. No requirement on the number of hits, pixel tracks, or track quality is required at this step. A maximum $\chi^2 < 20$ of the track fit is enforced and a $p_t > 1$ GeV to ensure the track would reach the calorimeter.

Variables leveraging the impact parameter information for a given jet are derived from the distribution of impact parameter significances. Fig. 6.10 demonstrates the improved separation of median IP significance relative to the mean (Fig. 6.10). As background QCD jets contain real displaced tracks (Tab. 2.5, 2.6), the mean

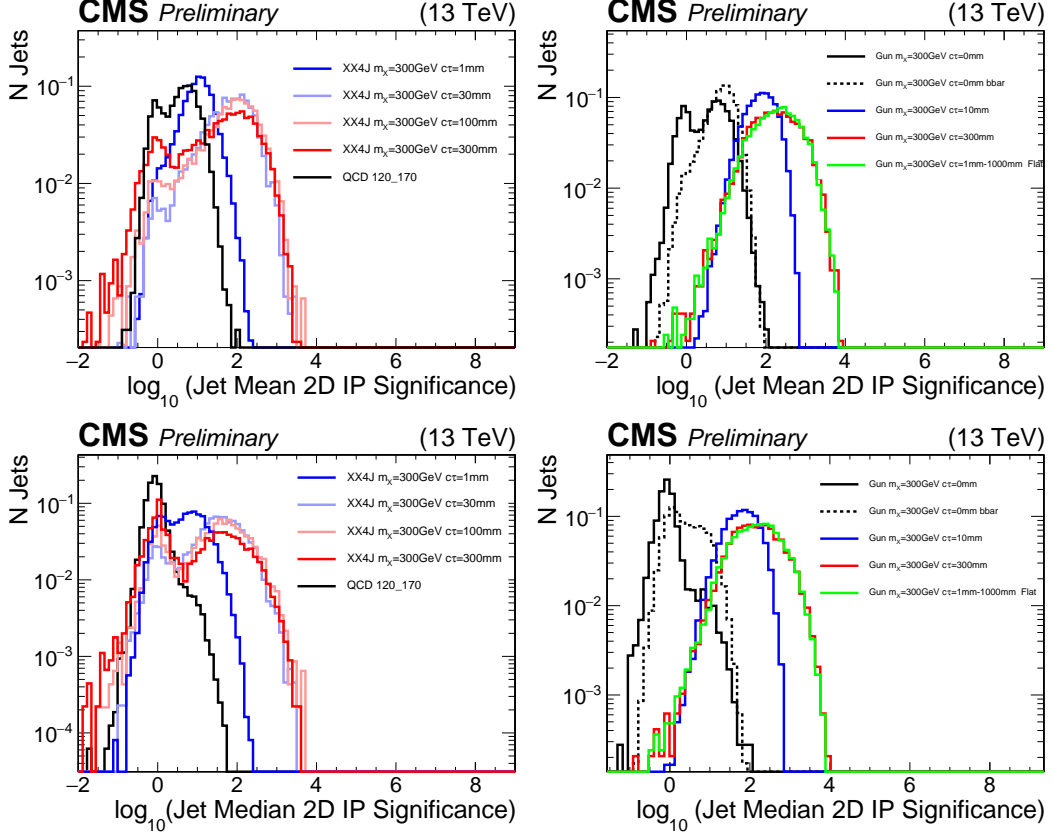


Figure 6.10: A comparison between using mean or median IP significance for the displaced di-jet gun and XX4J signal samples

calculation is sensitive to outlier tracks with large IP significance. For truly displaced jets, all tracks have large impact parameter preserving a high median value.

The tracks from displaced jets should not have significant contribution from tracks included in a primary vertex. This reduces the likelihood of selecting the correct primary vertex for the calculation of 3D impact parameters. Instead, we opt to use exclusively transverse quantities that depend only loosely on the primary vertex selection when a beam-spot constraint is applied. Fig. 6.11 shows the comparison between the 2D and 3D impact parameters showing greater separation for using traverse impact parameters. For the displaced di-jet gun samples, a primary vertex is rarely reconstructed for longer lifetimes. In this case, a fake PV is built and the resulting discrimination power is lost in the longitudinal axis.

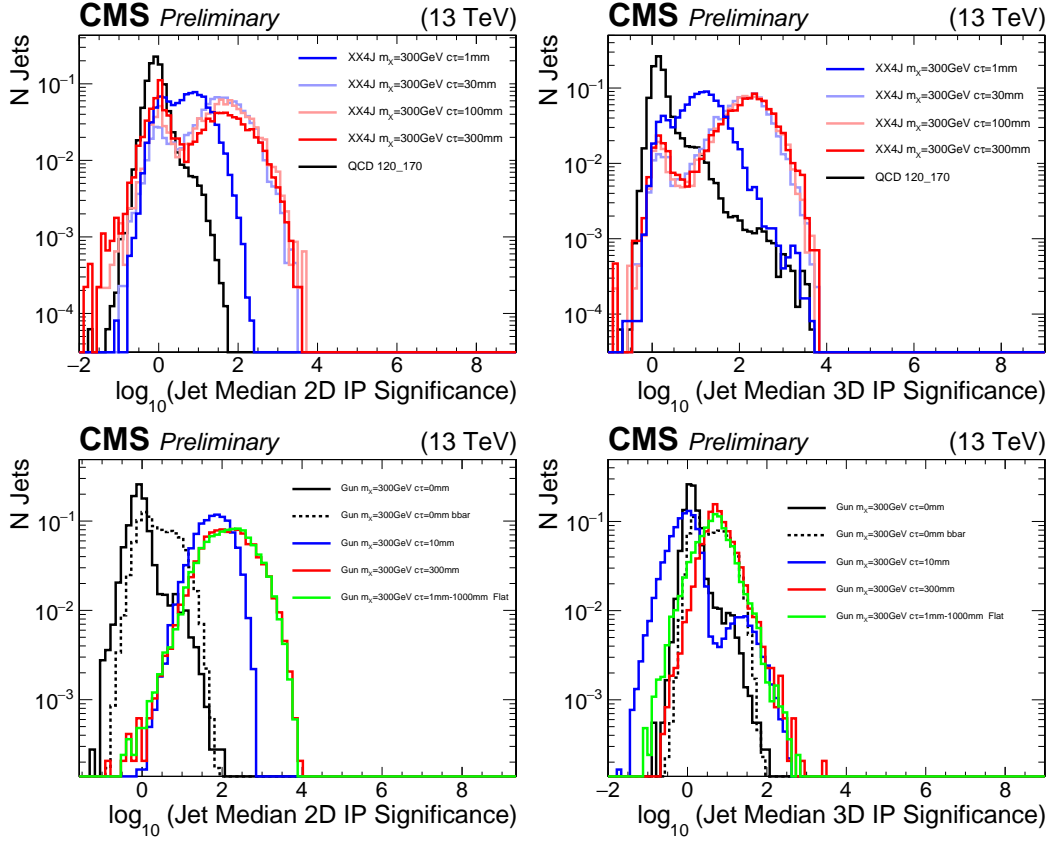


Figure 6.11: A comparison between the median IP Significance in 2D vs 3D for the displaced di-jet gun and XX4J signal samples

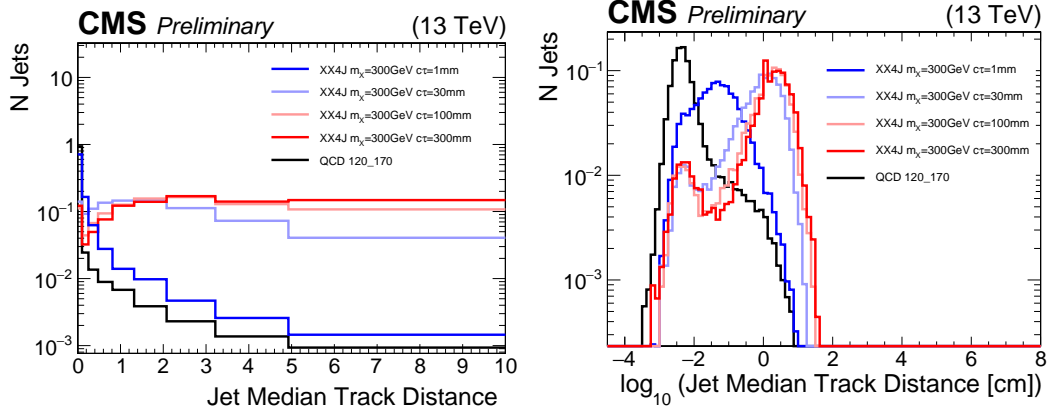


Figure 6.12: For each track in a jet the minimum distance between the track and the jet axis is computed. From this distribution the median is computed for each jet.

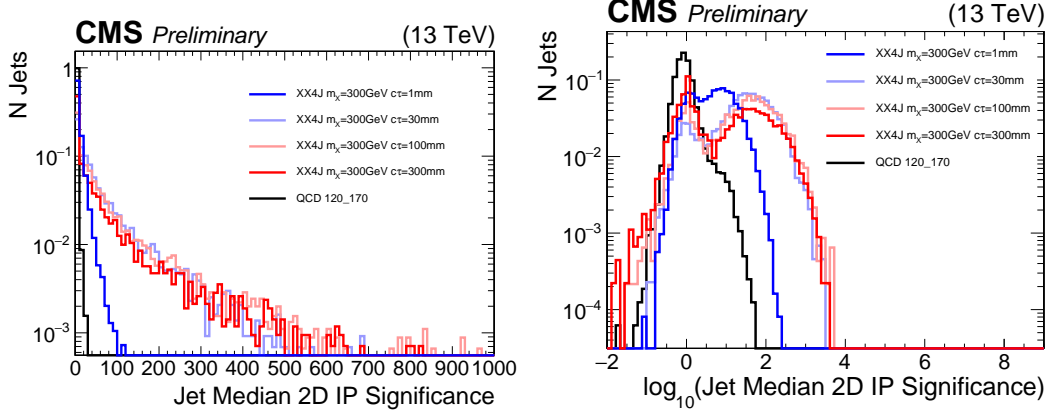


Figure 6.13: A comparison between log and linear scale variables. The log scale case shows the distinct population of significances related to pileup in the $XX4J$ sample.

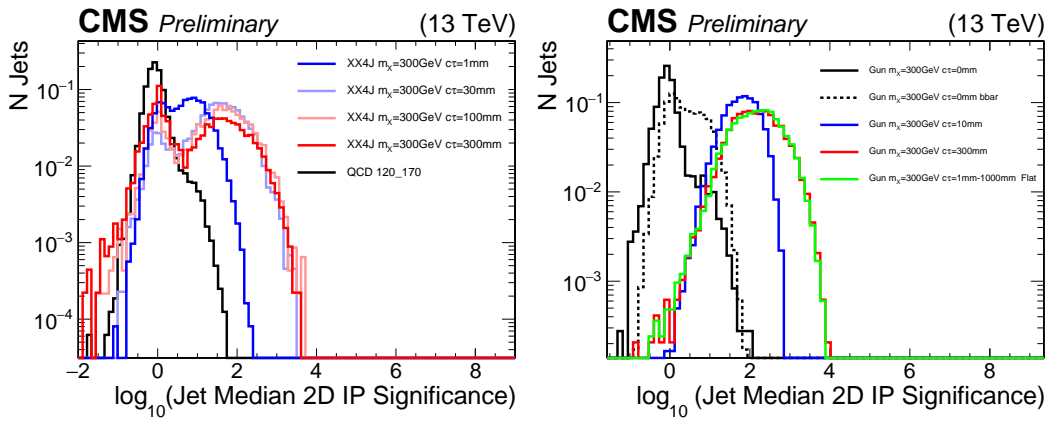


Figure 6.14: A comparison of the Jet Median 2D IP significance between the displaced di-jet gun and $XX4J$ samples

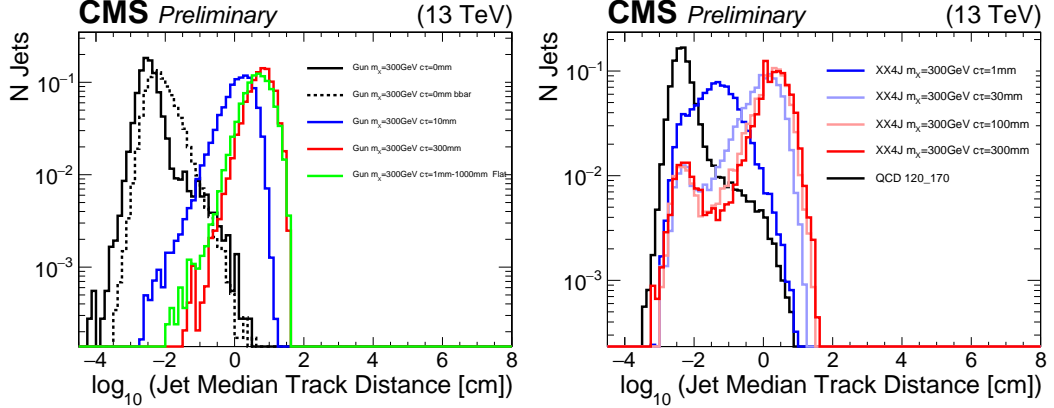


Figure 6.15: The closest distance between the jet axis and track

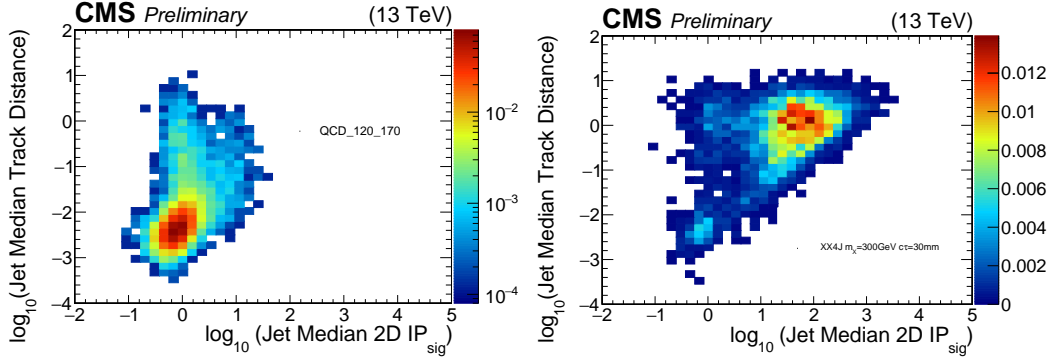


Figure 6.16: Correlations between the IP significance and the jet distance variables

Jet Primary Vertex Fraction (Alpha and Beta)

Jets decaying displaced from the primary vertex are unlikely to contain tracks included in the event's primary vertex fit when a beam spot constraint is included. QCD jets, expect the majority of their tracks to be from either the true primary vertex or a pile up vertex. For a given jet $\alpha(PV)$ is calculated as the sum is taken over tracks matching in $\Delta R < 0.4$ between two collections of tracks: the tracks in the specified primary vertex and tracks from the `generalTracks` collection. The sum is restricted to tracks with $p_t > 1.0$ GeV.

$$\alpha_{jet}(PV) = \frac{\sum_{i \in PV, tracks} p_t^i}{\sum_{j \in generalTracks} p_t^j} \quad (6.1)$$

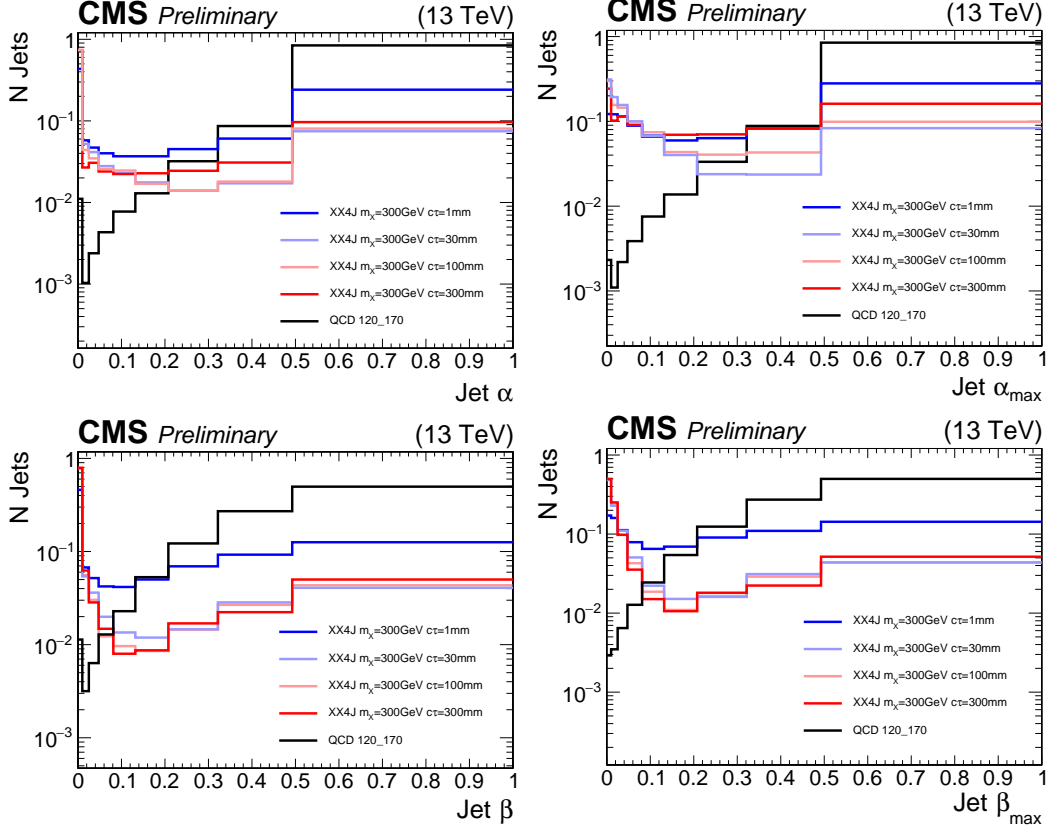


Figure 6.17: $\alpha, \alpha_{max}, \beta, \beta_{max}$ when varying the lifetime of the decaying X^0

If a single PV is selected for all jets in the event, PU jets which are not from this vertex can have signal-like $\alpha \approx 0$. To avoid this we define α_{max} for each jet individually selecting the primary vertex with the largest contribution to the sum. The assumption is PU jets will have high α for at least one of the vertices. Many events with $\alpha = 0$ have $\alpha_{max}! = 0$ as they originate from a sub-leading vertex in the `offlinePrimaryVerticesWithBS` collection. Because the **GUN** samples typically have no reconstructed primary vertices (except in the prompt case), these plots are not shown.

A second jet variable $\beta(PV)$ and β_{max} are defined similarly:

$$\beta_{jet}(PV) = \frac{\sum_{i \in PV, tracks} p_t^i}{p_{t,jet}} \quad (6.2)$$

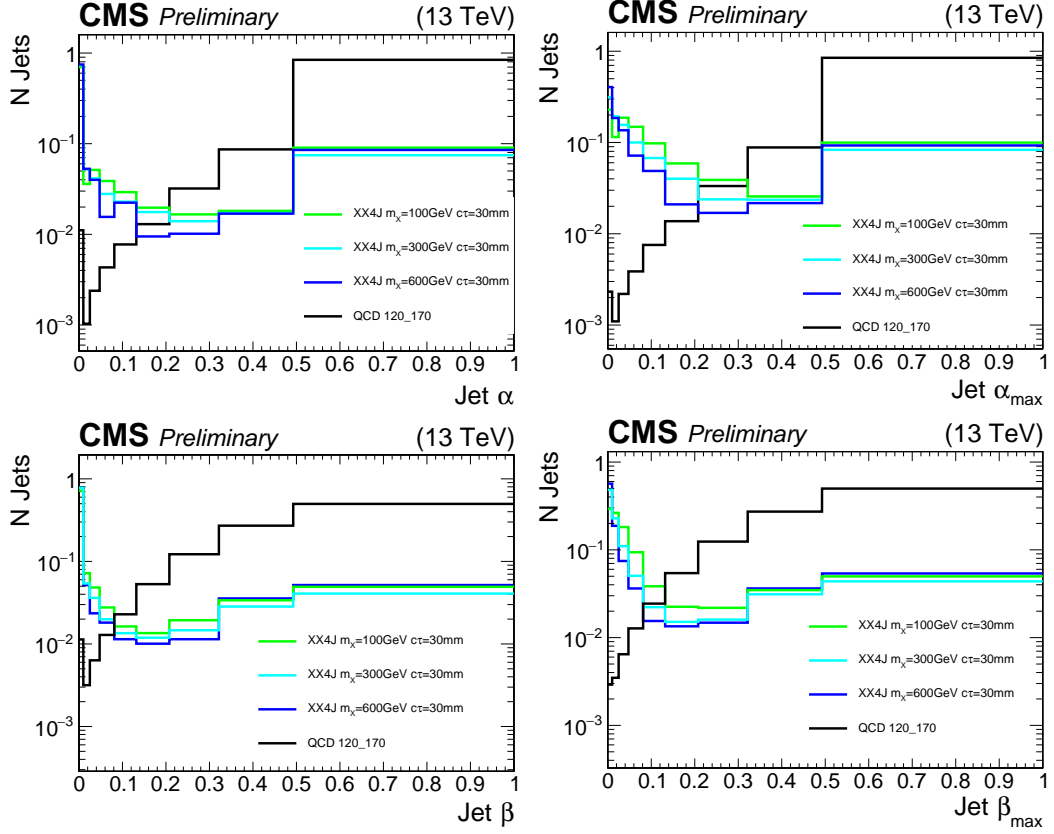


Figure 6.18: $\alpha, \alpha_{max}, \beta, \beta_{max}$ when varying the mass of the decaying X^0

A comparison of the four variables: $\alpha, \alpha_{max}, \beta, \beta_{max}$ is shown in Fig. 6.17 varying the lifetime of the sample and in Fig. 6.18 varying the mass for fixed lifetime.

Fig 6.19 show α_{max} has small correlation in background with the median 2D IP significance and β_{max} less so. This is because α_{max} is a function of the tracks matched to the jet, which are utilized in the median IP significance calculation. At low values of α_{max} we find the best separation between signal and background.

6.4.2 Calo Jet Information

In the case which there are no tracks to identify the decay as displaced, we can utilize the high hadronic energy fraction of jets that occur from decays in the hadronic

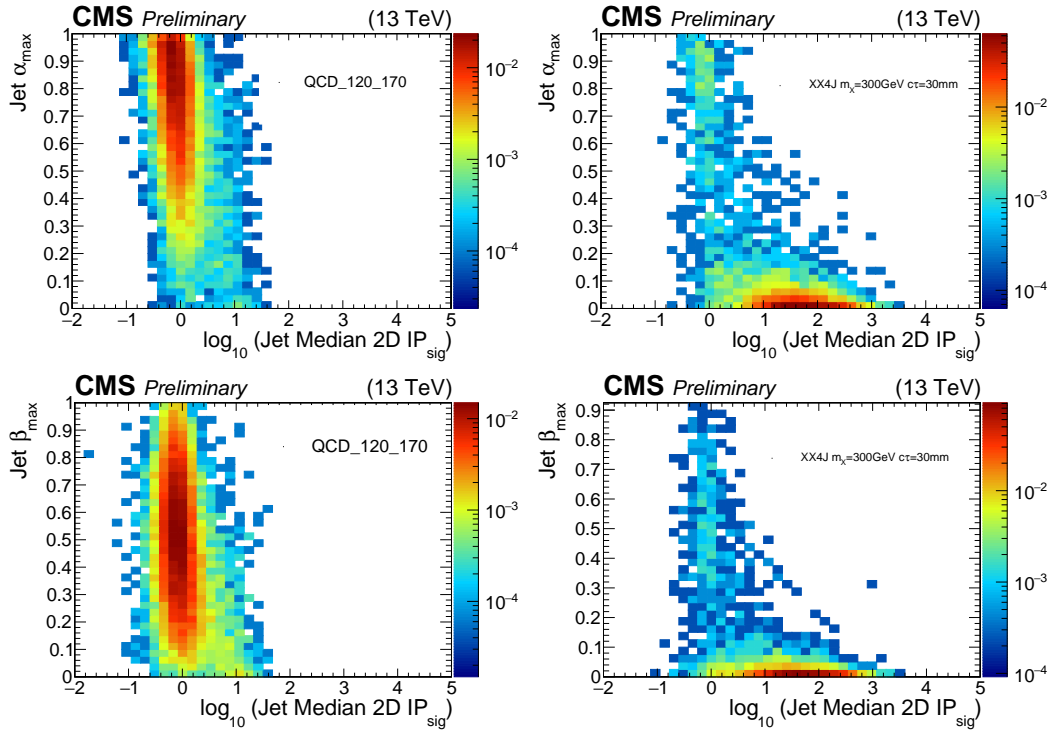


Figure 6.19: (Left) The correlation between α_{\max} and β_{\max} and median 2D IP significance for QCD (Right) The same for XX4J with $m_X = 300 \text{ GeV}$ and $c\tau = 30 \text{ mm}$

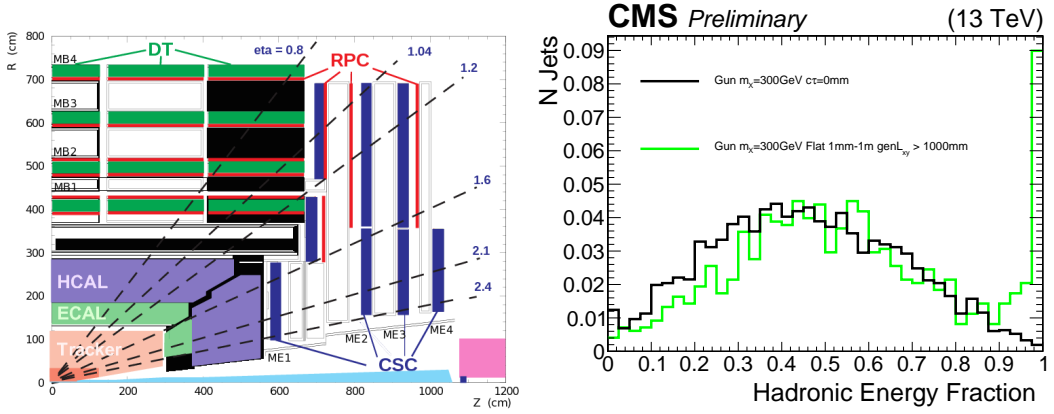


Figure 6.20: (Left) A longitudinal slice of the CMS detector showing the transverse coverage of the tracking layers. (Right) Hadronic fraction of jets in events with generator level requirement that the X^0 decay at a transverse distance $L_{xy} > 100 \text{ cm}$

calorimeter. Fig. 6.20 applies a generator level cut on the transverse decay distance of $L_{xy} > 100$ cm to insure that the decay occurs outside of the tracker.

Chapter 7

Displaced Jet Analysis

7.1 Introduction

The study of physics beyond the standard model (BSM) is one of the main objectives of the ATLAS and CMS experiments at the CERN LHC. With no signal observed so far, the ATLAS and CMS results put severe bounds on BSM theories.

The majority of these searches focus on prompt particles with lifetimes $c\tau_0 < 1\text{mm}$ and contain requirements on the physics objects that reject longer lived particle decays. This leaves open the possibility that light long-lived particles could exist and still remain undetected. In this paper, we present an inclusive search for long-lived particles decaying to various combinations of jets and leptons. The analysis exploits the information originating from the CMS calorimeters to reconstruct jets and measure their energies. The information from reconstructed tracks, in particular the transverse impact parameters, is used to discriminate the displaced-jets signal from the background of ordinary multijet events. The analysis is performed on data collected with the CMS detector at a center-of-mass energy $\sqrt{s} = 13\text{ TeV}$ in 2015. The data set corresponds to an integrated luminosity of 2.7fb^{-1} . Results for similar

signatures have been reported by ATLAS [1, 2] and CMS [3], using data collected at $\sqrt{s} = 8$ TeV.

7.2 Datasets

7.3 An inclusive displaced-jet tagger

The basic requirement for the displaced jet tagging criteria is at least a single track with $p_t > 1$ GeV. Besides the requirements implicitly enforced on the iterative tracking in the `generalTracks` collection, there are no further requirements (no total and pixel hit requirements). All tracking related variables for tagging are computed with this collection of tracks i.e. `generalTracks` with $p_t > 1$ GeV. There are no energy composition requirements of the calorimeter deposit and no requirements of a reconstructed secondary vertex, both of which can exclude sensitivity to long-lived decays to electrons and single prong taus.

All variables utilize 2D quantities. By excluding the longitudinal dimension we prevent large overestimation of displacement due to primary vertex mis-identification. When the signal model in question has a lifetime small on the scale of the longitudinal spread of pile up the primary vertex can still be accurately reconstructed. In contrast, for a decay in the lab frame of a few centimeters the probability of selecting the correct primary vertex can be highly model dependent. In fact, with beam spot constraints applied and no initial state radiation it is possible the primary vertex would not be reconstructed at all. This is especially the case for relatively light particles produced with lifetimes longer than the beamspot radius. By utilizing the `offlineBeamSpotWithBS` collection to compute primary vertex related quantities we limit the transverse spread relative to the z direction to approximately 0.001 cm. As

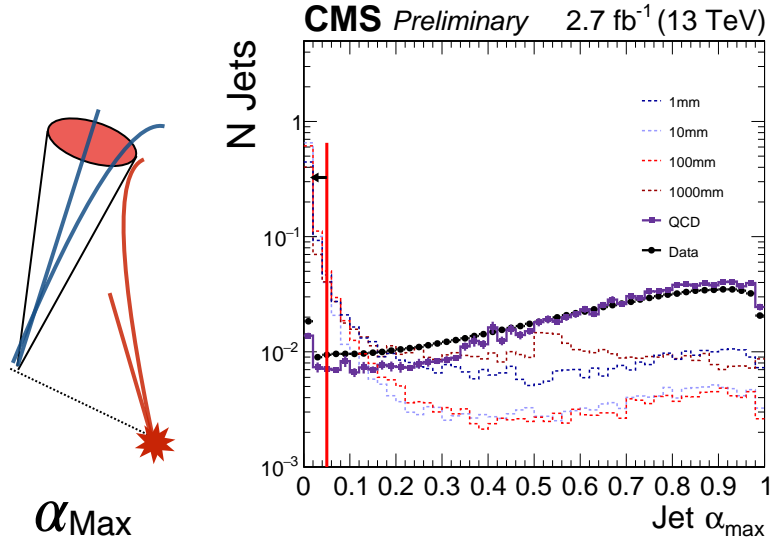


Figure 7.1: Diagram (left) and data/MC comparison (right) for the displaced jet tagging variable α_{max} . The left distribution shows the data collected by the displaced jet triggers with kinematic cuts and H_T trigger matching thresholds applied. Signal samples are taken from Jet-Jet interpretation with no generator matching for the signal jets, fixed $m_X = 700$ GeV and varied proper lifetime $c\tau_0$ in the mother frame.

the tag sensitivity becomes highly insensitive at distances smaller than 1 mm, the effect of choosing the wrong PV is negligible.

In contrast to previous analyses, a fitted secondary vertex is not utilized in the tag definition. This decision is deliberate to maintain sensitivity to electrons and single track taus while maintaining a single definition. Previous analyses had possible sensitivity by fitting a secondary vertex to pairs of jets containing a single track. Additionally, by not vertexing pairs of jets the displaced object allows for sensitivity to odd (non-even) multiplicities of displaced jets. For example, in the Jet-Jet interpretation there is sensitivity to 3 jets when the 4th is reconstructed outside of the tracker acceptance.

The Primary Vertex Compatibility Variable Alpha Max

The variable α_{max} characterizes the disassociation of the jet's tracks and all fitted primary vertices in an event. Jets decaying displaced from the primary vertex are unlikely to contain tracks included in the event's primary vertex fit. Background QCD jets, will contain a majority of tracks from either the true primary vertex or a pile up vertex. For a given jet $\alpha(PV)$ is calculated as the ratio of sums of p_t taken over tracks matching in $\Delta R < 0.4$ between two collections of tracks: the tracks in the specified primary vertex and tracks from the `generalTracks` collection. The sum is restricted to tracks with $p_t > 1.0$ GeV.

$$\alpha_{jet}(PV) = \frac{\sum_{i \in PV, tracks} p_t^i}{\sum_{j \in generalTracks} p_t^j} \quad (7.1)$$

If a single PV is selected for all jets in the event, PU jets which are not from this vertex can have signal-like $\alpha \approx 0$. To avoid this, we define α_{max} for each jet individually selecting the primary vertex with the largest contribution to the sum. The assumption is PU jets will have high α for at least one of the vertices. Many jets with $\alpha = 0$ have $\alpha_{max} > 0$ as they originate from a sub-leading vertex in the `offlinePrimaryVerticesWithBS` collection. As the variable is calculated relative to all primary vertices, there is no dependence on selecting a single vertex.

The 2D Angle $\hat{\Theta}_{2D}$

The variable Θ_{2D} is utilized to characterize the recoil angle of the tracks from the flight direction of the long lived particle. Θ_{2D} is defined as the angle between 1) the 2D ray extended from the primary vertex to the inner hit of the track and 2) the track 2D momentum vector at the inner hit of the track extended from the inner hit. The first vertex in the `offlinePrimaryVertexWithBS` collection is selected for all jets in the event.

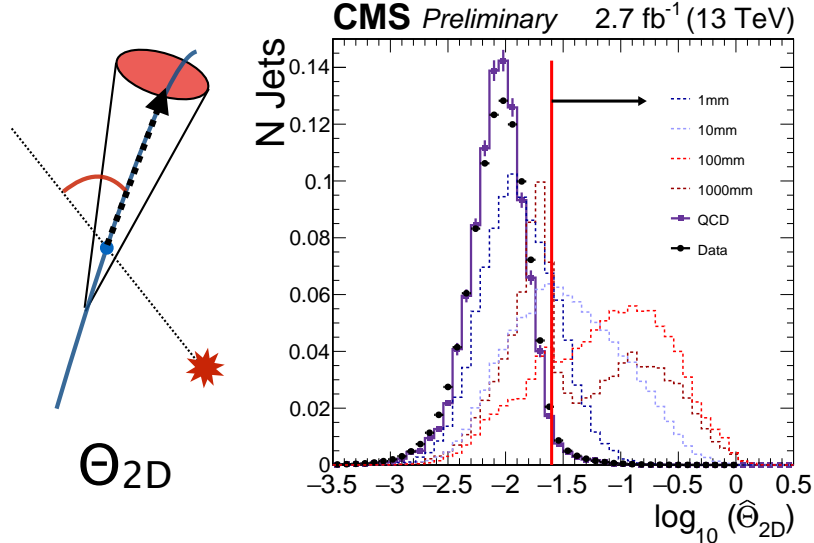


Figure 7.2: Diagram (left) and data/MC comparison (right) for the displaced jet tagging variable θ_{2D} . The left distribution shows the quantities collected by the displaced jet triggers with kinematic cuts and H_T trigger matching thresholds applied. Signal samples are taken from Jet-Jet interpretation with no generator matching for the signal jets, fixed $m_X = 700$ GeV and varied proper lifetime $c\tau_0$ in the mother frame.

As Standard Model QCD jets do contain long lived particles and tracks associated to conversions, a typical jet has a long tail in its distribution of Θ_{2D} . To minimize the effect of this tail, the median value (2D) is used, $\hat{\Theta}_{2D}$ (for the same reasons as it is used for $2DIP_{sig}$). Additionally, as the range of Θ_{2D} spans many orders of magnitude near zero a logarithm is applied constraining typical QCD jet values of $-2.5 < \log(\hat{\Theta}_{2D}) < -1$.

As mentioned previously, the smaller the boost of the particle, the more isotropic the decay angles. Thus, the decays of heavier long-lived particles yield larger values of Θ_{2D} . When the lifetime of the particle is small near 1 mm it is more difficult to resolve this angle because the ray's extrapolation backward corresponds to a smaller and smaller distance from the primary vertex. As the lifetime approaches a few centimeters the signal is up to 50% efficient in a nearly background free regime.

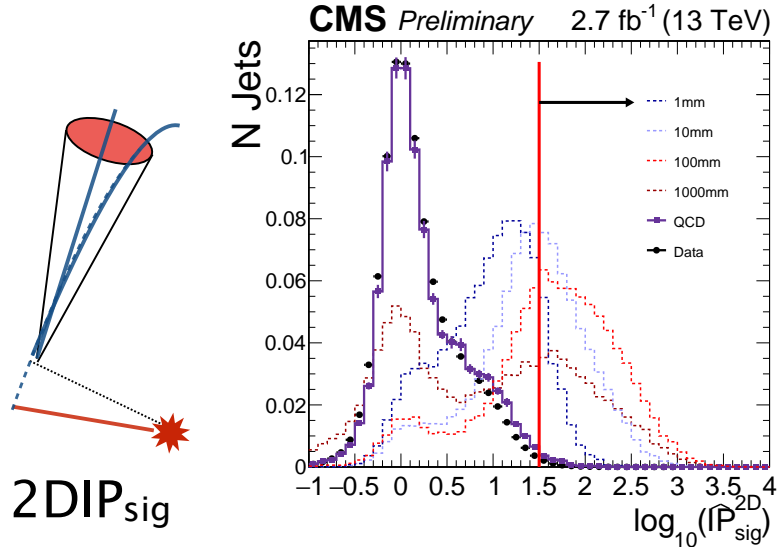


Figure 7.3: Diagram (left) and Data vs. Monte Carlo comparison (right) for the displaced jet tagging variable $2DIP_{sig}$. The left distribution shows the quantities collected by the displaced jet triggers with kinematic cuts and H_T trigger matching thresholds applied. Signal samples are taken from Jet-Jet interpretation with no generator matching for the signal jets, fixed $m_X = 700$ GeV and varied proper lifetime $c\tau_0$ in the mother frame.

Background jets capable of passing tight Θ_{2D} requirements typically consist of a single track.

Jet \hat{IP}_{sig}^{2D}

Variables leveraging the impact parameter information for a given jet are derived from the distribution of impact parameter significances derived from the tracks matched to the jet. As background QCD jets contain a long tail from the presence of real displaced tracks with large IP significance, the median $2DIP_{sig}$ is chosen: \hat{IP}_{sig}^{2D} . For jets originating from displaced decay, most tracks have a large impact parameter preserving a high median value.

Table 7.1: The baseline tag definition in terms of the three displaced jet tagging variables

Variable	$\log_{10}(x)$	Requirement	Linear Requirement
α_{max}		N/A	< 5%
$\hat{I}P_{sig}^{2D}$		> 1.5	> 31.6
$\hat{\Theta}_{2D}$		> -1.6	> 0.025

Table 7.2: The loose tag definition in terms of the three displaced jet tagging variables.

Variable	$\log_{10}(x)$	Requirement	Linear Requirement
α_{max}		N/A	< 50%
$\hat{I}P_{sig}^{2D}$		> 0.434	> 2.71
$\hat{\Theta}_{2D}$		> -1.70	> 0.02

7.3.1 Tagging Variable Cut Optimization

The requirements included in the baseline tag definition are determined through a scan of the possible parameter space. The values of the tagging variables scanned can be found in Table 7.4. Firstly, a scan is performed to determine the optimal selection relative to a figure of merit that is maximal labeled $fom_{max}(x)$ for a given sample $x \in X$ where X is the set of training samples. The figure of merit for a given sample $x \in X$ and selection $s_i \in S$ is computed as $fom(x, s_i) = \bar{N}(s_i, x) / \sqrt{\bar{N}(s_i, x) + \hat{N}_b(s_i)}$ where \bar{N} is the average number of jets tagged per event passing the event selection and \hat{N}_b is an estimate number of background events in the two tag bin. This estimation

Table 7.3: The integrated fake-rate is precisely N_{tagged}/N_{jets} for all jets passing the jet selection in events passing the event selection in data collected by the displaced jet triggers.

Working Point	Flat Fake-Rate / Probability
Loose Tag	2.5816%
Baseline Tag	0.0496%

Table 7.4: The values of the tagging variables included in the scan for selecting the baseline tag definition

Tagging Variable	Begin Scan	End Scan	Step Size	N Points
α_{max}	0	0.5	0.05	11
$\log_{10}(\hat{IP}_{sig}^{2D})$	0.0	2.5	0.1	26
$\log_{10}(\hat{\Theta}_{2D})$	-2.5	-0.5	0.1	21

\hat{N}_b is calculated as the total number of jets tagged in data times the fake rate $\hat{N}_b(s_i) = N_{jets-tagged}^{data} \times \frac{N_{jets-tagged}^{data}}{N_{jets}^{data}}$. Once fom_{max} is calculated for every sample and selection we choose the tagging requirements which minimize sum of the differences squared of the figure of merit $fom(s_i, x)$ relative to the maximal value fom_{max} Eq. 7.2.

$$\chi^2(s_i) = \sum_{x \in X} \left(\frac{(fom(s_i, x) - fom_{max}(x))^2}{fom_{max}(x)} \right) \quad (7.2)$$

The training set is chosen as the set of all Jet-Jet samples with $c\tau_0 = 1, 3$ mm. This set is chosen as it is the most difficult region for the analysis with the largest upper limit on the excluded cross-section.

7.4 Event selection

A signal is searched for by applying the selection described in section ?? and counting the number of tagged displaced jets, N_{tags} . In addition to the online and offline requirements described in section 7.5, the analysis signal region requires $N_{tags} \geq 2$. Efficiencies are reported for all interpreted models as a function of the lifetime with fixed mass (Table 7.5 and 7.6) as well as a function of mass with fixed lifetime (Table 7.7 and 7.8).

Table 7.5: Signal efficiency for fixed $m_X = m_{\tilde{t}} = 300$ GeV and varied $c\tau_0$ for the Jet-Jet and B-Lepton models. Selection requirements are cumulative from the first to the last row.

Jet-Jet				
m_X [GeV]	300	300	300	300
$c\tau_0$ [mm]	1	10	100	1000
≥ 2 tags	$2.33 \pm 0.15\%$	$39.49 \pm 0.63\%$	$54.54 \pm 0.74\%$	$14.58 \pm 0.38\%$
Trigger	$2.16 \pm 0.15\%$	$38.12 \pm 0.62\%$	$39.32 \pm 0.63\%$	$8.07 \pm 0.28\%$
Event sel.	$2.09 \pm 0.14\%$	$37.09 \pm 0.61\%$	$36.53 \pm 0.60\%$	$6.67 \pm 0.26\%$
≥ 3 tags	$0.170 \pm 0.041\%$	$14.14 \pm 0.38\%$	$16.72 \pm 0.41\%$	$1.36 \pm 0.12\%$
≥ 4 tags	$0.010 \pm 0.010\%$	$4.73 \pm 0.22\%$	$4.71 \pm 0.22\%$	$0.170 \pm 0.041\%$

B-Lepton				
$m_{\tilde{t}}$ [GeV]	300	300	300	300
$c\tau_0$ [mm]	1	10	100	1000
≥ 2 tags	$0.453 \pm 0.023\%$	$15.82 \pm 0.13\%$	$31.52 \pm 0.19\%$	$8.545 \pm 0.098\%$
Trigger	$0.291 \pm 0.018\%$	$11.45 \pm 0.11\%$	$17.08 \pm 0.14\%$	$3.224 \pm 0.060\%$
Event sel.	$0.269 \pm 0.017\%$	$9.91 \pm 0.11\%$	$13.33 \pm 0.12\%$	$2.084 \pm 0.048\%$
≥ 3 tags	$0.017 \pm 0.004\%$	$2.462 \pm 0.053\%$	$3.814 \pm 0.065\%$	$0.368 \pm 0.020\%$
≥ 4 tags	–	$0.297 \pm 0.018\%$	$0.480 \pm 0.023\%$	$0.0315 \pm 0.0060\%$

The two classes of events: (i) events passing the inclusive trigger algorithm and with $H_T > 650$ GeV; (ii) events passing the exclusive trigger algorithm and with $H_T > 450$ GeV are treated as a single class.

7.5 Datasets and simulated samples

Events are collected from two dedicated online selection algorithms, designed to identify events with displaced jets. The algorithms consider jets clustered from energy deposits in the calorimeters, using the FASTJET [4] implementation of the anti- k_t algorithm [5], with size parameter 0.4. Jets with transverse momentum $p_t < 60$ GeV or $|\eta| > 2.0$ are discarded. An inclusive trigger algorithm accepts events when the scalar sum of the jet p_t 's, H_T , is greater than 500 GeV and at least two jets with $|\eta| < 2.0$ and at most two prompt tracks are found. Tracks are classified as prompt if

their transverse impact parameter relative to the beam line, IP^{2D} , is less than 1mm. Another trigger algorithm is used, which requires $H_T > 350$ GeV and asks that there be two displaced jets each having at least one track with transverse impact parameter $IP^{2D} > 5\sigma_{IP^{2D}}$, where $\sigma_{IP^{2D}}$ is the uncertainty on IP^{2D} . Samples with large H_T are used to study the performance of the online selection algorithms.

Events are selected offline requiring at least two jets with $p_t > 60$ GeV and $|\eta| < 2.0$. As for the online selection, the offline jet reconstruction is performed clustering energy deposits in the calorimeters with the anti- k_t algorithm, with jet size parameter of 0.4. Two classes of events are considered: (i) events passing the inclusive trigger algorithm and with $H_T > 650$ GeV and (ii) events passing the exclusive trigger algorithm and with $H_T > 450$ GeV. The two classes of events sum to 786,002 unique events passing the event selection.

The main source of background events originates from multijet production. The properties of this background process are studied using a simulated multijet sample, generated with PYTHIA 8 [6]. The NNPDF 2.3 [7] parton distribution functions (PDFs) are used to model the parton momentum distribution inside the colliding protons. The event simulation includes the effect of multiple proton-proton collisions in the same bunch crossing and in bunch crossing nearby in time, referred to as pileup. Simulated samples are reweighted to match the pileup profile observed in data.

The analysis is interpreted with a set of benchmark signal models. The **Jet-Jet** model predicts pair-produced long-lived scalar neutral particles X^0 [8], each decaying to two light quarks u,d,s,c, and b with equal probability. The resonance mass m_X and proper lifetime $c\tau_0$ are scanned between 50 and 1500 GeV and between 1 and 2000mm, respectively. The trigger efficiencies for a fixed $m_X = 300$ GeV and $c\tau_0 = 1, 30$, and 1000 mm are 30%, 81%, and 42% respectively. The trigger efficiencies for a fixed $c\tau_0 = 30$ mm and $m_X = 50, 100$, and 1000 GeV are 2%, 14%, and 92% respectively.

The **B-Lepton** model contains pair-produced long-lived top squarks in R-parity violating models of Supersymmetry [9]. Each top squark decays to one b quark and a lepton. The branching fractions of the decay to the three lepton flavors are equal. The resonance mass $m_{\tilde{t}}$ and proper lifetime $c\tau_0$ are scanned between 300 and 1000GeV and between 1 and 1000mm, respectively. The trigger efficiencies for a fixed mass $m_{\tilde{t}} = 300$ GeV and $c\tau_0 = 1, 30$, and 1000 mm are 15%, 41%, and 23% respectively. The trigger efficiencies for $m_{\tilde{t}} = 500, 700$, and 1000 GeV and fixed $c\tau_0 = 30$ mm are 64%, 71%, and 74% respectively.

These models are also investigated with modified branching fractions. The **Light-Light** model is the Jet-Jet model excluding decays to b quarks (equal decays to lighter quarks) and the **B-Mu**, **B-Ele**, and **B-Tau** models are derived from the B-Lepton model with 100% branching fraction to muons, electrons, and taus, respectively. Leptonic tau decays are included in the **B-Tau** interpretation. All signal samples are generated with PYTHIA, with the setup described above for the multijet sample.

7.6 Background prediction

As typical multijets contain only a sub dominant fraction of real displaced tracks, jets with a small multiplicity of tracks represent the dominant background. As the tagging criteria utilize averages of all tracks matched to the jet, the likelihood of tagging a fake decreases exponentially with N_{tracks} .

Figure 7.4 shows the fraction of jets that are tagged as displaced jets in data as a function of the number of tracks associated with the jet N_{tracks} . This function is the misidentification rate of tagging a prompt jet as displaced (up to possible signal contamination) and is interpreted as the probability $p(N_{\text{tracks}})$ of being tagged. This parameterization allows for a representative estimation, event by event, of the probability of tagging multiple fake displaced jets. That is to say, an event with two

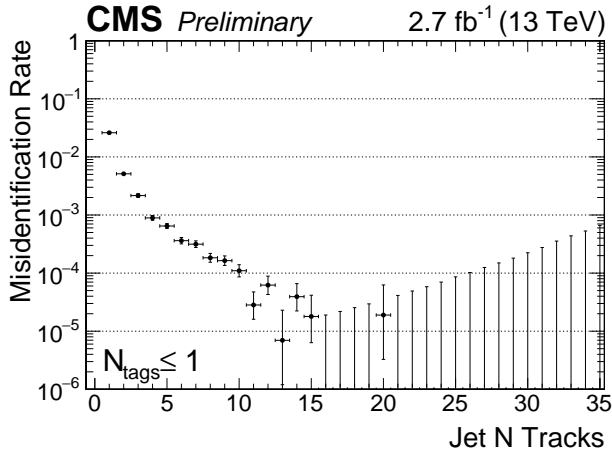


Figure 7.4: The fraction of jets passing the displaced-jet tagging criteria as a function of the number tracks associated with the jet N_{tracks} . The results are from data events with $N_{\text{tags}} \leq 1$ collected with the displaced-jet triggers and passing the offline selection criteria.

high track multiplicity jets is much less probable than two single track jets to have 2 fake displaced-jet tags.

To maintain the statistical independence of the events that are used to perform the prediction and the events in the signal region, the probabilities are measured in the full control sample of events with $N_{\text{tags}} \leq 1$, while the final signal region requires $N_{\text{tags}} \geq 2$. Additionally, this limits signal contamination in the probability measurement. The control sample of $N_{\text{tags}} = 1$ includes 1391 events.

The size of the bias introduced by only measuring the misidentification rate in events with $N_{\text{tags}} \leq 1$ is quantifiable. For the nominal tag the size of the effect of removing these events on the predicted number of two tag events is negligible (0.4%) compared to the statistical uncertainty of the prediction.

The mistagging rate is used to predict the probability for an event to have N_{tags} tagged jets, $P(N_{\text{tags}})$. For instance, for an event m with three jets j_1 , j_2 , and j_3 ,

there is one configuration with no tags, with a probability:

$$P^m(N_{\text{tags}} = 0) = (1 - p_1)(1 - p_2)(1 - p_3) ,$$

where $p_i = p(N_{\text{tracks}}(j_i))$. Similarly, there are three possibilities for this same event to have $N_{\text{tags}} = 1$:

$$P^m(N_{\text{tags}} = 1) = p_1(1 - p_2)(1 - p_3) + (1 - p_1)p_2(1 - p_3) + (1 - p_1)(1 - p_2)p_3 .$$

The probability of finding N_{tags} tags in the m event is:

$$P^m(N_{\text{tags}}) = \sum_{\text{jet-configs}} \prod_{i \in \text{tagged}} p_i \prod_{k \in \text{not-tagged}} (1 - p_k) . \quad (7.3)$$

Tagged jets enter the product as p_i and non-tagged jets enter as $(1 - p_i)$. Equation (7.3) is used to compute the probability of observing N_{tags} , under the assumption that the sample does not contain any signal. The number of events expected for a given value of N_{tags} is then computed as

$$N_{\text{events}}(N_{\text{tags}}) = \sum_m P^m(N_{\text{tags}}) , \quad (7.4)$$

where m runs only over events with fewer than two tagged jets. The prediction is then compared to the observed N_{tags} multiplicity in events with two or more tagged jets, to assess the presence of a signal.

Let q_i be the misidentification rate corresponding to a jet with i tracks and N_{tracks} the maximum number of tracks for any jet in the analysis. The statistical error σ_{q_i} in the misidentification rate is propagated to an error on the number of tagged events

with $N_{tags} = 1, 2, 3, \dots$

$$\begin{aligned}\sigma_{N_{n-tags}}^2 &= \sum_{i=1}^{N_{tracks}} \left(\frac{\partial N_{n-tags}}{\partial q_i} \sigma_{q_i} \right)^2 \\ &= \sum_{i=1}^{N_{tracks}} \left(\left(\sum_{m \in N_{events}} \frac{\partial P^m(N_{tags} = n)}{\partial q_i} \right) \sigma_{q_i} \right)^2\end{aligned}$$

The probability is determined for each event for $N_{tags} \leq N_{jets}$. The predicted number of events with N_{tags} is calculated as the sum over all events Eq. ??.

We validate this procedure in the absence (background-only test) and presence (signal-injection test) of a signal, using simulated events.

The background-only test is performed predicting the tag multiplicity on the simulated multijet sample, taking as input the misidentification rate distribution. In order to populate the large- N_{tags} region of the distribution, a looser version of the displaced-jet tagger is employed in this test. The full sample of events passing the event selection is divided into multiple independent samples and the background prediction validated. The predicted background of N_{tags} events in simulated multijet events is found to be consistent within statistical uncertainty.

7.6.1 Signal Injection Tests

Injection with QCD

To test the response of the background prediction to the presence of signal contamination in the jet probabilities used for the $P(N_{tags})$ derivation, signal events are ‘injected’ into QCD Monte Carlo. Approximately 15 million QCD events from /QCD_HT700to1000_TuneCUETP8M1_13TeV-madgraphMLM-pythia8 are used as the background input. The resulting predictions for varied masses, lifetimes, and sizes of contamination are shown in Fig. 7.5 and Fig. 7.6. The corresponding predictions, observed number of tags, and the deviation from expectation are summarized in

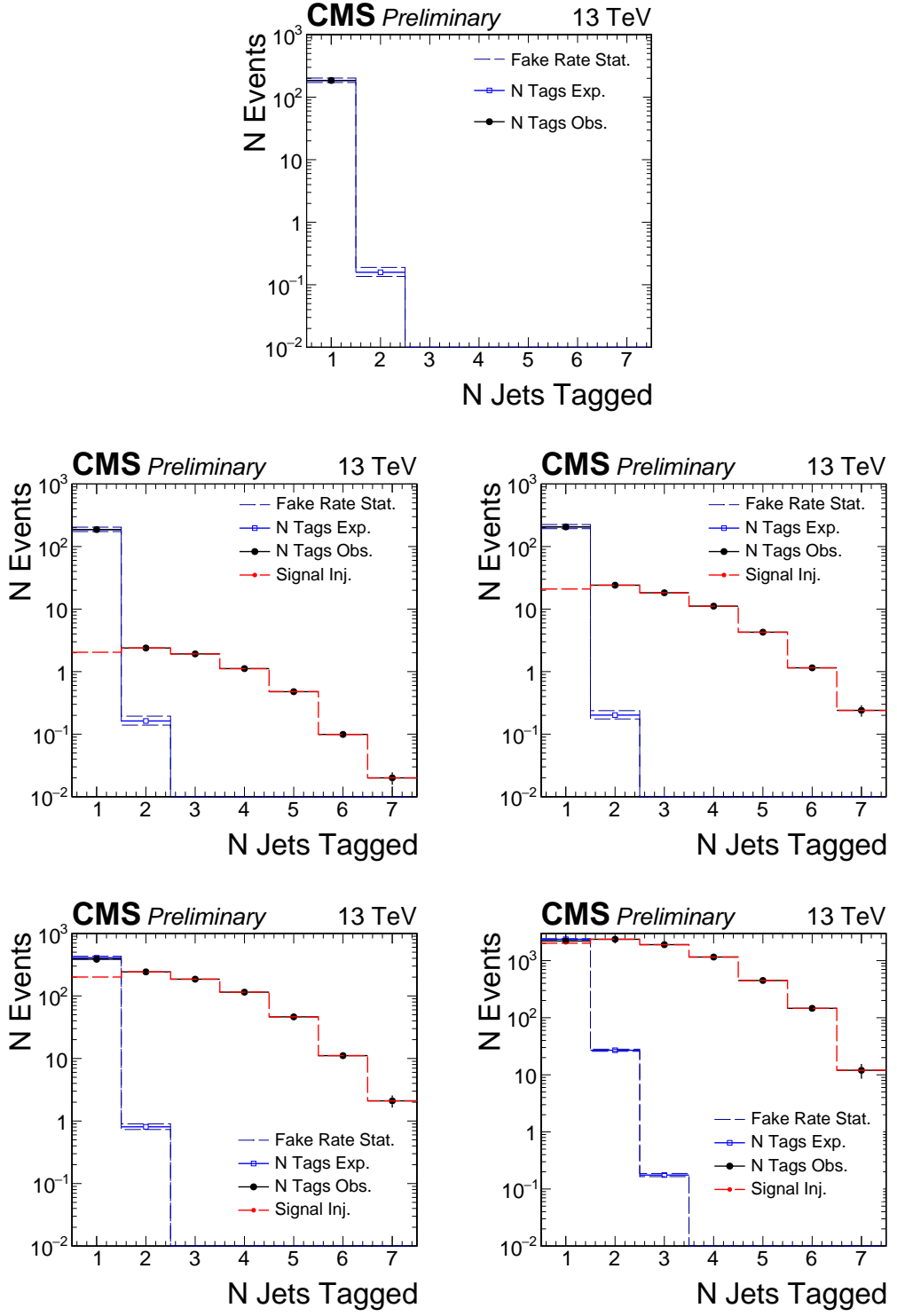


Figure 7.5: Signal Injection tests. The Jet-Jet signal sample used has fixed $m_X = 700\text{GeV}$ and $c\tau_0 = 10 \text{ mm}$. The level of signal contamination is progressively varied between 10, 100, 1000, and 10000 events injected before any selection. The full event selection is applied and the baseline jet tag definition.

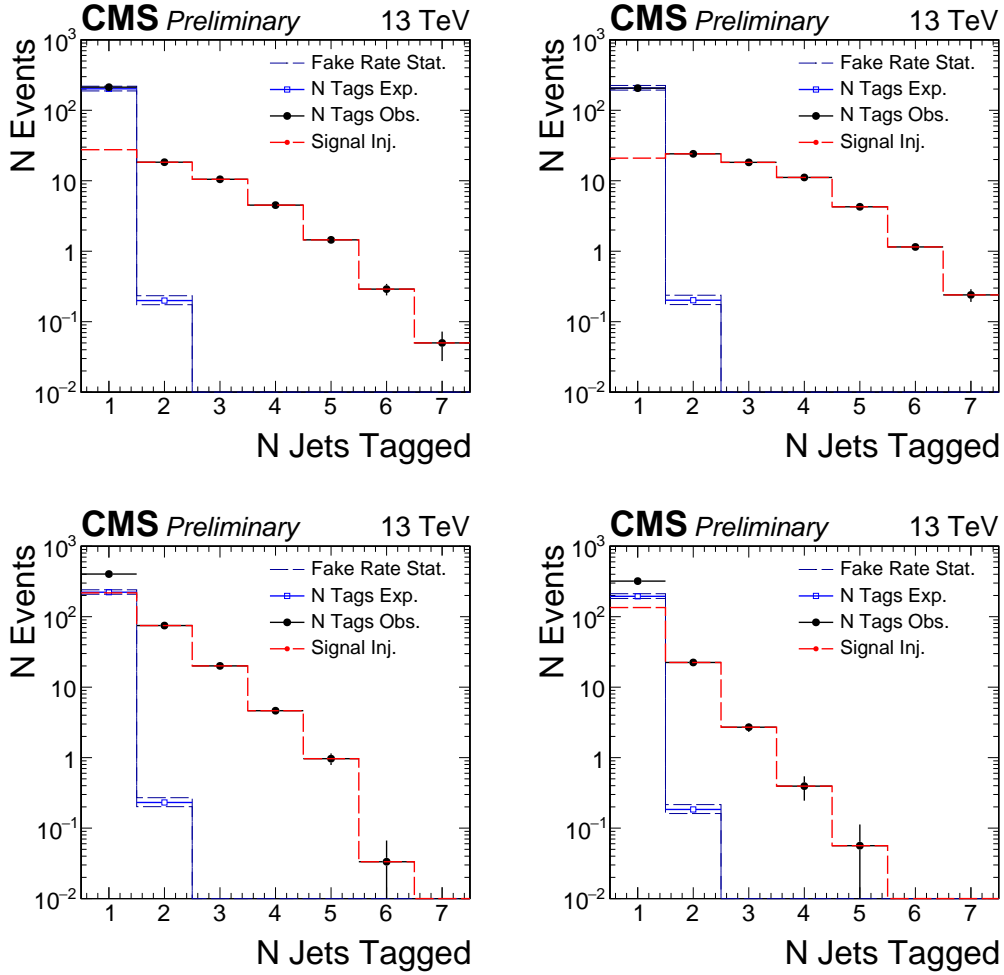


Figure 7.6: Signal Injection. The Jet-Jet signal sample is varied $m_X = 700 \text{ GeV}$ and $c\tau_0 = 1000 \text{ mm}$ (top left) $m_X = 700 \text{ GeV}$ and $c\tau_0 = 10 \text{ mm}$ (top right) $m_X = 100 \text{ GeV}$ and $c\tau_0 = 1000 \text{ mm}$ (bottom left) $m_X = 100 \text{ GeV}$ and $c\tau_0 = 10 \text{ mm}$ (bottom right). The level of signal contamination is fixed at 100 events for the $m_X = 700 \text{ GeV}$ and 1000 events for $m_X = 100 \text{ GeV}$. The full event selection is applied and the baseline jet tag definition.

Table 7.9 and Table 7.10. The goal of this exercise is to understand the quantity of signal contamination, as well as lifetime and mass, required to significantly alter the background prediction.

The resulting predictions are also reported normalized such that the total signal + qcd events passing the event selection are equal to the number of events passing the event selection in the analysis in Table 7.11.

The change in the N_{tags}^{obs} distribution to the presence of signal is on the order of the number of events with $N_{tags} > 2$ whereas the integrated shift in $P(N_{tags} \geq 2)$ is on the order of the shift induced in the $p(j)$ distribution. This shift is of the order the signal contamination. We can conclude the analysis will retain relative sensitivity as long as the signal contamination is relatively smaller than the QCD contribution in the fake rate calculation.

In summary, the background prediction is robust to a variety signal masses, lifetimes and sizes of contamination. Robust in the sense that the background is correctly determined within error in the 0 injection case and the bias to the background prediction due to the contamination is small relative to the number of signal events injected.

The following section explores the sensitivity to signal explicitly in a simplified scenario given the assumption that the jet probabilities accurately predict the background in the scenario where there are no signal events present. This assumption is based on the closure studies in the previous section and be considered true within some closure systematic.

Explicit Sensitivity in A Simplified Injection Scenario

Consider a sample of N_{QCD} QCD events with a known fraction of jets that are tagged $f(j_i)$ as a function of some jet parameters j_i . For simplicity, assume events have exactly 2 jets. Also assume we have shown that the observation approximately deter-

mined $N_{obs}^{2tag} = N_{pred}^{2tag}$ when we interpret $f(j_i)$ as a conditional probability $p(j_i)$ such that:

$$N_{obs}^{2tag} = N_{pred}^{2tag} = \sum_i [p(j_1)p(j_2)]_i = N_{QCD}p^2$$

where we are using a flat probability p such that $p(j_1) = p(j_2) = p = n_{tag}/n_{jets} = n_{fake}/2N_{events}$. Where n_{tag} is the number of jets tagged, which in a QCD sample is exactly n_{fake} . Now, say we perform the signal injection test by injecting N_{sig} events with correspondingly $2N_{sig}$ signal jets. Let ϵ be the efficiency for a signal event to have 1 tag. Accordingly the probability will shift $p(j_i) \rightarrow \tilde{p}(j_i)$:

$$\tilde{p} = \frac{n_{fake} + n_{true-tags}}{2N_{QCD} + 2N_{sig}} = \frac{n_{fake} + \epsilon 2N_{sig}}{2N_{QCD} + 2N_{sig}}$$

Taylor expanding in N_{sig} about 0 we obtain:

$$\begin{aligned} \tilde{p} &= \frac{n_{fake}}{2N_{QCD}} - \frac{N_{sig}n_{fake}}{2(N_{QCD})^2} + \epsilon \frac{2N_{sig}N_{QCD}}{2(N_{QCD})^2} \\ &= p - p \frac{N_{sig}}{N_{QCD}} + \frac{N_{sig}\epsilon}{N_{QCD}} \end{aligned}$$

Let $\Delta = N_{sig}/N_{QCD}$

$$\tilde{p} = p(1 - \Delta) + \Delta\epsilon$$

Note that as the signal contamination $\Delta \rightarrow 0$, we obtain the correct probability $\tilde{p} = p$. Now we attempt to predict the number of events with 2 tags using \tilde{p} and splitting

the sum over signal and QCD events.

$$\begin{aligned}
N_{pred}^{2tag} &= \sum_i \tilde{p}\tilde{p} \\
&= \sum_i (p(1 - \Delta) + \Delta\epsilon)^2 \\
&= \sum_i p^2 - p^2(2\Delta) + p^2\Delta^2 + 2p\Delta\epsilon - 2p\Delta^2\epsilon + \Delta^2\epsilon^2
\end{aligned}$$

We now split the events in the sum between QCD and Signal.

$$\begin{aligned}
N_{pred}^{2tag} &= \sum_i (QCD) + \sum_i (Signal) \\
\sum_i (QCD) &= N_{QCD}(p^2 - p^2(2\Delta) + p^2\Delta^2 + 2p\Delta\epsilon - 2p\Delta^2\epsilon + \Delta^2\epsilon^2) \\
&= N_{obs}^{QCD} - N_{sig}(p^2\Delta + \Delta\epsilon^2 - 2p^2 + 2p\epsilon - 2p\Delta\epsilon)
\end{aligned}$$

where we have used the fact that $\Delta N_{QCD} = N_{sig}$ and $\sum_i p^2 = N_{obs}^{QCD}$:

$$\sum_i (Signal) = N_{sig}(p^2 - p^2(2\Delta) + p^2\Delta^2 + 2p\Delta\epsilon - 2p\Delta^2\epsilon + \Delta^2\epsilon^2)$$

We now evaluate our sensitivity to signal or equivalently the disagreement between observed and prediction by the variable S . Let $N_{obs}^{2tag} = N_{obs}^{sig} + N_{obs}^{QCD}$. The sensitivity S , is a measure of how well we have predicted the background in the presence of signal. When $S = 1$ the prediction is exactly the background and the excess is exactly the number of signal events. When $S = 0$ the probabilities prediction has over estimated the background entirely resulting in no disagreement between observed and predicted

2 tag events.

$$\begin{aligned}
S = \frac{N_{obs}^{2tag} - N_{pred}^{2tag}}{N_{sig}} &= 1 - (2p\epsilon + \Delta\epsilon^2) \\
&\quad - (p^2 + \Delta^2\epsilon^2 + 2p\Delta\epsilon - 2p^2 - 2p\Delta\epsilon) \\
&\quad - (p^2\Delta - 2p^2\Delta - 2p\Delta^2\epsilon) \\
&\quad - (p^2\Delta^2)
\end{aligned}$$

where we have grouped terms by their order in $O(\Delta) + O(p)$. Consider the case when $\epsilon \approx 1$ (this is an approximation for readability as $\epsilon = 1$ would imply no 2 tag events) and for simplicity say $\Delta = p = x$.

$$S = 1 - 3x + 3x^3 - x^4$$

If we plug in the baseline fake rate for x then $S(x = 5 \times 10^{-4}) = 0.999$.

7.6.2 Tag Probability Cross Validation

To test the bias of the background estimation a method of cross validation is utilized. For a given sample, N_{div} non-overlapping sub-samples are partitioned. For each sub-sample, a corresponding set of jet probabilities are computed as described in the previous section. For each set of jet probabilities, an N_{tag}^{pred} prediction is made for the $N_{div} - 1$ remaining samples (which have no overlapping events). We will refer to the sample used for the prediction as the measurement sample. The result is $N_{div}(N_{div} - 1)$ pairs of probabilities and measurement samples. From each pair, in each bin of N_{tags} , we generate a distribution of pulls $(N_{obs} - N_{pred})/\sqrt{N_{pred}}$ for each N_{tag} bin. All events must pass the event selection.

Due to limited statistics in the 2 tag bin for the baseline tag, the loose tag definition (Table 7.2) is used to generate pull distributions in the 2 tag bin.

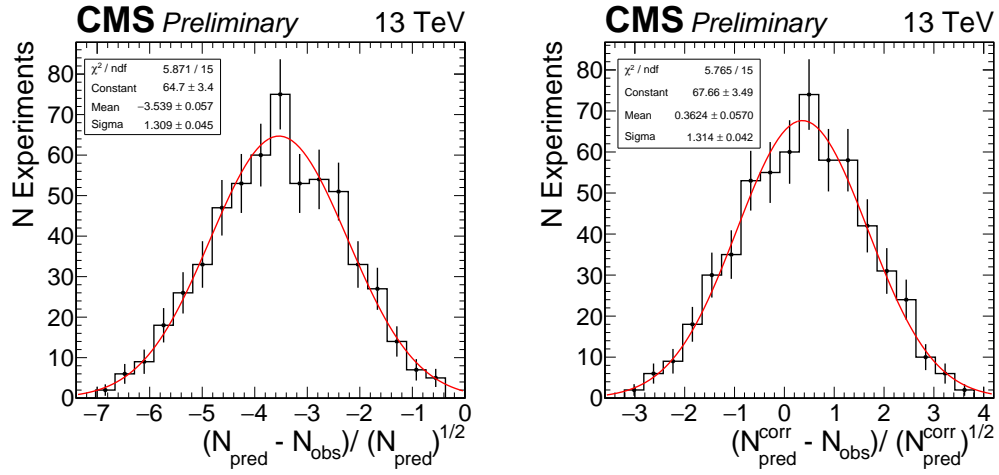


Figure 7.7: Cross validation of the predicted of the number of loose tags in data collected by the displaced jet triggers. Pulls for the 1 tag bin with the loose tag (left). Pulls for the 1 tag bin with the loose tag with the SR correction (Right).

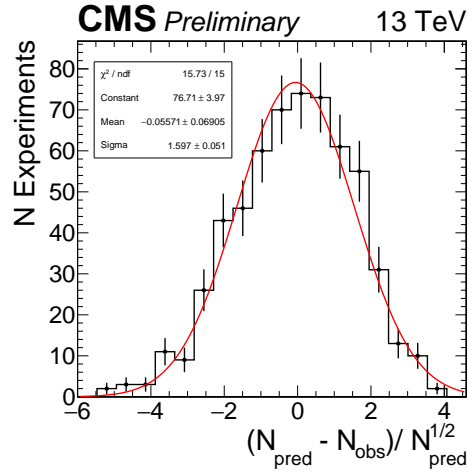


Figure 7.8: Cross validation of the predicted of the number of tags in data passing the displaced jet triggers. Pulls for the 1 tag bin with the baseline tag after the application of the signal removal correction $2r_{12} = .2\%$

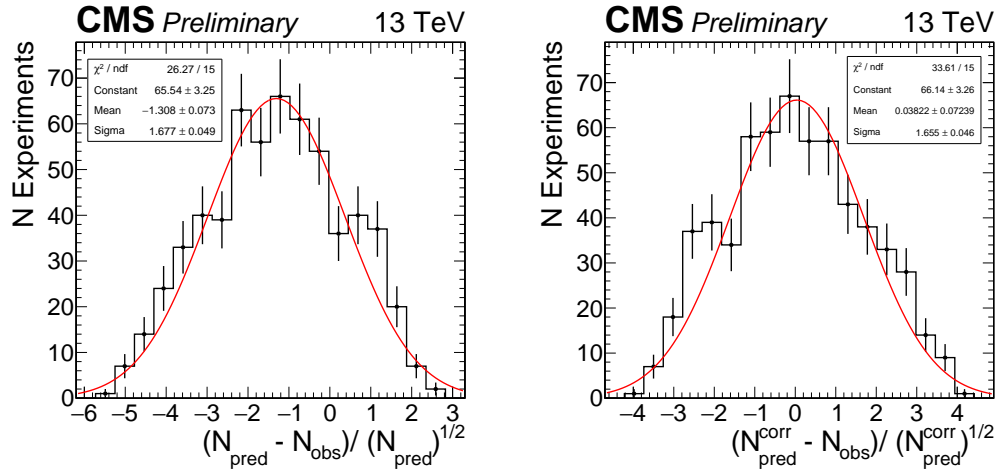


Figure 7.9: Cross validation of the predicted of the number of loose tags in QCD events passing the displaced jet triggers. Pulls for the 1 tag bin with the loose tag (left). The signal region removal corrected pulls (Right).

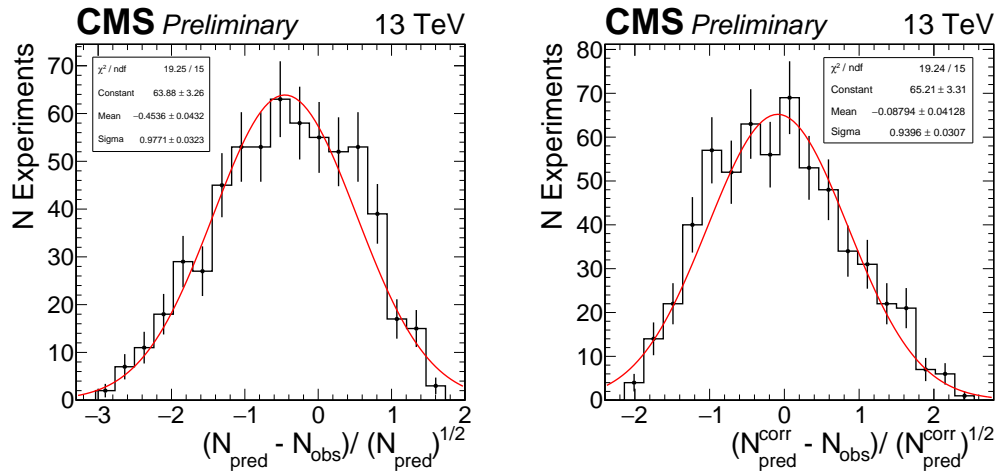


Figure 7.10: Cross validation of the predicted of the number of loose tag in QCD events passing the displaced jet triggers. Pulls for the 2 tag bin with the loose tag uncorrected (left). The same prediction corrected for the SR removal (right)

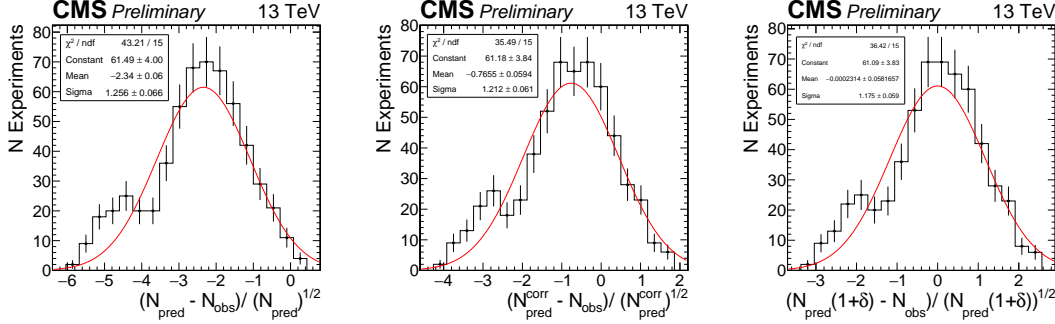


Figure 7.11: Cross validation of the predicted of the number of baseline tags in data collected by the displaced jet triggers. Pulls for the 2 tag bin with the loose tag (left). Pulls with the signal region removal correction applied (middle). The same signal region removal correction shifted by $\delta = 7.5\%$ (Right).

We summarize the cross validation studies in the following figures:

- Fig 7.7: SR corrected and uncorrected 1 tag bin pulls for the Loose tag definition in Data collected by Displaced Jet Triggers. $N_{div} = 25$
- Fig 7.8: SR corrected 1 tag bin pulls for the Baseline tag definition in Data collected by Displaced Jet Triggers. $N_{div} = 25$
- Fig 7.9: 1 tag bin pulls for the Loose tag definition in QCD events passing the Displaced Jet Triggers. $N_{div} = 25$
- Fig 7.10: 2 tag bin pulls for the Loose tag definition in QCD events passing by Displaced Jet Triggers. $N_{div} = 25$
- Fig 7.11: SR corrected, uncorrected, and SR corrected+ δ 2 tag bin pulls for the Loose tag definition in Data collected by Displaced Jet Triggers. $N_{div} = 25$

In data and QCD, the SR correction provides a significant improvement on the pull distributions with respect to the ideal parameters $\mu = 0$ and $\sigma = 1.0$. For the 1 tag prediction in data with the loose tag the central value changes from $\mu = 3.5$ (uncorrected) to $\mu = 0.36$ (corrected). For the signal region (2+ tags), the loose tag

in data is within 7.5% of ideal μ and the QCD estimate is within error of $\mu = 0$ but has $\sigma = 1.6 > 1.0$.

7.7 Systematic uncertainties

7.7.1 Background systematic uncertainties

A background systematic uncertainty is quoted for the data-driven background prediction method. This uncertainty is estimated by repeating the background-prediction procedure on data with a looser version of the displaced-jet tagging algorithm as outlined in section 7.6. The background estimation uncertainty of 7.5% is the required adjustment to the prediction to remove the bias observed in the Gaussian fit. For three or more tags, the systematic uncertainty for the method is kept fixed.

The statistical uncertainty on the measured misidentification rate as a function of N_{tracks} is propagated to the predicted N_{tags} distribution as a systematic uncertainty. This systematic uncertainty is calculated for each tag multiplicity bin individually. The uncertainty for the 2 tag bin is $-12/+13\%$.

In summary, for the background prediction in the two tag bin, a 7.5% uncertainty is assigned to the background prediction method and $-12/+13\%$ uncertainty is assigned to the statistics of the misidentification rate.

7.7.2 Signal systematic uncertainties

A summary of the systematic uncertainties associated with the signal yields is given in Table 7.12. The uncertainty on the trigger emulation is measured by comparing the predicted efficiency for simulated multijet events and data collected by a loose H_T trigger. The observed difference at threshold (5%) is taken as an estimate of the uncertainty in the emulation of the online H_T requirement. Similarly, the uncertainty induced by the online versus offline jet acceptance is obtained from the shift in the

trigger efficiency when the offline jet p_t requirement is increased from $p_t > 60$ GeV to $p_t > 80$ GeV (5%).

The systematic uncertainty on the luminosity is 2.7% [10].

The uncertainty arising from the PDFs for pair-produced masses in the range of 50–1500GeV is found to be 1–6% Figure 7.12. An ensemble of alternative PDF is sampled from the output of the NNPDF fit. Events are reweighted according to the ratio between these alternative PDF sets and the nominal ones. The distribution of the signal prediction for these PDF ensemble is used to quantify the uncertainty.

The systematic uncertainty on the modeling of the jet tagging variables in signal MC samples is estimated from the displaced track modeling in multi-jet events in data and MC. The mismodeling of the measured value of Θ_{2D} and IP_{sig}^{2D} for single tracks is propagated to the final tag distribution by varying the individual measured values in MC by the difference in the measured value relative to data (3–10%). The tagging variables are then re-calculated. The N_{tags} distribution is recalculated with the new values. The systematic uncertainty is assigned as the relative change in events, bin by bin in N_{tags} . For the two tag bin, this varies from 1 to 30% depending on the mass and lifetime Figure 7.16. The mismodeling of α_{\max} is found to have a negligible effect on the signal efficiency as the requirement is relatively loose.

The systematic uncertainty on the modeling of the online tracking efficiency is obtained by studying the online regional track reconstruction in data and MC. The online values of IP^{2D} and IP_{sig}^{2D} are varied by the magnitude of the mismodeling found in events collected in control triggers. The new values are used to determine if the event would still pass at least one of the trigger paths and its associated offline H_T requirement. The N_{tags} distribution is recalculated with the values varied up and down. The relative change in the number of events per bin is taken as the systematic uncertainty. For the two tag bin, this uncertainty varies from 1 to 35%.

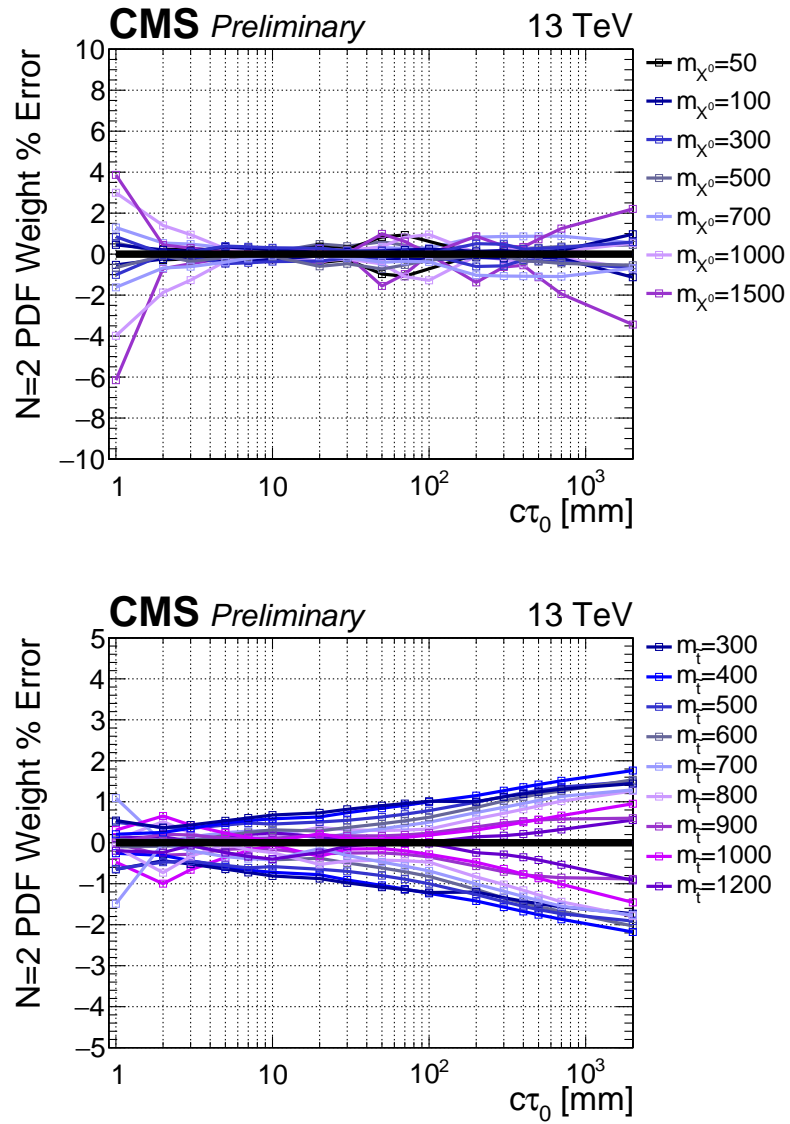


Figure 7.12: The PDF acceptance systematics in the Jet-Jet (left) and B-Lepton (right) signal model as a function of the mass m_X or $c\tau_0$ for the 2 tag bin. The systematic is reported two sided for the two tag bin in the analysis. The error to fluctuate up is in the upper half plane and the error to fluctuate down on the lower half plane.

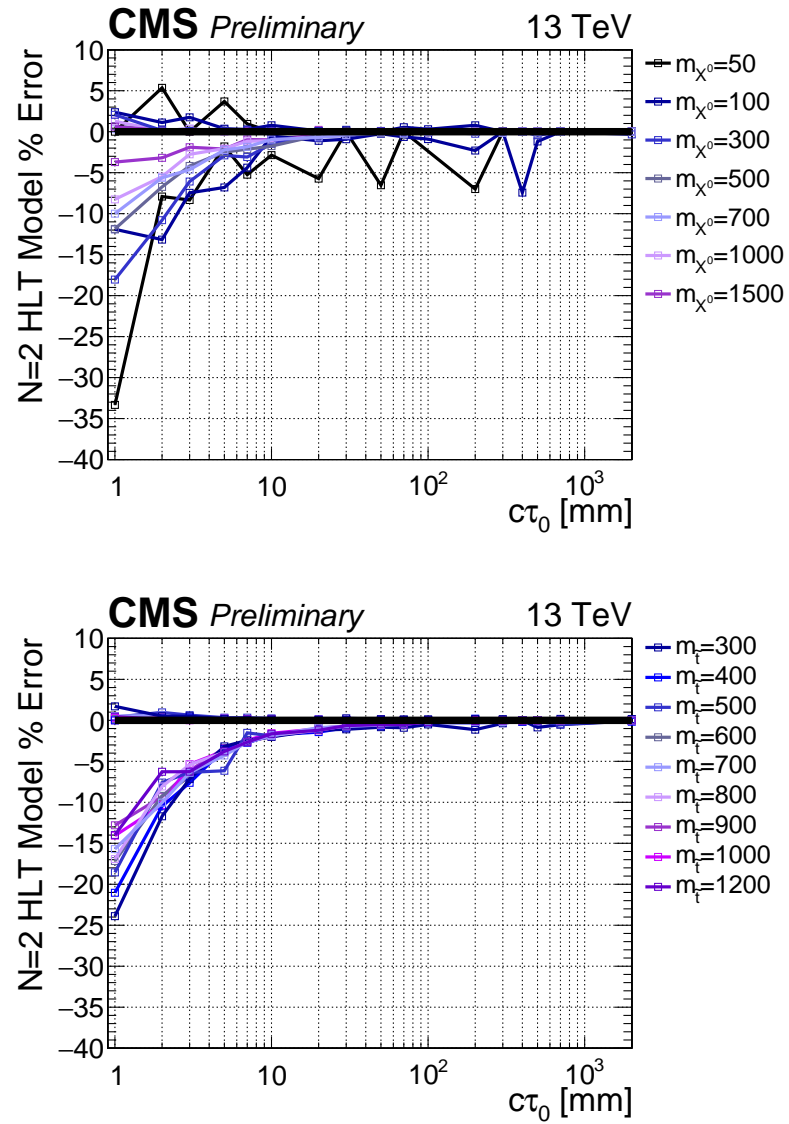


Figure 7.13: The onling tracking related systematics in the Jet-jet (top) and B-Lepton (bottom) model as a function of $c\tau_0$. (Top) The online track 2DIP and $2DIP_{sig}$ modeling in the 2 tag bin

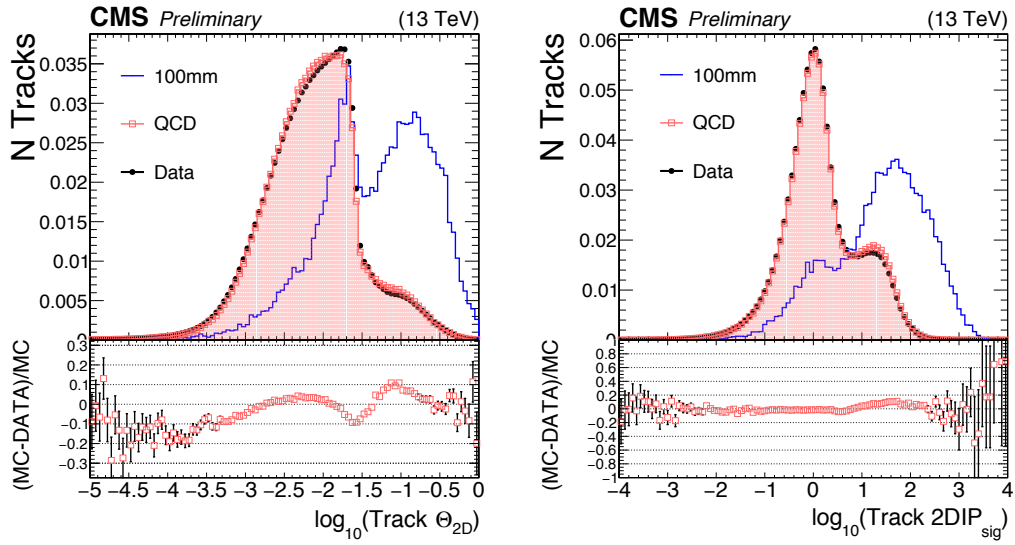


Figure 7.14: Comparison of the offline θ and 2DIP_{sig} for individual tracks associated to jets passing $p_T > 60$ GeV and $|\eta| < 2.0$ as collected by HLT-HT425.

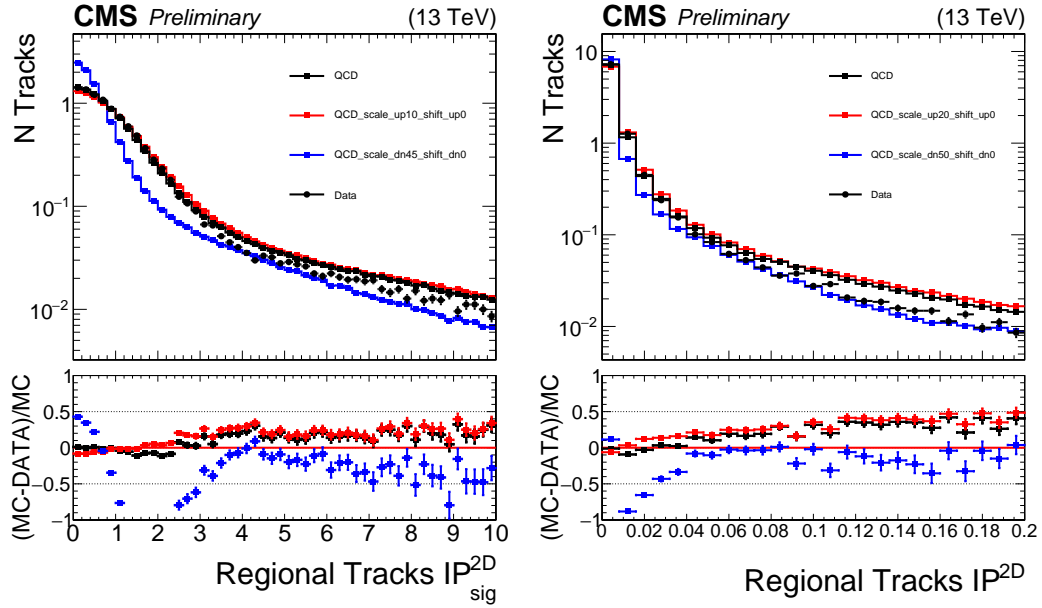


Figure 7.15: Comparison of the online 2DIP and 2DIP_{sig} for individual tracks associated to jets passing $p_T > 60$ GeV and $|\eta| < 2.0$ as collected by HLT-HT425. For each variable x the value is scaled as $x(1 \pm \Delta)$ with positive in red and the negative in blue. A re-scaling of $+10/-45$ and $+20/-50$ for 2DIP_{sig} and 2DIP respectively provide an envelope for the DATA/MC differences

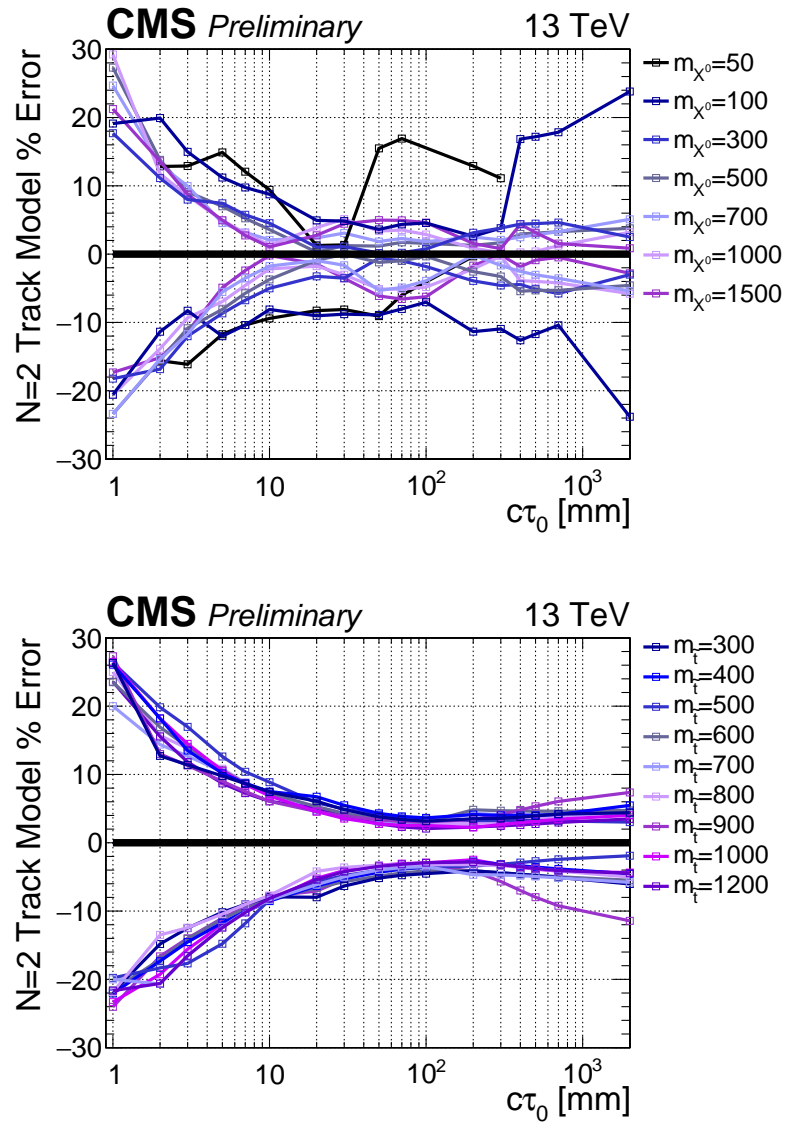


Figure 7.16: The two tracking related systematics in the Jet-Jet (top) and B-Lepton (bottom) model as a function of $c\tau_0$. The displaced jet tagging variable systematic in the 2 tag bin. The systematic is reported two sided for the two tag bin in the analysis. The error to fluctuate up is in the upper half plane and the error to fluctuate down on the lower half plane.

All signal systematic uncertainties are calculated individually for each model for all individual mass and lifetime points, and for each value of N_{tags} in the signal region.

7.8 Results and interpretation

The numerical values for the expected and observed yields are summarized in Table 7.13. The observed yields are found to be consistent with the predicted background, within the statistical and systematic uncertainties. No evidence for a signal at large values of N_{tags} is observed.

Exclusions for each model are obtained from the predicted and observed event yields in Table 7.13 and the signal efficiencies in Tables 7.7–7.8. All bounds are derived at 95% confidence-level (CL) according to the CL_s prescription [11, 12, 13] in the asymptotic approximation. For each limit derivation, we consider events with $N_{\text{tags}} \geq 2$ using independent bins for $N_{\text{tags}} = 2$ and $N_{\text{tags}} \geq 3$. Finer binning of the tag multiplicity for $N_{\text{tags}} > 3$ is found to have a negligible affect on the expected limits. Cross section upper limits are presented as a function of the mass and lifetime of the parent particle. The analysis sensitivity is maximal for $(10 < c\tau_0 < 1000)\text{mm}$. Mass exclusion bounds at fixed lifetime are also derived, comparing the excluded cross section with the values predicted for the benchmark models described in section 7.5. In the case of SUSY models, the next-to-leading order (NLO) and next-to-leading-logs (NLL) $t\bar{t}$ production cross section is used as reference, computed in the large-mass limit for all the other SUSY particles [14, 15, 16, 17, 18, 19].

Figures 7.17 and 7.18 show the excluded pair-production cross section for the Jet-Jet and Light-Light models, respectively. Cross sections as small as 1.2 fb are excluded for $c\tau_0 = 50\text{mm}$ for both models. Exclusion limits are also derived for resonances decaying to $b\ell$ final states, as shown in Fig. 7.19. The sensitivity is similar to what is observed for the Jet-Jet model, although less stringent as additional jets

give higher efficiency than additional leptons from both the tagging and triggering perspectives. Cross sections larger than 2.47 fb are excluded at 95% CL, for $c\tau_0$ in the range 70–100 mm excluding a parent mass value of 1135 GeV.

Figures 7.20 and 7.21 show the exclusions on the B-Tau and B-Ele models, respectively. The two models have similar performance at high mass with slightly stronger limits for the B-Ele model at lower mass $m_{\tilde{t}} = 300$ GeV and lifetimes $c\tau_0 > 10$ mm. The highest mass excluded in the B-Ele (B-Tau) model occurs at $m_{\tilde{t}} = 1150$ (1155)GeV and $c\tau_0 = 70$ (70)mm at an observed cross section upper limit of 2.25 (2.17) fb at 95% CL.

In contrast, Fig. 7.22 shows the exclusion for the B-Mu model. Since the analysis uses jets reconstructed from calorimetric deposits while the two muons have small or no associated calorimeter deposit, the signal reconstruction efficiency and displaced-jet multiplicity are smaller in this case. This results in a weaker exclusion bound. The highest mass excluded in the B-Mu model occurs at $m_{\tilde{t}} = 1090$ GeV and $c\tau_0 = 70$ mm at an observed cross section upper limit of 3.36 fb at 95% CL.

Table 7.6: Signal efficiency for fixed $m_X = m_{\tilde{t}} = 300$ GeV and varied $c\tau_0$ with modified branching ratios relative to the Jet-Jet and B-Lepton models. Selection requirements are cumulative from the first to the last row.

Light-Light				
m_X [GeV]	300	300	300	300
$c\tau_0$ [mm]	1	10	100	1000
≥ 2 tags	$2.20 \pm 0.19\%$	$40.49 \pm 0.80\%$	$54.92 \pm 0.93\%$	$14.55 \pm 0.47\%$
Trigger	$2.04 \pm 0.18\%$	$39.16 \pm 0.78\%$	$39.63 \pm 0.79\%$	$8.20 \pm 0.36\%$
Event sel.	$2.03 \pm 0.18\%$	$38.41 \pm 0.77\%$	$36.99 \pm 0.76\%$	$6.89 \pm 0.33\%$
≥ 3 tags	$0.187 \pm 0.054\%$	$14.77 \pm 0.48\%$	$16.70 \pm 0.51\%$	$1.48 \pm 0.15\%$
≥ 4 tags	–	$5.11 \pm 0.28\%$	$4.73 \pm 0.27\%$	$0.216 \pm 0.058\%$
B-Ele				
$m_{\tilde{t}}$ [GeV]	300	300	300	300
$c\tau_0$ [mm]	1	10	100	1000
≥ 2 tags	$0.807 \pm 0.093\%$	$20.51 \pm 0.47\%$	$39.01 \pm 0.65\%$	$11.46 \pm 0.35\%$
Trigger	$0.398 \pm 0.065\%$	$14.68 \pm 0.40\%$	$22.95 \pm 0.50\%$	$5.15 \pm 0.23\%$
Event sel.	$0.398 \pm 0.065\%$	$13.92 \pm 0.39\%$	$20.34 \pm 0.47\%$	$3.58 \pm 0.19\%$
≥ 3 tags	$0.043 \pm 0.022\%$	$4.22 \pm 0.21\%$	$7.21 \pm 0.28\%$	$0.822 \pm 0.093\%$
≥ 4 tags	–	$0.727 \pm 0.088\%$	$1.19 \pm 0.11\%$	$0.053 \pm 0.024\%$
B-Tau				
$m_{\tilde{t}}$ [GeV]	300	300	300	300
$c\tau_0$ [mm]	1	10	100	1000
≥ 2 tags	$0.483 \pm 0.073\%$	$18.40 \pm 0.45\%$	$34.98 \pm 0.61\%$	$9.31 \pm 0.32\%$
Trigger	$0.439 \pm 0.069\%$	$14.63 \pm 0.40\%$	$20.20 \pm 0.46\%$	$3.81 \pm 0.20\%$
Event sel.	$0.406 \pm 0.067\%$	$12.45 \pm 0.37\%$	$15.50 \pm 0.41\%$	$2.37 \pm 0.16\%$
≥ 3 tags	$0.022 \pm 0.016\%$	$3.23 \pm 0.19\%$	$4.62 \pm 0.22\%$	$0.441 \pm 0.069\%$
≥ 4 tags	–	$0.525 \pm 0.076\%$	$0.660 \pm 0.084\%$	$0.022 \pm 0.015\%$
B-Mu				
$m_{\tilde{t}}$ [GeV]	300	300	300	300
$c\tau_0$ [mm]	1	10	100	1000
≥ 2 tags	$0.130 \pm 0.037\%$	$8.02 \pm 0.29\%$	$20.09 \pm 0.46\%$	$4.03 \pm 0.21\%$
Trigger	$0.054 \pm 0.024\%$	$3.97 \pm 0.21\%$	$6.63 \pm 0.26\%$	$0.881 \pm 0.098\%$
Event sel.	$0.043 \pm 0.022\%$	$2.92 \pm 0.18\%$	$4.21 \pm 0.21\%$	$0.489 \pm 0.073\%$
≥ 3 tags	–	$0.227 \pm 0.049\%$	$0.307 \pm 0.057\%$	$0.033 \pm 0.019\%$
≥ 4 tags	–	$0.011 \pm 0.011\%$	–	–

Table 7.7: Signal efficiencies for the Jet-Jet and B-Lepton models with $c\tau_0 = 30\text{mm}$ and varied mass. Selection requirements are cumulative from the first to the last row.

Jet-Jet				
m_X [GeV]	50	100	300	1000
$c\tau_0$ [mm]	30	30	30	30
≥ 2 tags	$2.710 \pm 0.095\%$	$14.80 \pm 0.22\%$	$54.24 \pm 0.74\%$	$79.93 \pm 0.89\%$
Trigger	$0.503 \pm 0.041\%$	$5.39 \pm 0.13\%$	$46.41 \pm 0.68\%$	$74.05 \pm 0.86\%$
Event sel.	$0.297 \pm 0.031\%$	$3.70 \pm 0.11\%$	$44.75 \pm 0.67\%$	$73.99 \pm 0.86\%$
≥ 3 tags	$0.050 \pm 0.013\%$	$1.087 \pm 0.060\%$	$20.87 \pm 0.46\%$	$49.42 \pm 0.70\%$
≥ 4 tags	–	$0.217 \pm 0.027\%$	$6.81 \pm 0.26\%$	$25.45 \pm 0.50\%$

B-Lepton				
$m_{\tilde{t}}$ [GeV]	300	600	800	1000
$c\tau_0$ [mm]	30	30	30	30
≥ 2 tags	$31.52 \pm 0.19\%$	$47.32 \pm 0.23\%$	$52.53 \pm 0.24\%$	$55.88 \pm 0.35\%$
Trigger	$17.08 \pm 0.14\%$	$35.03 \pm 0.20\%$	$40.40 \pm 0.21\%$	$43.14 \pm 0.30\%$
Event sel.	$14.70 \pm 0.13\%$	$32.34 \pm 0.19\%$	$36.94 \pm 0.20\%$	$39.26 \pm 0.29\%$
≥ 3 tags	$4.106 \pm 0.068\%$	$10.76 \pm 0.11\%$	$13.29 \pm 0.12\%$	$15.00 \pm 0.18\%$
≥ 4 tags	$0.552 \pm 0.025\%$	$1.828 \pm 0.045\%$	$2.687 \pm 0.055\%$	$3.092 \pm 0.082\%$

Table 7.8: Signal efficiency for fixed $c\tau_0 = 30$ mm and varied mass with modified branching ratios relative to the Jet-Jet and B-Lepton models. Selection requirements are cumulative from the first to the last row.

Light-Light					
m_X [GeV]	50	100	300	1000	
$c\tau_0$ [mm]	30	30	30	30	
≥ 2 tags	$2.84 \pm 0.12\%$	$15.56 \pm 0.29\%$	$54.87 \pm 0.92\%$	$80.52 \pm 1.11\%$	
Trigger	$0.530 \pm 0.052\%$	$5.70 \pm 0.17\%$	$47.14 \pm 0.85\%$	$74.85 \pm 1.07\%$	
Event sel.	$0.327 \pm 0.041\%$	$3.90 \pm 0.14\%$	$45.68 \pm 0.84\%$	$74.80 \pm 1.07\%$	
≥ 3 tags	$0.052 \pm 0.016\%$	$1.113 \pm 0.076\%$	$21.77 \pm 0.58\%$	$50.04 \pm 0.88\%$	
≥ 4 tags	–	$0.230 \pm 0.035\%$	$7.38 \pm 0.34\%$	$25.80 \pm 0.63\%$	
B-Ele					
$m_{\tilde{t}}$ [GeV]	300	600	800	1000	
$c\tau_0$ [mm]	30	30	30	30	
≥ 2 tags	$39.01 \pm 0.65\%$	$53.70 \pm 0.75\%$	$59.62 \pm 0.78\%$	$62.42 \pm 1.11\%$	
Trigger	$22.95 \pm 0.50\%$	$38.07 \pm 0.63\%$	$43.06 \pm 0.66\%$	$45.21 \pm 0.95\%$	
Event sel.	$21.59 \pm 0.48\%$	$37.02 \pm 0.62\%$	$39.47 \pm 0.64\%$	$42.20 \pm 0.92\%$	
≥ 3 tags	$7.86 \pm 0.29\%$	$14.28 \pm 0.38\%$	$17.37 \pm 0.42\%$	$20.39 \pm 0.64\%$	
≥ 4 tags	$1.37 \pm 0.12\%$	$3.32 \pm 0.19\%$	$4.34 \pm 0.21\%$	$4.69 \pm 0.31\%$	
B-Tau					
$m_{\tilde{t}}$ [GeV]	300	600	800	1000	
$c\tau_0$ [mm]	30	30	30	30	
≥ 2 tags	$34.98 \pm 0.61\%$	$51.42 \pm 0.73\%$	$57.20 \pm 0.76\%$	$59.43 \pm 1.07\%$	
Trigger	$20.20 \pm 0.46\%$	$39.78 \pm 0.64\%$	$45.46 \pm 0.68\%$	$47.62 \pm 0.96\%$	
Event sel.	$17.17 \pm 0.43\%$	$37.47 \pm 0.62\%$	$43.64 \pm 0.67\%$	$44.26 \pm 0.92\%$	
≥ 3 tags	$5.21 \pm 0.24\%$	$13.29 \pm 0.37\%$	$16.15 \pm 0.40\%$	$19.13 \pm 0.61\%$	
≥ 4 tags	$0.86 \pm 0.10\%$	$3.09 \pm 0.18\%$	$3.68 \pm 0.19\%$	$4.48 \pm 0.29\%$	
B-Mu					
$m_{\tilde{t}}$ [GeV]	300	600	800	1000	
$c\tau_0$ [mm]	30	30	30	30	
≥ 2 tags	$20.09 \pm 0.46\%$	$35.46 \pm 0.60\%$	$41.18 \pm 0.64\%$	$43.13 \pm 0.93\%$	
Trigger	$6.63 \pm 0.26\%$	$24.73 \pm 0.50\%$	$31.85 \pm 0.56\%$	$34.10 \pm 0.82\%$	
Event sel.	$5.25 \pm 0.24\%$	$21.40 \pm 0.47\%$	$27.42 \pm 0.52\%$	$31.18 \pm 0.79\%$	
≥ 3 tags	$0.344 \pm 0.060\%$	$3.03 \pm 0.18\%$	$5.28 \pm 0.23\%$	$6.08 \pm 0.35\%$	
≥ 4 tags	–	$0.122 \pm 0.035\%$	$0.677 \pm 0.082\%$	$0.68 \pm 0.12\%$	

Table 7.9: The signal injection test using a fixed signal point $m_X = 700$ GeV and $c\tau_0 = 10$ mm with varied amount of injection. A summary of the 1,2,3, and 4 tag predictions as a function of the number of events injected (top). The two background systematic errors are listed separately as σ_{method} , $\sigma_{fake-rate}$. A summary of the observed number of tags (bottom).

Injection $\sigma \times \mathcal{L}$	1 Pred	2 Pred	3 Pred	4 Pred
0	$185^{+14,+17}_{-14,-13}$	$0.16^{+0.01,+0.03}_{-0.01,-0.02}$	—	—
10	$187^{+14,+17}_{-14,-13}$	$0.16^{+0.01,+0.03}_{-0.01,-0.02}$	—	—
100	$207^{+16,+18}_{-16,-14}$	$0.20^{+0.02,+0.04}_{-0.02,-0.03}$	—	—
1000	$408^{+31,+23}_{-31,-19}$	$0.81^{+0.06,+0.09}_{-0.06,-0.08}$	—	—
10000	$2366^{+177,+53}_{-177,-49}$	$26.95^{+2.02,+1.19}_{-2.02,-1.10}$	$0.18^{+0.01,+0.01}_{-0.01,-0.01}$	—

Injection $\sigma \times \mathcal{L}$	1 Obs	2 Obs	3 Obs	4 Obs
0	185.00	0.00	0.00	0.00
10	186.94	2.40	1.99	1.20
100	205.14	23.05	20.45	11.89
1000	386.10	237.20	188.40	116.80
10000	2260.00	2341.00	1976.00	1165.00

Table 7.10: Signal injection test with fixed number of injected events and varied $c\tau_0$ and m_X . A summary of the 1,2,3, and 4 tag predictions as a function of the number of events injected (top). The two background systematic errors are listed separately as σ_{method} , $\sigma_{fake-rate}$. A summary of the observed number of tags (bottom).

$\sigma \times \mathcal{L}$	m_X [GeV]	$c\tau_0$ [mm]	1 Pred	2 Pred	3+4 Pred
100	700	10	$207^{+16,+18}_{-16,-14}$	$0.20^{+0.02,+0.04}_{-0.02,-0.03}$	—
100	700	1000	$202^{+15,+18}_{-15,-14}$	$0.20^{+0.02,+0.03}_{-0.02,-0.03}$	—
1000	100	10	$222^{+17,+18}_{-17,-14}$	$0.23^{+0.02,+0.04}_{-0.02,-0.03}$	—
1000	100	1000	$195^{+15,+17}_{-15,-13}$	$0.18^{+0.01,+0.03}_{-0.01,-0.02}$	—

$\sigma \times \mathcal{L}$	Mass [GeV]	$c\tau_0$ [mm]	1 Obs	2 Obs	3+4 Obs
100	700	10	205.14	23.05	32.34
100	700	1000	211.56	17.98	12.36
1000	100	10	403.57	74.33	26.10
1000	100	1000	320.64	22.92	3.99

Table 7.11: A summary of the size of the signal injected in the signal injection test (top). A summary of signal region yields in the 2,3, and 4 nominal displaced jet tag bins (middle) and the observed number of tags (bottom), as a function of the size of the signal contamination, for a signal injection test using a fixed signal point $m_X = 700$ GeV and $c\tau_0 = 10$ mm with varied signal yields. The no signal case is included as a reference to the predicted values without contamination. The test is normalized such that the sum of signal and background events stays fixed at the observed number of events passing the analysis event selection. The contamination fraction corresponds to the hypothetical fraction of signal events contained within the events passing the event selection.

Contam. Fraction	Signal σ [fb]		
0	0		
0.01%	30		
0.10%	290		
1.04%	3000		
9.47%	28000		
Contamination %	2 tag pred	3 tag pred	4 tag pred
0	$1.34^{+0.25}_{-0.17}$	-	-
0.01%	$1.34^{+0.25}_{-0.17}$	-	-
0.10%	1.67 ± 0.33	-	-
1.04%	$6.71^{+0.91}_{-0.82}$	-	-
9.47%	205.38 ± 15.21	1.37 ± 0.08	-
Contamination %	2 tag obs	3 tag obs	4 tag obs
0.00%	0	0	0
0.01%	19	16	10
0.10%	179	159	93
1.04%	1914	1520	943
9.47%	17632	14883	8775

Table 7.12: Summary of the systematic uncertainties. When the uncertainty depends on the specific features of the models (mass, lifetime and decay mode of the long-lived particle) a range is quoted, which refers to the computed uncertainty for $N_{\text{tags}} = 2$ events.

Signal systematic uncertainty	Effect on yield
H_T trigger inefficiency	5.0%
Jet p_t trigger inefficiency	5.0%
Trigger online tracking modeling	1.0–35.0%
Luminosity	2.7%
Acceptance due to PDF	1.0–6.0%
Displaced-jet tag variable modeling	1.0–30.0%

Table 7.13: The predicted and observed number of events as a function of N_{tags} . The prediction is based on the mistagging probability derived from events with fewer than two tags. The full event selection is applied. The quoted uncertainty corresponds to the total background systematic uncertainty.

N_{tags}	Expected	Observed
2	$1.09^{+0.16}_{-0.15}$	1
≥ 3	$(4.9 \pm 1.0) \times 10^{-4}$	0

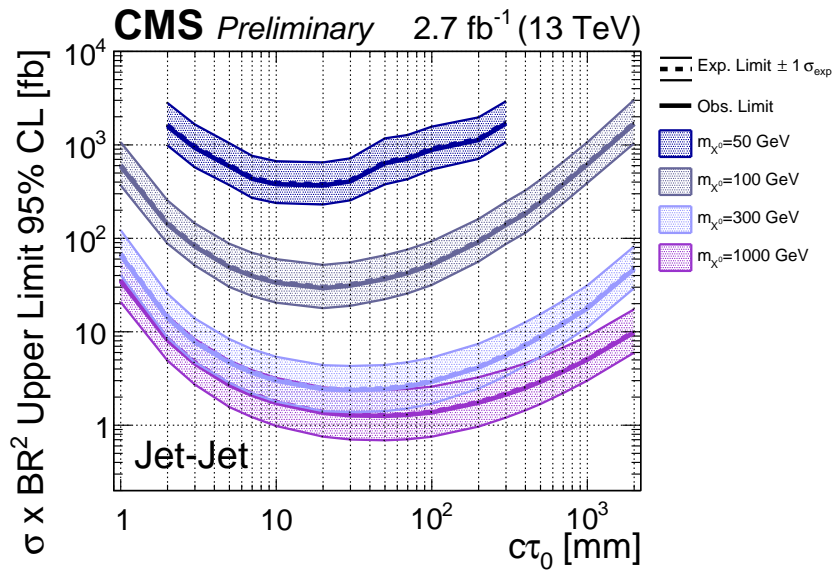
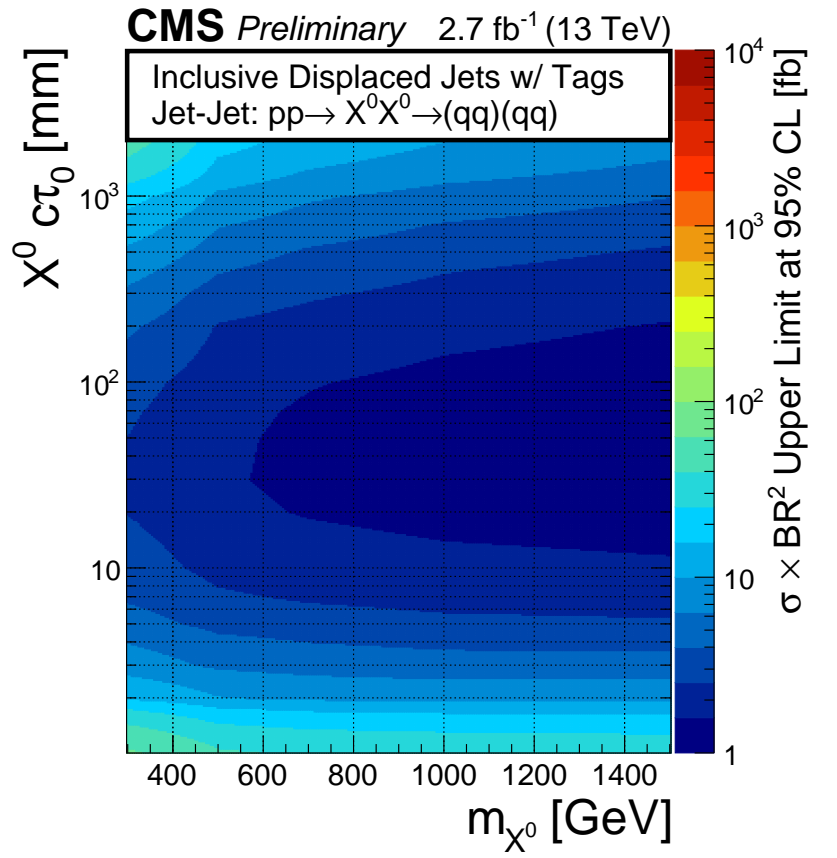


Figure 7.17: The excluded cross section at 95% CL for the Jet-Jet model as a function of the mass and lifetime of the parent particle X^0 (top) and as a function of the lifetime for four values of the mass (bottom).

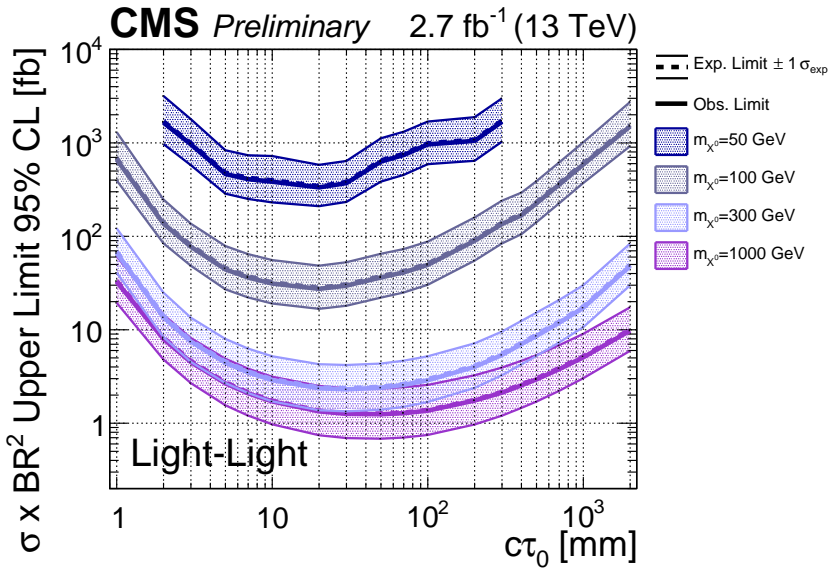
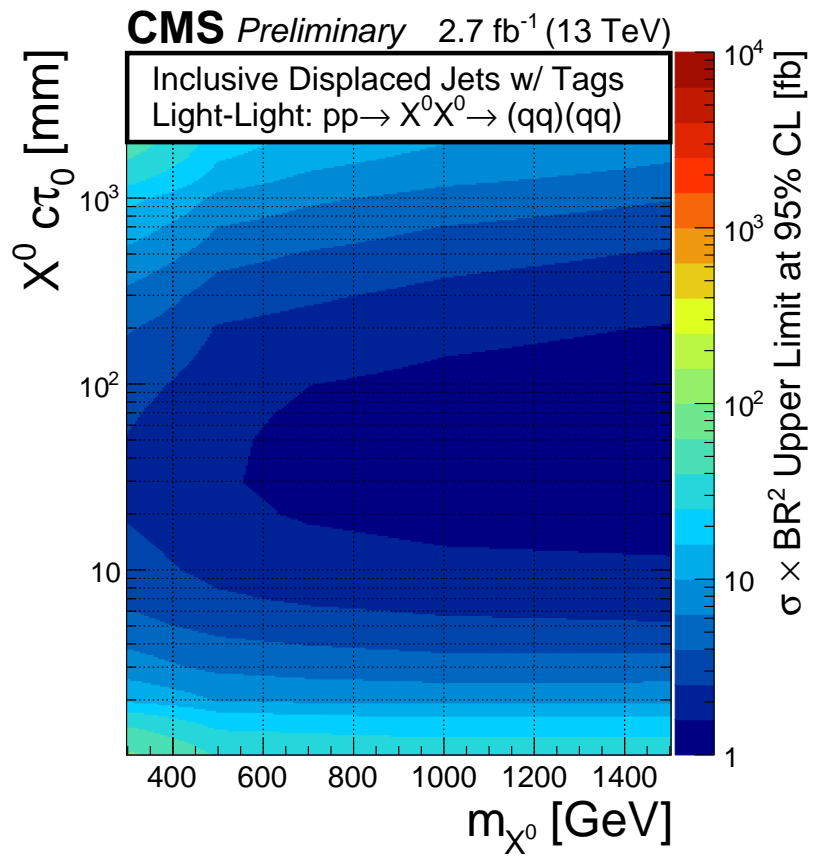


Figure 7.18: The excluded cross section at 95% CL for the Light-Light model as a function of the mass and lifetime of the parent particle X^0 (top) and as a function of the lifetime for four values of the mass (bottom).

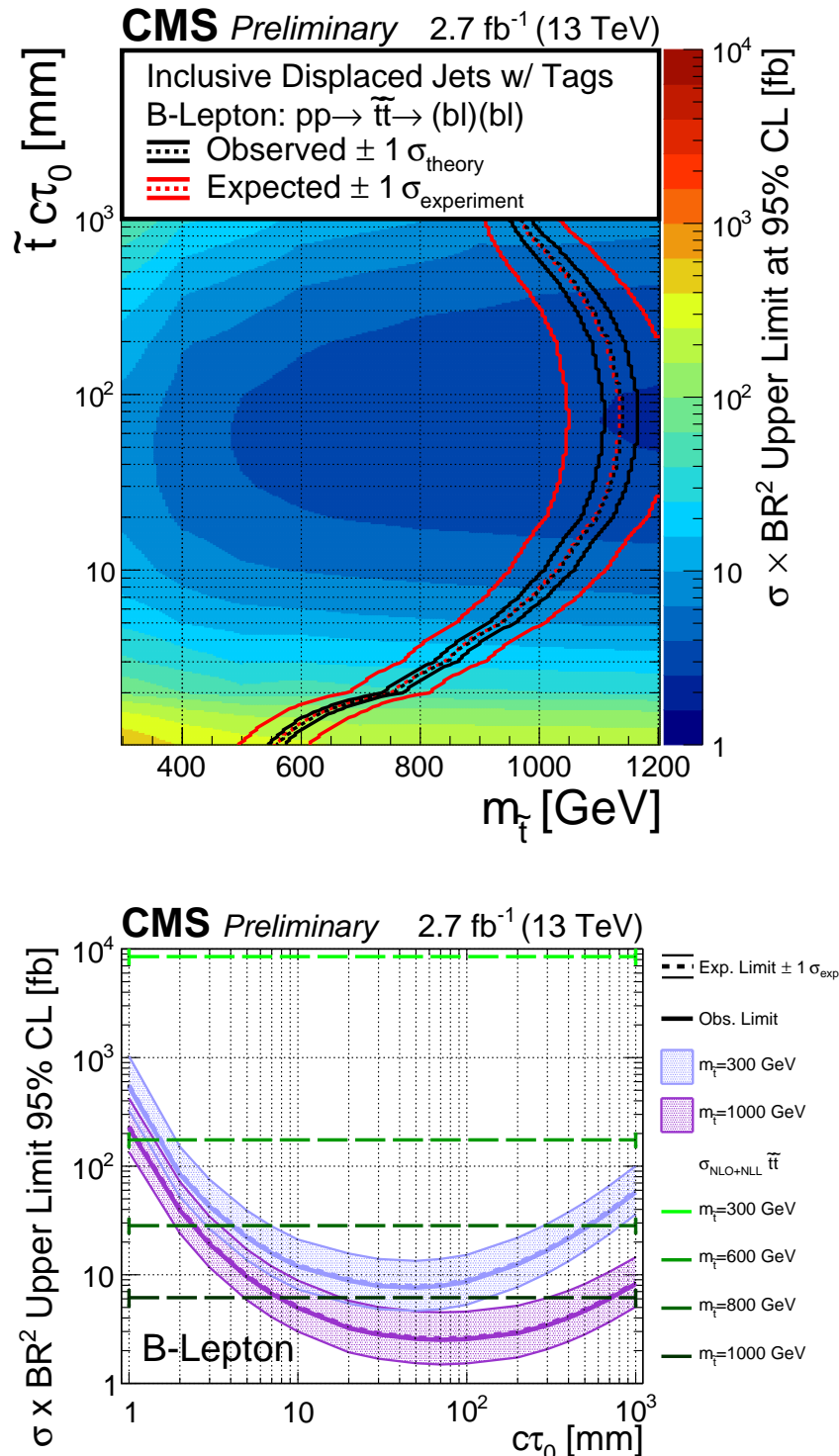


Figure 7.19: The excluded cross section at 95% CL for the B-Lepton model as a function of the mass and lifetime of the parent particle \tilde{t} (top) and as a function of the lifetime for two values of the mass (bottom). The bottom plot also shows the expected upper limits with one standard deviation uncertainties.

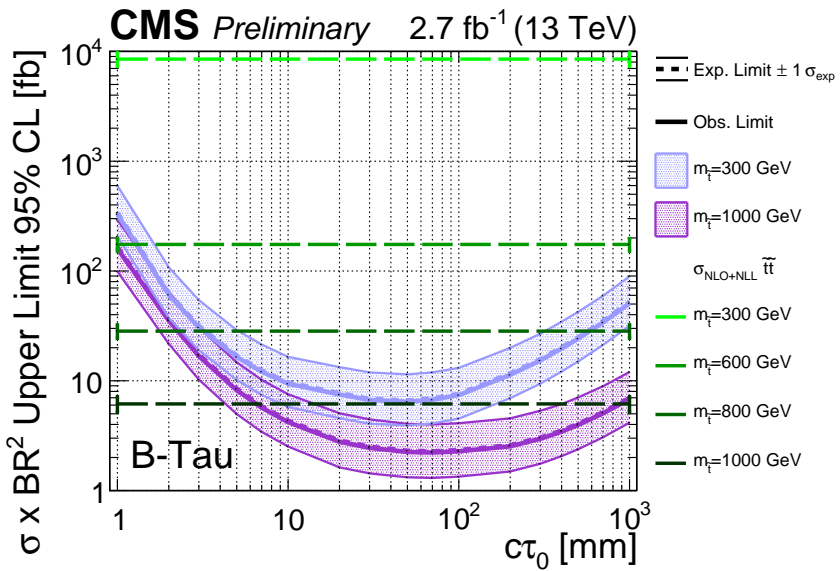
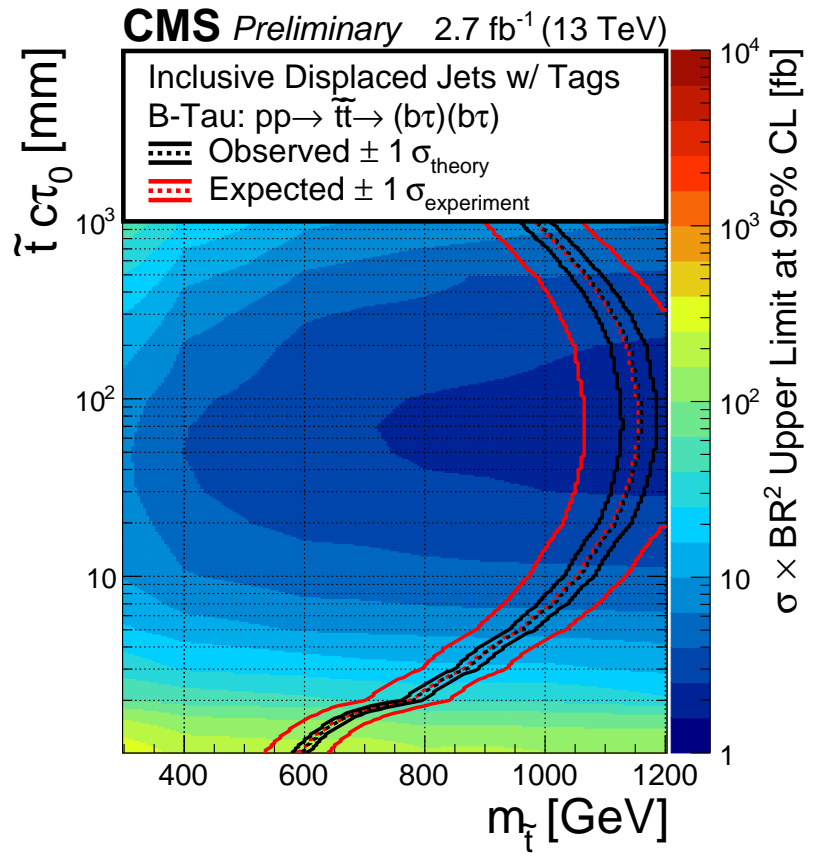


Figure 7.20: The excluded cross section at 95% CL for the B-Tau model as a function of the mass and lifetime of the parent particle \tilde{t} (top) and as a function of the lifetime for two values of the mass (bottom). The bottom plot also shows the expected upper limits with one standard deviation uncertainties.

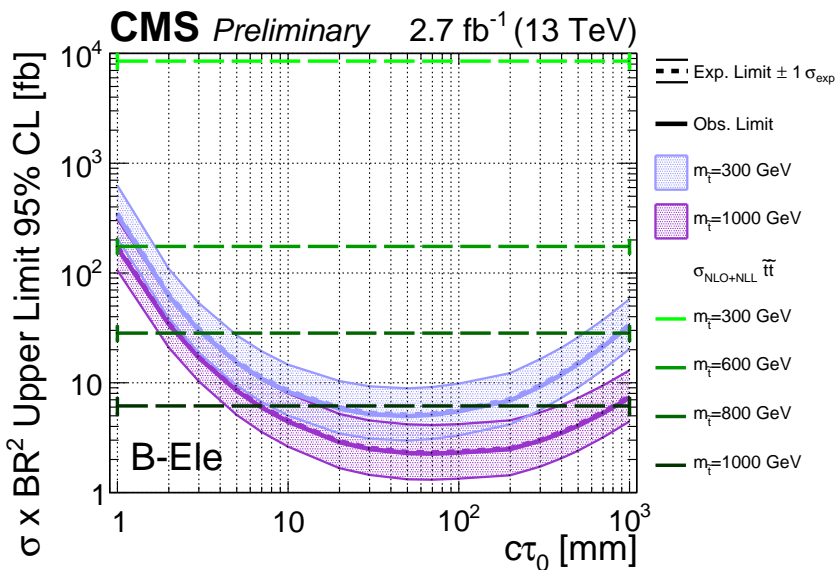
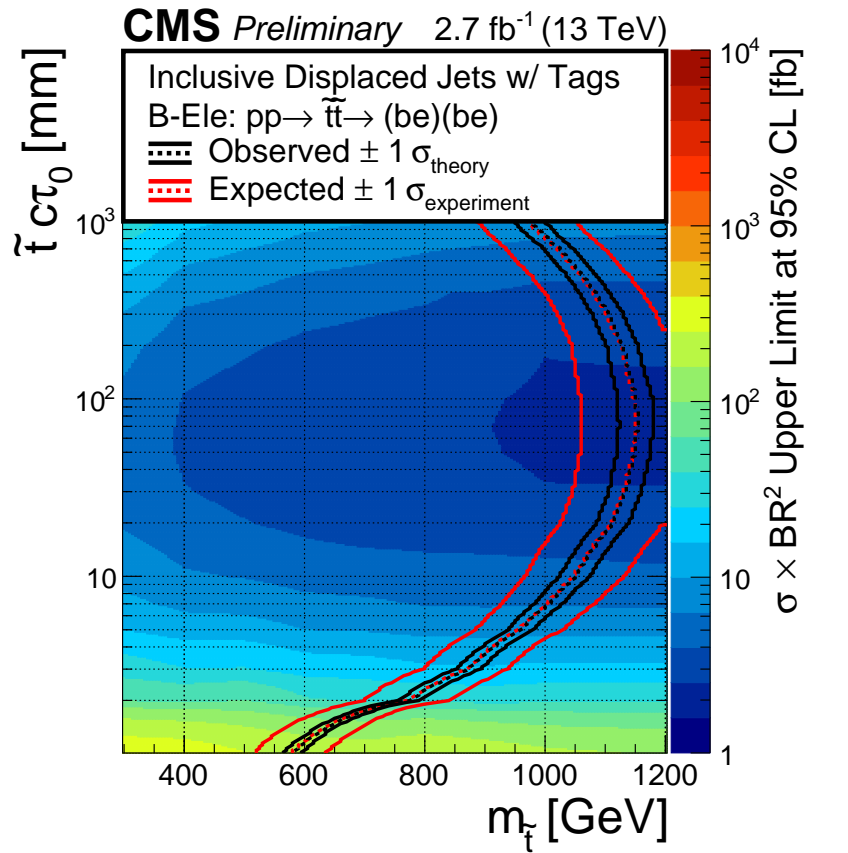


Figure 7.21: The excluded cross section at 95% CL for the B-Ele model as a function of the mass and lifetime of the parent particle \tilde{t} (top) and as a function of the lifetime for four values of the mass (bottom). The bottom plot also shows the expected upper limits with one standard deviation uncertainties.

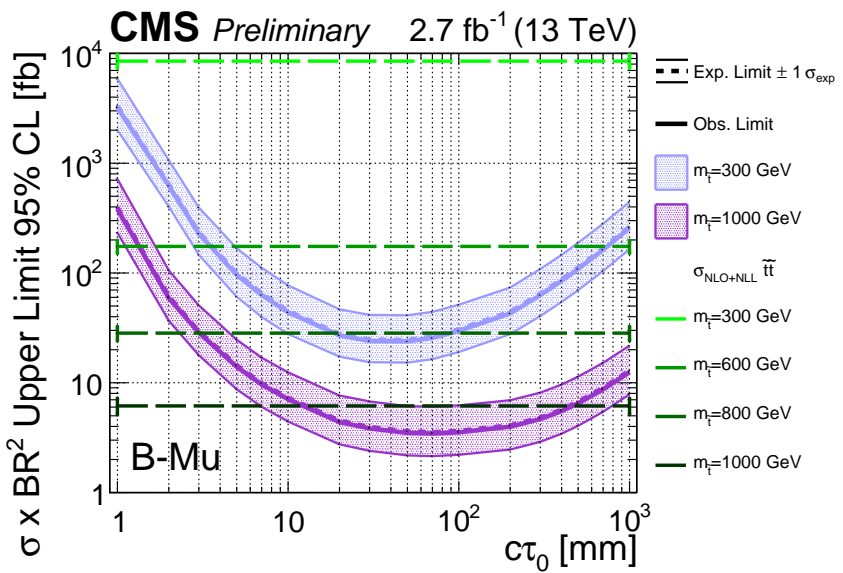
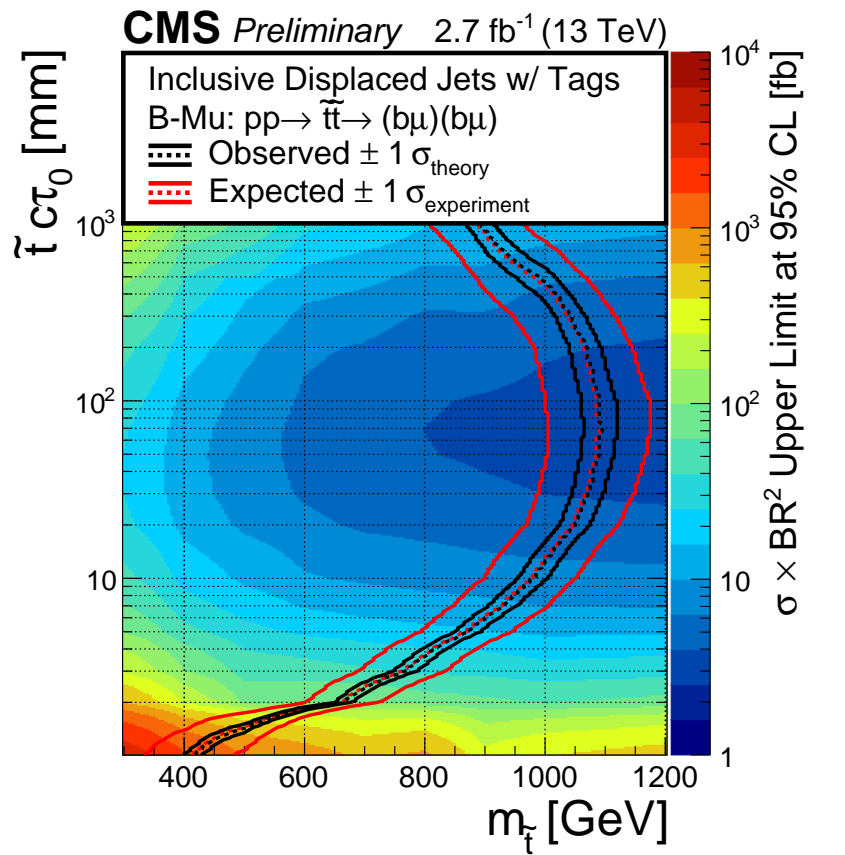


Figure 7.22: The excluded cross section at 95% CL for the B-Mu model as a function of the mass and lifetime of the parent particle \tilde{t} (top) and as a function of the lifetime for four values of the mass (bottom). The bottom plot also shows the expected upper limits with one standard deviation uncertainties.

Bibliography

- [1] Georges Aad et al. Search for long-lived, weakly interacting particles that decay to displaced hadronic jets in proton-proton collisions at $\sqrt{s} = 8$ TeV with the atlas detector. *Phys. Rev. D*, 92:012010, 2015.
- [2] Georges Aad et al. Search for massive, long-lived particles using multitrack displaced vertices or displaced lepton pairs in pp collisions at $\sqrt{s} = 8$ TeV with the ATLAS detector. *Phys. Rev. D*, 92:072004, 2015.
- [3] Vardan Khachatryan et al. Search for Long-Lived Neutral Particles Decaying to Quark-Antiquark Pairs in Proton-Proton Collisions at $\sqrt{s} = 8$ TeV. *Phys. Rev. D*, 91:012007, 2015.
- [4] Matteo Cacciari, Gavin P. Salam, and Gregory Soyez. Fastjet user manual. *Eur. Phys. J. C*, 72, 2012.
- [5] Matteo Cacciari, Gavin P. Salam, and Gregory Soyez. The anti- k_t jet clustering algorithm. *JHEP*, 04:063, 2008.
- [6] T. Sjöstrand, Stephen Mrenna, and Peter Z. Skands. A brief introduction to PYTHIA 8.1. *Comput. Phys. Commun.*, 178:852, 2008.
- [7] R. et al Ball. Parton distributions with LHC data. *Nucl. Phys. B*, 867:244, 2013.
- [8] M. Strassler and Zurek K. Discovering the higgs through highly displaced vertices. *Phys. Lett. B*, 263, 2008.
- [9] P. Graham, D. Kaplan, S. Rajendran, and P. Sarawat. Displaced supersymmetry. *Journal of High Energy Physics*, 149, 2012.
- [10] CMS Luminosity Measurement for the 2015 Data Taking Period. Technical Report CMS-PAS-LUM-15-001, CERN, Geneva, 2016.
- [11] A. L. Read. Presentation of search results: the CL_s technique. *J. Phys. G*, 28:2693, 2002.
- [12] Thomas Junk. Confidence level computation for combining searches with small statistics. *Nucl. Instrum. Meth. A*, 434:435, 1999.
- [13] CMS and ATLAS Collaborations. Procedure for the lhc higgs boson search combination in summer 2011. CMS-NOTE-2011-005, 2011.

- [14] W. Beenakker, R. Höpker, M. Spira, and P. M. Zerwas. Squark and gluino production at hadron colliders. *Nucl. Phys. B*, 492:51, 1997.
- [15] A. Kulesza and L. Motyka. Threshold resummation for squark-antisquark and gluino-pair production at the LHC. *Phys. Rev. Lett.*, 102:111802, 2009.
- [16] A. Kulesza and L. Motyka. Soft gluon resummation for the production of gluino-gluino and squark-antisquark pairs at the LHC. *Phys. Rev. D*, 80:095004, 2009.
- [17] W. Beenakker, S. Brensing, M. Krämer, A. Kulesza, E. Laenen, and I. Niessen. Soft-gluon resummation for squark and gluino hadroproduction. *JHEP*, 12:041, 2009.
- [18] W. Beenakker, S. Brensing, M. Krämer, A. Kulesza, E. Laenen, L. Motyka, and I. Niessen. Squark and gluino hadroproduction. *Int. J. Mod. Phys. A*, 26:2637, 2011.
- [19] M. Krämer, A. Kulesza, R. van der Leeuw, M. Mangano, S. Padhi, T. Plehn, and X. Portell. Supersymmetry production cross sections in pp collisions at $\sqrt{s} = 7$ TeV. 2012.